NTNU – Trondheim
Norwegian University of
Science and Technology

Effects of BOP Stack Modelling on Estimated Wellhead Fatigue Damage

Erling Harildstad
Andreas Haukanes

Subsea Technology
Submission date: June 2013
Supervisor: Bernt Johan Leira, IMT
Co-supervisor: Rune Yttervik, Statoil

Norwegian University of Science and Technology
Department of Marine Technology

NTNU
Norwegian University of Science and Technology
Department of Marine Technology

Master Thesis, Spring 2013
for
Erling Harildstad og Andreas Haukanes

Effects of BOP Stack Modelling on Estimated Wellhead Fatigue Damage

Innvirkning av BOP Modellering på Estimert Utmatnings-skade for Brønnhode

Statoil is working to improve the quality and accuracy of computer simulations which are applied for predicting global response in critical components in relation to offshore drilling operations. Such components comprise the marine riser, the flex-joint, the tensioner system, the BOP stack, the well-head, the conductor and the casing.

When using the term 'BOP stack' reference is made to a system consisting of the BOP connector, the BOP, the connector between the BOP and the LMRP, the LMRP and the lower flex joint.

Comparison of results from computer simulations and full-scale measurements indicate that the simulation models used today are overly conservative with respect to fatigue calculations.

A proper representation of the structural properties of the BOP stack has been identified as one of the shortcomings of today's models. The objective of the present thesis is to contribute to improving the model in this respect.

Common practice in relation to dynamic analyses of drilling systems is to model the BOP stack with infinitely high stiffness. By 'infinite' stiffness we mean a stiffness that will result in zero curvature in the BOP stack for any applied loading. To investigate this assumption and its influence on wellhead fatigue calculations, improved and realistic BOP stack structural properties should be implemented in the global analyses. The improved model may be obtained by investigating a corresponding detailed 3D element model of the BOP stack.

The influence of improving the BOP stack structural properties on estimated fatigue life can accordingly also be assessed.

The following subjects are to be addressed as part of this work:

1. An overview is to be given of methods and procedures which are applied for estimation of wellhead fatigue as described in the relevant literature. Relevant design guidelines are also to be briefly summarized.

2. Numerical models are to be established for an example BOP stack. Both a full 3D Finite Element Model and a simplified beam element model (with structural properties obtained from the 3D model) are to be considered.

3. Non-linear time-domain dynamic response analyses which are based on a global riser model in Riflex/Sima are to be performed for a particular drilling system. Comparison is to be made between results from response calculations which are based both on BOP stack models which are infinitely rigid and with elastic properties taken into account.

4. Fatigue damage assessment is to be performed for a relevant hotspot in the wellhead. Comparison between fatigue damage which is computed by application of different BOP stack models is to be elaborated upon.

5. Parametric variations with respect to structural properties of the BOP stack are performed to the extent that time allows. The resulting effect of these properties on the computed well-head damage is to be highlighted.

The work scope may prove to be larger than initially anticipated. Subject to approval from the supervisor, topics may be deleted from the list above or reduced in extent.

In the thesis the candidate shall present his personal contribution to the resolution of problems within the scope of the thesis work.

Theories and conclusions should be based on mathematical derivations and/or logic reasoning identifying the various steps in the deduction.

The candidate should utilise the existing possibilities for obtaining relevant literature.

The thesis should be organised in a rational manner to give a clear exposition of results, assessments, and conclusions. The text should be brief and to the point, with a clear language. Telegraphic language should be avoided.

The thesis shall contain the following elements: A text defining the scope, preface, list of contents, summary, main body of thesis, conclusions with recommendations for further work, list of symbols and acronyms, references and (optional) appendices. All figures, tables and equations shall be numbered.

The supervisor may require that the candidate, in an early stage of the work, presents a written plan for the completion of the work. The plan should include a budget for the use of computer and laboratory resources which will be charged to the department. Overruns shall be reported to the supervisor.

The original contribution of the candidate and material taken from other sources shall be clearly defined. Work from other sources shall be properly referenced using an acknowledged referencing system.

The thesis shall be submitted in electronic form:

- Signed by the candidate

- The text defining the scope included
- Drawings and/or computer prints which cannot be bound should be organised in a separate folder.

Supervisor: Professor Bernt J. Leira

Contact person at Statoil: Rune Yttervik

Deadline: June 10th 2013

Trondheim, January 14th, 2013

Bernt J. Leira

Bernt J. Leira

Preface

This master's thesis has been carried out at the Department of Marine Technology, Faculty of Engineering Science and Technology at the Norwegian University of Science and Technology (NTNU). The thesis has been written as part of the Master of Science program in Marine Subsea Engineering. The thesis is weighted by 30 credits and has been written during the last semester.

We would like to thank our supervisor at the Department of Marine Technology, Bernt J. Leira, for essential guidance and good advice. We would also like to thank Rune Yttervik from Statoil for providing the necessary input data and for demonstrating great commitment to our work.

June 7, 2013

Erling Harildstad Andreas Haukanes

Trondheim, *June 2013*

Abstract

To date, there are no international codes or standards that deal with estimation of fatigue in subsea wellhead systems. Nevertheless have preliminary analytical methods for wellhead fatigue estimation been established. These analytical methods involve the use of global dynamic response analyses. Such analyses are commonly carried out in finite element software where the drilling system is modelled as beam or bar elements. Several uncertainties exist in regards to the mathematical modelling and simulation in global response analyses of drilling systems. In this thesis the uncertainties that are related to the goodness of the representation of the blowout preventer stack (BOP stack), are addressed.

An overview of previous and ongoing work on analytical estimation of wellhead fatigue is given. Relevant theory on the subject is presented and described. The theory comprises of fatigue on structures, loads on a drilling system and static and dynamic response analysis. The main features of the preliminary analytical methods for estimating wellhead fatigue are summarized.

The BOP stack is commonly assumed to have infinitely high stiffness when performing a global response analysis of a drilling system. The main objective in the thesis is to investigate if this is a good assumption. The investigation start with local modelling of an elastic beam element model of a BOP stack. Further, this elastic beam model is calibrated to have the same stiffness properties as a detailed 3D element model of the BOP stack. The calibrated elastic beam BOP stack model is implemented in a global model of a drilling system. Global response analyses are carried out for two global models. One with an infinitely stiff BOP stack model and one with the calibrated elastic BOP stack model. Fatigue damage estimates are calculated with basis in the results from the global response analyses. The effects of BOP stack modelling are evaluated with regards to estimated fatigue damage in the wellhead. In addition to

this main study, parameter studies and a sensitivity study are carried out to evaluate uncertainties and assumptions within a realistic frame.

The results from the wellhead fatigue assessments conclude that the elastic BOP stack model imposes greater estimated fatigue damage in the wellhead compared to the infinitely stiff BOP stack model. The difference, in terms of estimated fatigue damage, imposed by the two BOP stack models is, at maximum, 0.51 % for the main study. The largest difference observed in the parameter studies is 1.34 %. Hence, it is concluded that the effects of improved BOP stack modelling in a global response analysis, with respect to wellhead fatigue estimation, is not significant. There are though some uncertainties connected to the bending stiffness of the wellhead connector and the LMRP connector.

Abstrakt

Det finnes per dags dato ingen internasjonale koder eller standarder som legger føringer for estimering av utmatting i brønnhodesystemer. Likevel har foreløpige analytiske metoder for estimering av utamtting i brønnhodesystemer blitt etablert. Disse analytiske fremgangsmåtene innebærer bruk av globale dynamiske responsanalyser. Slike analyser blir vanligvis utført i programvare som er basert på elementmetoden og hvor boresystemet blir modellert med bjelke- eller stavelementer. Det eksisterer flere usikkerheter i forhold til den matematiske modelleringen og simuleringen av boresystemer i globale responsanalyser. I denne oppgaven er usikkerheter relatert til hvor god representasjonen av utblåsningsventilen er, behandlet.

Det blir gitt en oversikt over tidligere og pågående arbeider som omhandler analytisk estimering av utmatting i brønnhoder. Relevant teori blir presentert og beskrevet. Teoridelen er delt inn i utmatting i strukturer, laster på boresystem og statisk og dynamisk responsanalyse. Hovedtrekkene i de metodene som brukes i dag for estimering av utmatting i brønnhodesystemer blir oppsummert.

Utblåsningsventilen er ofte antatt å ha uendelig høy stivhet når det utføres globale responsanalyser på boresystemer. Hovedmålet i avhandlingen er å undersøke om dette er en god antagelse. Dettte gjøres ved å først modellere en elastisk bjelkeelementmodell i et dedikert elementmetodeprogram. Denne modellen er en forenkling av utblåsningsventilen. Videre er denne elastiske bjelkemodellen kalibrert til å ha de samme stivhetsegenskapene som en 3D modell av utblåsningsventilen. Den kalibrerte, elastiske bjelkemodellen er deretter implementert i en global modell av et boresystem. Globale responsanalyser er utført for to globale modeller. En med en uendelig stiv modell av utblåsningsventilen og en med den kalibrerte, elastiske modellen av utblåsningsventilen. Estimatene av utmattingsskade er beregnet med basis i resultatene fra de globale responsanalysene. Effektene som modelleringen av utblåsningsventilen medfører blir evaluert opp mot den

uendelig stive modellen, med hensyn til estimert utmattingsskade i brønnhodet. I tillegg til dette hovedstudiet, er parameterstudier og en sensitivitetsstudie gjennomført for å vurdere en rekke usikkerheter og antagelser innenfor en realistisk ramme.

Ut i fra resultatene kan det konkluderes med at den elastiske modellen av utblsåningventilen induserer større estimert utmattingsskade i brønnhodet i forhold til den uendelig stive modellen. Den største forskjellen, i form av estimert utmattingsskade indusert av de to modellene, er i hovedstudiet 0.51 %. Den største forskjellen som er observert i parameterstudiene er 1.34 %. På grunnlag av dette konkluderes det med at effektene av forbedret modellering av utblåsningsventilen i en global responsanalyse, med tanke på estimering av utmatting i brønnhodet, er ikke signifikant. Derimot er det knyttet visse usikkerheter rundt bøyestivheten i koblingen mellom brønnhode og utblåsningsventilen, samt koblingen mellom øvre og nedre del av selve utblåsningsventilen.

Acronyms

ASME	American Society of Mechanical Engineers
BOP	Blowout Preventer
DNV	Det Norske Veritas
RP	Recommended Practice
FEA	Finite Element Analysis
FEM	Finite Element Method
LEFM	Linear Elastic Fracture Mechanics
JONSWAP	JOint North Sea WAve Project
LMRP	Lower Marine Riser Package
MODU	Mobile Offshore Drilling Unit
SN Curve	Stress versus number of cycles to failure
OMAE	International Conference on Ocean, Offshore and Arctic Engineering
OTC	Offshore Technology Conference
JIP	Joint Industry Project
PM	Pierson-Moscowitz
SCF	Stress Concentration Factor
VIM	Vortex Induced Motions
VIV	Vortex Induced Vibrations
WH	Wellhead
XT	Christmas Tree
EOF	Empirical Orthogonal Function
FORM	First Order Reliability Method
P-Y	Pressure-Displacement
ISO	International Organization of Standardization
API	American Petroleum Institute
DOF	Degree Of Freedom
CAE	Computer Aided Engineering
RAO	Response Amplitude Operator
CPU	Central Processing Unit
WAFO	Wave Analysis for Fatigue and Oceanography
DFF	Design Fatigue Factor

Symbols

N	Number of cycles to failure
ΔS	Stress range
$\Delta\sigma$	Stress range
ΔK	Stress intensity factor
m	Inverse slope of SN curve
n	Applied number of cycles
D	Fatigue damage
Q	Probability of exceedance of the stress range $\Delta\sigma$
q	Weibull scale parameter
h	Weibull stress range shape distribution parameter
$\Gamma\left(1+\frac{m}{h}\right)$	Gamma function
λ	Wave length
ϕ	Velocity potential
ζ	Wave elevation
ζ_a	Wave amplitude
k	Wave number
ω	Wave frequency
d	Water depth
P_D	Dynamic pressure
ϵ	Phase angle
$S(\omega)$	Wave spectrum
H_s	Significant wave height
T_p	Spectral peak period
u_c	Current velocity
H	Transfer function
C_M	Mass coefficient

C_D	Drag coefficient
P	Fluid pressure
$\overline{f_s}$	Average vortex shedding frequency
St	Strouhal number
$\overline{C}_L$	Average amplitude of transversal force coefficient
$\boldsymbol{M}$	Mass matrix
$\boldsymbol{K}$	Stiffness matrix
$\boldsymbol{C}$	Damping matrix
$\boldsymbol{R}$	Load vector (statics)
$\boldsymbol{Q}$	Load vector (dynamics)
$\boldsymbol{a}$	Connectivity matrix
$\boldsymbol{u}$	Displacement vector (dynamics)
$\dot{\boldsymbol{u}}$	Velocity vector (dynamics)
$\ddot{\boldsymbol{u}}$	Acceleration vector (dynamics)
$\boldsymbol{r}$	Displacement vector (statics)
E	Youngs modulus
I	Second moment of area
$\log \bar{a}$	Intercept with $\log N$ axis of SN-curve

Contents

List of Figures

List of Tables

Chapter 1

Introduction

1.1 General Background

In a historical perspective, the easiest accessible hydrocarbon reservoirs have been developed first. Now, offshore oil and gas exploration move into deeper and more harsh environments. Technological advancements have enabled development of previously inaccessible reservoirs. The improved ability to find and develop fields offshore and the ability to drill deviated wells are such important advancements [1]. Simultaneously, new technology makes it possible to extract even more hydrocarbons and gas from existing wells. At the last count, there were over 800 subsea wells in the North Sea. Many of these wells are over 20 years old, and economic demands dictate that they are used for longer periods. Subsea wells that are used for longer periods will experience larger accumulated loads. Consequently, regulatory bodies are seeking assurances that the wells' condition and integrity are being correctly managed, particularly with regard to fatigue design and calculation methodologies [2]. Subsea wells are usually drilled using a mobile offshore drilling unit, MODU. The MODU is commonly connected to a subsea wellhead system by a drilling riser. The dynamic response of the MODU and the drilling riser due to environmental loading imposes dynamic loads to the subsea wellhead system. The dynamic loads may lead to the growth of cracks in welds in the wellhead and lead to structural failure. Such a structural failure in the wellhead system can lead to severe consequences. A failure may expose the well to the environment and make any intervention impossible. Consequences like this implies the need for methods that can predict the fatigue load capacity of subsea wellhead systems.

To date, there are no international codes or standards which provide guidance on how subsea wellhead fatigue assessments shall be carried out [3]. Nevertheless have preliminary analytical methods for wellhead fatigue estimation been established. These analytical methods involves the use of global dynamic response analyses. Such analyses

are commonly carried out in finite element software where the drilling system is modelled as beam elements. Challenges are related to the goodness of the representation of subsea components in such analyses. One of these subsea components is the blowout preventer stack.

1.2 Previous and Ongoing Work

Reviewing previously published work on dynamical lateral loading of subsea wellhead systems, one interesting finding is that the majority of work identified has been published during the period from 1983 to 1993 [4]. There is an indication that this is a response to a wellhead fatigue failure reported to have happened west of Shetland in 1981. In OMAE Conference 1989, Singeetham [5] reported that there had been several subsea wellhead failures in service, and the failures were primarily at the bottom of the high pressure housing. Furthermore, Statoil experienced abnormal BOP movements on a North Sea subsea wellhead due to a fatigue failure in a conductor weld in 2005 [6].

1.2.1 Joint Industry Project - Structural Well Integrity

In mid-2010, a number of the world's leading oil companies came together to begin a joint industry project(JIP) to develop structural well integrity guidelines, and along with this a method for wellhead fatigue analysis [3].

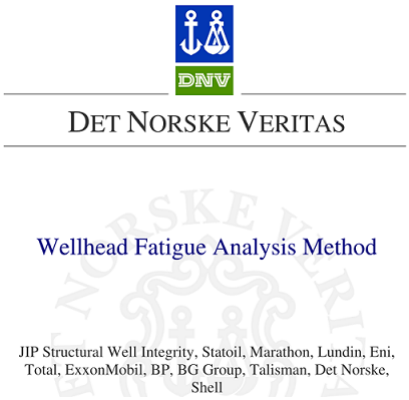

Figure 1.1: JIP - Participants [3]

The motivation for developing an industry guideline stems from the fact that existing international standards provide limited or no guidance on wellhead fatigue calculation.

Despite of this, suggestions for wellhead fatigue assessment exist. Comparison between the results from these fatigue assessments and the inspections of exhausted wellheads indicate that the current methods are overly conservative. One of the objectives of the JIP is to assess the gap in the existing standards, and provide a uniform method on how to perform wellhead fatigue assessments.

The list of companies that make up the JIP; Statoil, DNV, Marathon, Lundin, Eni, Total, ExxonMobil, BP, BG Group, Talisman, Det Norske and Shell really emphasizes the need for a unified methodology of wellhead fatigue analysis in the industry. According to Buchmiller *et al.* [7], a uniform approach for performing wellhead fatigue calculations will improve traceability, and control can be established for the structural capacity of the subsea wellhead systems.

1.2.2 Current Work

There are many studies in progress on wellhead fatigue assessment, and not only does the number of studies emphasize the complexity of the subject, the variation in method approaches and considerations made, do as well. Many of the studies that are done are presented on the annual OMAE[1] conference which is organized by ASME[2]. OTC[3] is another conference of this kind. The majority of the following contributions deal with the guidelines that are established in the JIP. This is done to investigate techniques and methods addressed by the JIP and modify them if necessary.

The effect of a fatigue failure on the wellhead ultimate load capacity

Reinås *et al.* [8] discuss reduction in ultimate load capacity due to a fatigue fracture, and where these fractures are likely to occur. If the factored fatigue life of a subsea wellhead is approaching its limit, the presence of a fatigue fracture should be assumed. A reduction in the ultimate load capacity due to a fatigue fracture may reduce the safety margin should an accidental or extreme loading occur. An example of an accidental load is an uncontrolled MODU offset due to anchor failure or loss of anchors. The paper concludes that there is a significant reduction in a wells' structural capacity where a welded connection has experienced a fatigue failure. In fact, a fatigue failure

[1] http://www.asmeconferences.org/OMAE2013/
[2] http://www.ooae.org/
[3] http://www.otcnet.org/2013/

in the conductor housing weld, left the well with 41 % structural capacity compared to the intact well. In the event where a well is to be re-used, a weak-point analysis is recommended to be conducted. If the weak point analysis reveals reduced structural capacity, new guidelines on MODU offset limitations may have to be established.

The effect of variation of lower boundary conditions in global riser load analysis

Reinås *et al.* [9] explores the effect on the global load analysis by changing the lower boundary condition. The loads that are obtained through global analyses are applied to a local wellhead model. Differences, if any, in terms of fatigue life between the boundary conditions, are spotted. The different models use the same upper boundary condition. The following lower boundary conditions are proposed:

- ◇ fixed at wellhead
- ◇ ISO 13624-2
- ◇ JIP - current method
- ◇ JIP - modified method

Reinås *et al.* [9] also discuss approaching the wellhead fatigue analysis in two ways. A de-coupled approach and a coupled approach. The paper concludes that there are minor differences in the loading obtained from the global analyses with respect to the the different boundary conditions. In early design phase, fixed boundary condition may be used as a starting point, however, setting the boundary condition according to the JIP indicates capturing a more dynamic behaviour than that of the other two boundary conditions investigated. It is also noted that differences in the local modelling methodology can have great effect on the calculated fatigue life, meaning modelling must be done with great caution.

The effects of modelling techniques and data uncertainty in wellhead fatigue life calculation

Williams and Greene [10] have outlined a holistic[4] method of wellhead system fatigue life calculation. They have also outlined a series of parametric studies to determine the

[4]Holism - a set of beliefs in which everything in nature is seen as being connected in some way

sensitivity of the fatigue calculations to variations and uncertainties in the input data. Especially three cases are investigated:

- ◇ VIV fatigue calculation. Sensitivity of input current profile
- ◇ The effect of modelling simple riser tensioner system versus detailed.
- ◇ The effect of linear flex joint stiffness versus non-linear stiffness on wellhead fatigue estimates.

VIV response of the riser will impart VIM to the wellhead, which will add to the existing fatigue damage. Uncertainty in VIV response of a drilling riser system is addressed and it is stressed that different software can produce VIV estimates. The calibration of coefficients can also be different. For VIV calculation, Williams and Greene compare use of detailed measurements of current taken from site versus the application of current profiles generated with basis in statistical analysis of field measured data. In this paper, the software tool SHEAR7[5] is used to calculate the VIV response. A detailed tensioner model is found to be reducing fatigue life in the wellhead between 20 % to 40 %, and hence a detailed tensioner system is recommended to be implemented in a wellhead fatigue analysis. The use of non-linear flex joint characteristics versus linear characteristic led to a reduction in the conductor fatigue life by approximately 30 %, whilst having little impact on the riser VIV response.

A new boundary condition modelling of lateral cement support in local wellhead models

Sæther *et al.* [4] address the importance of the well cement as a lateral supporting boundary condition of the wellhead and surface casing in a local model of a subsea wellhead system. In their paper they apply a modified boundary condition approach that differs from the previously applied ways of modelling cement in a wellhead fatigue context. The modelling and analyses are carried out in both 2D FEM wellhead model and a complex 3D FEM wellhead model. The paper explains the common procedure for the instalment of the wellhead, i.e. installation of conductor housing, conductor, surface casing and cement. The modified approach is derived on the basis of this procedure. The modified approach led to a reduction in estimated stress in the surface casing weld. These estimates are though only valid if the BOP is landed on the subsea wellhead before

[5] http://shear7.com/

the cement close to the seabed has properly set. The stress reduction was verified in the 3D model as well as the 2D model.

Benefits of a structural reliability analysis approach

Hørte *et al.* [11] investigates if it is reasonable that the probability of wellhead fatigue failure can be estimated. If that is the case, such results can enable quantified risk assessments of the wellhead fatigue failure problem. They argues that a deterministic approach introduces unnecessary conservatism, as many "worst case" values are used for many of the input parameters. The structural reliability approach is in this context considered immature and is not yet applied to a real case. It is, however, noted that the approach reveals interesting findings with respect to uncertainties in cement level, global load calculations, SN curve and more.

Fatigue assessment of subsea wells for future and historical operations based on measured riser loads

Russo *et al.* [12] immerse themselves in the possibilities of calculating future fatigue damage based on measured riser loads. Forecasting future fatigue damage is based on global riser analyses results, which has shown to introduce conservatism. By applying measured riser response, historical fatigue damage can be estimated. Russo suggests a refined methodology using actual measured response to assess historical fatigue damage and future fatigue damage by combining an analytical local well modelling with full scale measurements statistics. One of the findings is that this refined approach indicates that a pure analytical fatigue approach is highly conservative. The refined approach was proven to be slightly conservative compared to actual measurements of exhausted wellheads.

Parameters affecting fatigue damage accumulation

Lim *et al.* [13] highlight a number of parameters affecting the fatigue damage accumulation of subsea wellheads, such as

- Soil strength
- BOP stack size

- ◇ Conductor and casing design
- ◇ Wellhead design

Soft and stiff soils give rise to increased fatigue accumulation in conductor and surface casing and welds and connectors near the mudline, respectively. This is a result of bending loads caused by deflection of the BOP stack. In soft soils, the peak bending moment typically occurs at 5 meters to 10 meters below the mudline, thus making the conductor and surface casing at these depths the most critical components in terms of fatigue damage. In stiff soils, the peak bending moment typically occurs at 5 meters or less below the mudline, resulting in greatest fatigue accumulation at the welds near the mudline.

Increased BOP stack size results in larger bending moments at the wellhead if any motion is present. A more massive BOP stack increases the natural period of the BOP and makes it more susceptible to riser motion. This will induce larger displacements in the BOP stack and consequently greater fatigue damage accumulation in the wellhead.

1.3 Thesis Objectives

- ◇ An overview is to be given of methods and procedures which are applied for estimation of wellhead fatigue as described in the relevant literature. Relevant design guidelines are also to be briefly summarized.
- ◇ Numerical models are to be established for an example BOP stack. Both a full 3D Finite Element Model and a simplified beam element model (with structural properties obtained from the 3D model) are to be considered.
- ◇ Non-linear time-domain dynamic response analyses which are based on a global riser model in Riflex/Sima are to be performed for a particular drilling system. Comparison is to be made between results from response calculations which are based both on BOP stack models which are infinitely rigid and with elastic properties taken into account.
- ◇ Fatigue damage assessment is to be performed for a relevant hotspot in the wellhead. Comparison between fatigue damage which is computed by application of different BOP stack models is to be elaborated upon.
- ◇ Parametric variations with respect to structural properties of the BOP stack are

performed to the extent that time allows. The resulting effect of these properties on the computed well-head damage is to be highlighted.

1.3.1 Thesis Structure

Chapter 1 gives an introduction to the topic of wellhead fatigue assessment and outlines previous and ongoing work on the subject.

Chapter 2 presents the subsea drilling process and describes the components which are commonly used in this context.

Chapter 3 deals with the fatigue theory which is relevant to the exhaustion of welds in subsea wellhead systems.

Chapter 4 addresses the environmental loads that acts on a drilling system.

Chapter 5 presents software for response analysis of structures and the theory they are based upon.

Chapter 6 presents the main features of current wellhead fatigue methodologies.

Chapter 7 describes the modelling process and the setup of the analyses that were conducted in the investigation of the effects of BOP stack modelling on wellhead fatigue damage.

Chapter 8 presents and discusses the results from the wellhead fatigue assessments which are described in chapter 7. highlights **Chapter 9** summarizes the most important results and presents conclusions that are made.

Chapter 10 presents suggestions for for further work.

Appendix A contains information about the two models of the BOP stack that are used in the local analyses in this thesis.

Appendix B contains information about the calibration of an elastic beam model of the BOP stack

Appendix C contains information about the global drilling system model

Appendix D contains results from the fatigue damage assessments that were carried out in this thesis.

Appendix E gives information about the contents in the attached data folder.

Chapter 2

Offshore Drilling

2.1 Subsea Drilling, Workover and Intervention

2.1.1 Subsea Drilling

In this section a brief introduction to the typical steps in subsea drilling is given to give an understanding of which system components are needed for the different phases of the drilling operation.

Subsea drilling is divided into several steps. In each step, a steel casing is set down and cemented in place. The size of the well bore, and therefore also the size of the hole, decreases with each step. figure 2.1 represents a typical casing configuration.

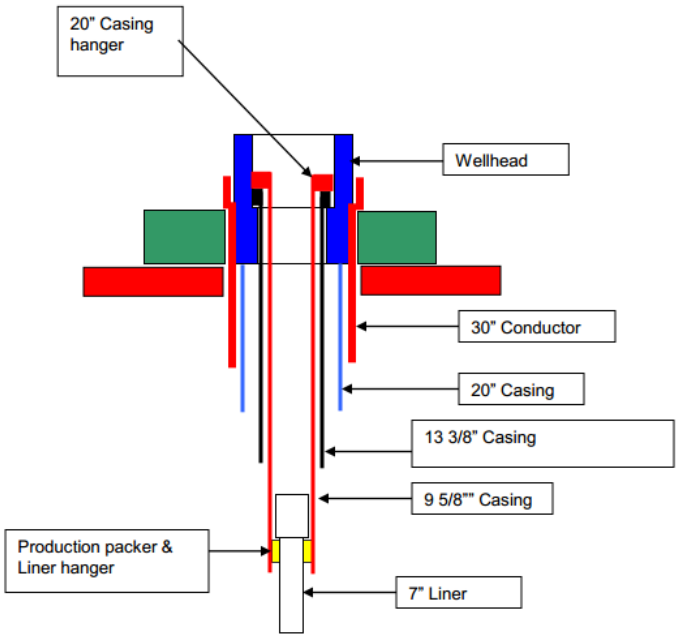

Figure 2.1: Typical casing configuration [14]

Initially a guide base is installed on the seabed. A 36″ hole is then drilled and fitted with a 30″ conductor. Drilling of the 36″ and the 26″ top hole sections does not require complete circulation of the drill mud, a drilling riser is thus not needed. In this phase the mud is typically disposed at the sea floor. A 20″ casing which corresponds to a 26″ hole is normally equipped with an $18\,3/4$″ wellhead. Then the blowout preventer (BOP) and the riser is run and fitted to the wellhead. The drilling continues through the riser and the BOP. Now the mud is circulated up to the floater. Further the $17\,1/2$″ and the $12\,1/4$″ holes are drilled and the corresponding $13\,3/8$″ and $9\,5/8$″ casings are run. The final step is to drill the reservoir section and complete the well.

A specially composed mud is used to transport cuttings from the well bore up to the surface when drilling. The mud enters the well through the drill string and is pumped down the well. When it enters the well bore it transports the well cuttings up to the surface through the annulus of the riser. The properties of the mud have to be altered for each step to adjust for the change in the pressure from the formation. As drilling progresses, the pressure from the formation increases. A heavier mud is therefore required to withstand this pressure. The mud must though not be too heavy, or the formation may fracture. A second property of the mud is to act as a pressure barrier. The mud will act as a counter force and help to prevent a potential blow out if one should unexpectedly drill into a high pressure gas pocket.

2.1.2 Workover and Intervention

For existing subsea wells, it is essential to perform periodic service and maintenance to ensure the integrity of the production system through the life of the well. This kind of maintenance requires a stop in oil production and that an external vessel to connects to the well. One kind of operation, known as workover, comprises removal of well components like production tubing and wellhead. This is a large and expensive operation and may impose substantial loads on the well system.

The term intervention refers to periodic maintenance done to the well to optimize and monitor the production. This kind of operation may be executed with different techniques, depending on the work that is scheduled to be done. The techniques may be divided into three categories;

A: Light Intervention

- Wireline without riser

B: Medium Intervention

- Wireline with riser, coiled tubing

C: Heavy intervention

- Wireline with riser, coiled tubing, drillstring

Different subsea components are required for intervention and workover operations. To conduct a wellhead fatigue assessment for such operations, these components must be incorporated in the analyses.

2.2 Components in Offshore Drilling Operations

The integrity of the components used in offshore drilling is essential to make safe and efficient operations possible. Though the main concern in this paper is the wellhead system, all components in the system play their part in influencing the distribution of the environmental loading. These components will be described in this chapter.

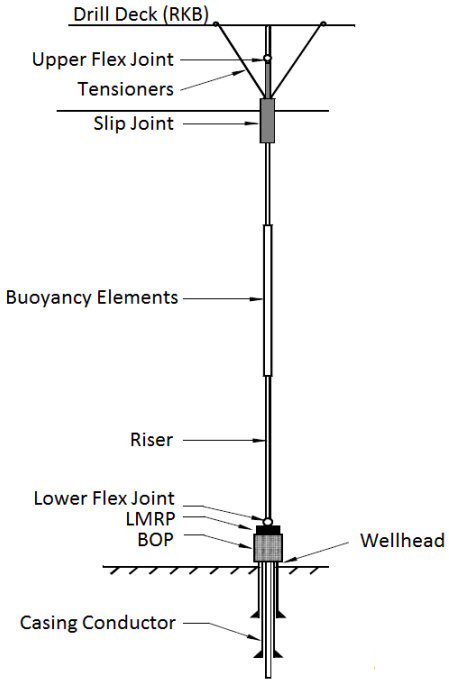

Figure 2.2: Drilling system [9]

2.2.1 Marine Riser

A marine riser acts as a conduit that connects the MODU to the subsea well. There are mainly two types of drilling risers used in the industry today.

- ◇ Low pressure risers
  - – Open to atmospheric pressure
  - – Kill and choke lines
  - – Subsea BOP

- ◇ High pressure risers
  - – Closed to atmospheric pressure
  - – Simple design, no choke and kill lines
  - – Topside BOP

The riser consists of several joints which are connected when the pipe is run. Typical lengths of the joints are between 9 and 25 meter. To reduce the riser's weight in water, buoyancy elements are fitted to the joints. The joints close to the surface are though left without such elements. The wave loads acting on the riser depend on the diameter of the pipe. Hence, pipes with low diameter in the surface region will minimize the riser's response. Outside the main riser pipe, choke, kill and booster lines are attached. Kill and choke lines are used to control potential high pressure occurrences by pumping heavy mud down the lines and into the well. The booster line is used to inject fluid at the lower end of the riser. This accelerates the mud flow for easier transport of cuttings from the well bore to the surface.

2.2.2 Tensioner System

To prevent buckling in the riser, it is important to ensure proper tension in the riser. As the riser has a small diameter relative to its length, buckling may occur if the riser is compressed. A riser tensioning system is thus used to provide sufficient tension. The tensioner system counteracts the weight of the riser by providing tension as the drilling vessel heaves.

Modern riser tensioners are complex hydro-pneumatic systems. The purpose is to make the riser tension constant, however this is far from the reality [10]. Concerning a fatigue

assessment of well drilling components, it is important to capture the real non-linear variation in tension. The most common way to model the tensioner system is by applying constant tension or a linear spring. Williams and Greene [10] investigated the effect of implementing a detailed tensioner model contra a simplified model in a fatigue assessment of drilling components. One of the cases that were studied was a low pressure wellhead housing weld with a nominal positioned vessel during drilling conditions. The fatigue life was calculated to be 4.2 and 2.5 years for the simplified and detailed model respectively. In other words, the improved model corresponds, in this case, to a 40 % reduction in fatigue capacity.

2.2.3 Blowout Preventer Stack

As mentioned in section 2.1.1, a BOP stack is used when drilling the intermediate and reservoir sections. The purpose of the BOP is to control a potential blowout by cutting the drill string and sealing the bore.

Although the BOP is an essential component in the drilling system, it exposes the wellhead system to great loads. In the early 1980s, the common height of a BOP was 12 to 14 meters and wet weight 125 to 160 tonnes. In the later years the typical height and weight of BOP stacks has increased due to a higher safety focus. Now, typical wet weight and height is 270 to 365 tonnes and 14 to 15.5 meters, respectively [15, 16]. It follows when the BOP size increases, the importance of BOP dynamics increases. Dynamic response of the BOP may contribute greatly to wellhead fatigue. The BOP may in some cases experience a cantilever type eigenmode resulting from global flexibility of the wellhead [6]. A heavier BOP stack will increase the BOP/wellhead systems natural period and make it more susceptible for dynamic effects from wave loads.

The BOP stack is divided into two main modules. The upper part, LMRP, and the bottom part, ram-preventer

Lower Marine Riser Package

The LMRP comprises an annular BOP, a control pod, a flex joint and a LMRP connector. The annular preventer is designed to seal the space between the drill pipe and the wellbore, also known as the annulus. To seal this space, a rubber ring is squeezed inwards against the pipe.

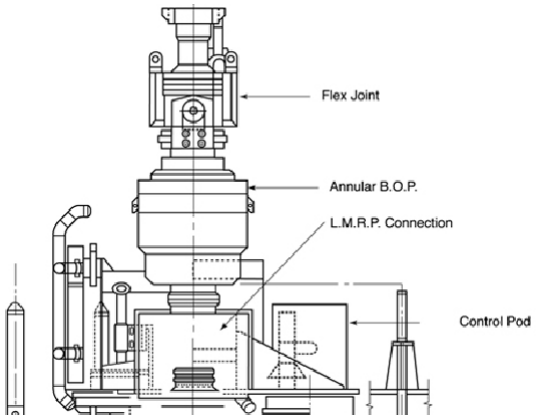

Figure 2.3: Upper BOP stack - LMRP [17]

Ram-preventers

Commonly the BOP stack consists of two or more pipe ram-preventers and one blind shear ram-preventer. The ram-preventers are designed to enclose the drillpipe and seal the annular space while the blind shear rams should seal the wellbore and cut the drillpipe. Some BOPs also comprise casing shear rams which may cut through thick walled pipes.

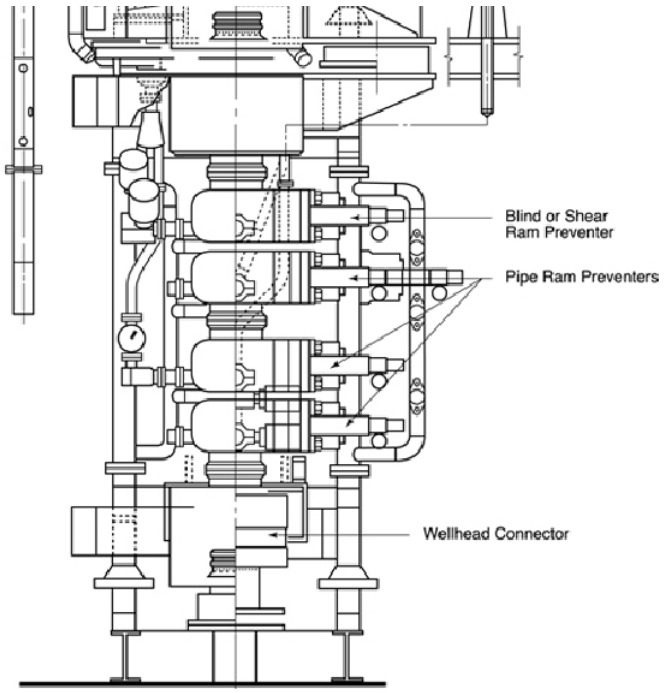

Figure 2.4: Lower BOP stack - RAM preventer [17]

2.2.4 Joints and Connectors

Flex Joint

A drilling system commonly comprise of a lower flex joint and an upper flex joint. The flex joint make up the topmost part of the LMRP. The joint allows the riser to rotate with minimal motion induced stresses. It consists of a metal body with elastomer flex elements. The center passage has to be equal to or larger then the pipe diameter. The elastomer elements provides stiffness to the riser when it rotates which minimizes stress concentrations near the couplers. Concerning a mathematical model, the joint may be modelled as a radial spring with specified stiffness.

Slip Joint

The slip joint is also known as telescopic joint. It consists of two concentric pipes that move relative to each other. The joint is situated on top of the riser and is connected to a tension plate which is again connected to the riser tension system. This allows the drill pipe and riser to move independent of each other without inflicting damage.

Riser joint connectors

To connect the riser joints several types of connectors may be used. As the water depth increases, issues like high external pressure and high bending moments are of particular concern [18]. The type of connector chosen will affect the riser's properties in many ways, where important factors are axial, pressure, bending loads and fatigue [18].

Wellhead connector

Wellhead connectors are used to couple the wellhead to the BOP stack and are complex with interacting parts. Commonly the wellhead connectors are bolted to the BOP or XT before installation. When the BOP or XT is lowered onto the wellhead, the connector is coupled to the wellhead by hydraulically actuated locking dogs.

2.2.5 Wellhead System

Drilling a subsea well from a floating drilling rig requires a subsea wellhead system. The system is installed gradually during the drilling process, starting with a guidebase or template. The subsea wellhead system comprises mainly of:

- ◇ Guidebase/Template
- ◇ Low pressure housing
- ◇ High pressure housing / Wellhead housing
- ◇ Casing hangers

For the remainder of the thesis, when referring to the term wellhead, this means subsea wellhead system. A wellhead serves several purposes:

- ◇ Support the blowout preventer (BOP) and seal the well during drilling
- ◇ Support and seal the production tree
- ◇ In some cases, to support and seal the production tubing hanger

The wellhead, together with the BOP or XT, provides the means to safely contain reservoir pressure during drilling and production. Wellheads must be designed for high structural loads imposed during drilling, workover or well completion operations. In addition it must support the casing weight and it must also be able to withstand forces imposed by internal pressure [19].

Chapter 3

Fatigue of Marine Structures

3.1 Wellhead Fatigue in General

The fatigue capacity of a system can be defined as the system's ability to accommodate cyclical loading before experiencing failure. For a typical wellhead system, cyclical loading will result in the growth of flaws which are present in the system from the time of manufacture. Once the flaw reaches a certain critical size, a failure can be considered to have occured [20].

A wellhead is typically subjected to cyclical fatigue loads due to environmental forces. For all practical purposes, the environmental forces acting directly on the wellhead are negligible. However, environmental forces acting on the drilling vessel and the marine drilling riser are transmitted along the riser and onto the wellhead. This is seen clearly in figure 3.1 below. These forces will be elaborated in chapter 4.

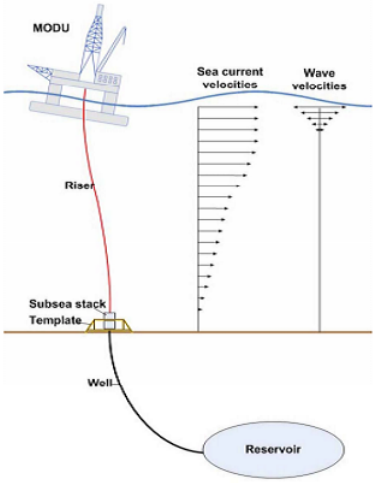

Figure 3.1: Overview of forces on subsea stack [11]

A problem which is faced during drilling and completion operations is that if vessel

offsets and riser tensions are not carefully controlled, excessive bending loads can be imposed to the wellhead. Depending on the magnitude and repetition of these loads, the wellhead may be subjected to damage. From figure 3.2 it is seen that when there is vessel offset, an angle between the riser and BOP stack can impose large loads in the wellhead. It is noted that figure 3.2 represents a workover system.

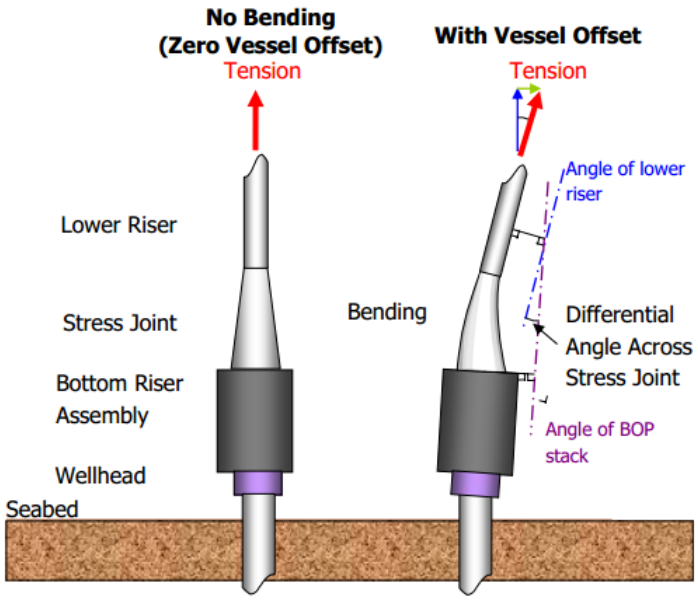

Figure 3.2: Lower riser and wellhead during workover [21]

.

As mentioned, overloading of a wellhead can be caused by excessive bending moments as a consequence of large vessel offsets and extreme currents during completion and work over activities. Damage can also be caused by cyclical fatigue loads.

A particular concern related to fatigue loading, is the boundary conditions of the wellhead. As mentioned in section 2.2.5, one of the main purposes of the wellhead is to transfer loads from the BOP and riser to the soil. Thus the soil properties becomes an important factor in relation to which stresses that occur in the wellhead. The most important soil factor is the stiffness. Common practice for obtaining the soil stiffness that corresponds to the wellhead location is by the application of pressure-displacement curves (P-Y curves). For the determination of the P-Y curves the following standards are applicable: ISO 19901:4 [22], ISO 19902 [23] and API RP2A [24]. These codes outline different procedures on how to calculate the P-Y relation depending on which kind of soil is present.

Fatigue data may be divided into two different groups dependent on how many cycles are required for collapse of the structure. The low cycle range represents the event where collapse occurs for less than 10^5 cycles, and the high cycle for above 10^5 cycles. In the low cycle range the structure undergoes cyclic plasticity, while in the high cycle range the stress is essentially elastic. Due to limits in terms of operation window when drilling, the loads acting on the system will impose essentially elastic stresses. Hence, the high cycle range is most relevant and will be considered further.

3.2 Fatigue Loading

When conducting a fatigue analysis of a structure the acting stress over time is of interest. Since the acting stress is calculated on basis of the loading, the nature of the loading must be thoroughly examined. Commonly the loading comprises combinations of shear force and moment. In the case of environmental loading, the loading may be may be considered as a stochastic process as shown in figure 3.3. A challenge in relation

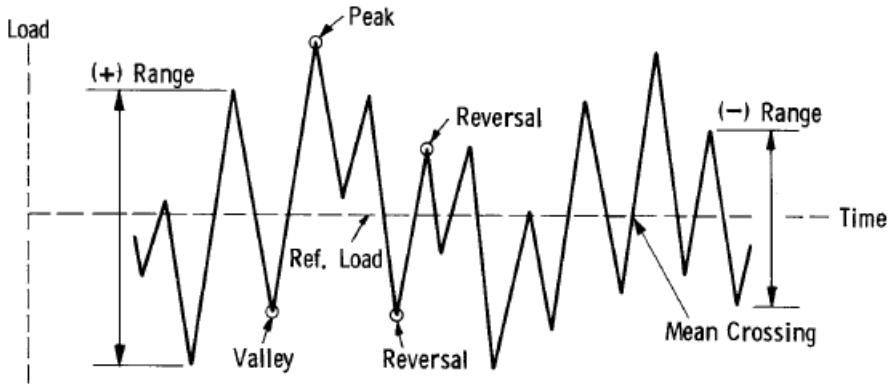

Figure 3.3: Stress vs Time [25]

to calculation of stochastic loading is the fact that different load amplitudes have a corresponding probability of occurrence. When calculating the variation in stress due to stochastic loading, it follows that the acting stress in the structure will also be of stochastic nature. Since fatigue damage is calculated on the basis of stress variations, any calculated damage for environmentally loaded structures will have a probabilistic dependency.

As seen in figure 3.3, different terms apply for stochastic processes. The terms which will be used further [25]:

- ◇ Peak: A point where the sign of the derivative of the time history changes from positive to negative
- ◇ Valley: A point where the sign of the derivative of the time history changes from negative to positive
- ◇ Range: Difference between valley and peak. Often written as stress or load peak, depending on the process referred to.

3.3 SN Curves

In the period from 1850 to 1875 August Wöhler did a research on fatigue of railway roads. He discovered that cyclic stress over time reduced the design lifetime of the railway. This introduced the SN curve, which is a stress-lifetime relationship. SN plots usually consist of a very large number of cycles and it is thus plotted on a log-log format. A typical SN curve for constant amplitude loading is shown in figure 3.4

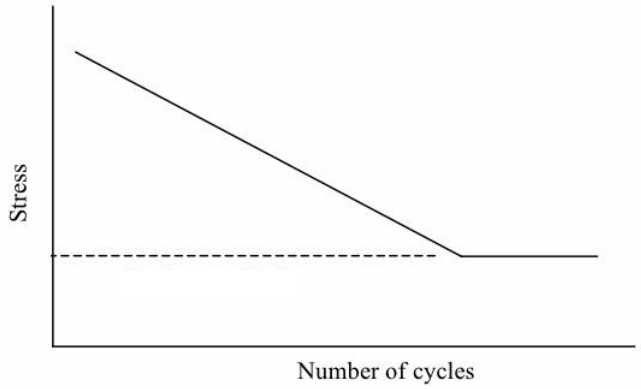

Figure 3.4: Typical SN curve [26]

For the log-log format the SN curve tends to follow a linear relationship [27]:

$$N(\Delta S)^m = \text{constant}$$

As seen in figure 3.4 the curve follows this relationship until the fatigue limit which is represented by the horizontal line. Stress ranges beneath this value will not contribute to fatigue damage.

3.3.1 SN Curves for Variable Amplitude Loading

A particular interest in this thesis is the fatigue life of welded joints subjected to environmental loading. The SN curve in figure 3.4 represents structures subjected to constant amplitude loading, i.e. it cannot represent structures subjected to environmental loading. For the case where a structure is subjected to such loads, it follows that some loads will be above the structure's fatigue limit and some will be below. Only the loads that are above this limit will contribute to crack growth. As the crack grows, the fatigue limit will decrease with the number of load cycles. Consequently, more cycles will become "active" and thereby start to contribute to crack growth. To include this phenomenon in SN curves, a correction must be done. One way to do this is to use the Haibach model. The model represents a fictitious extrapolation of the SN curve with a slope of $-(2m-1)^{-1}$ where m^{-1} is the slope of the initial SN curve. The result is a bi-linear SN curve.

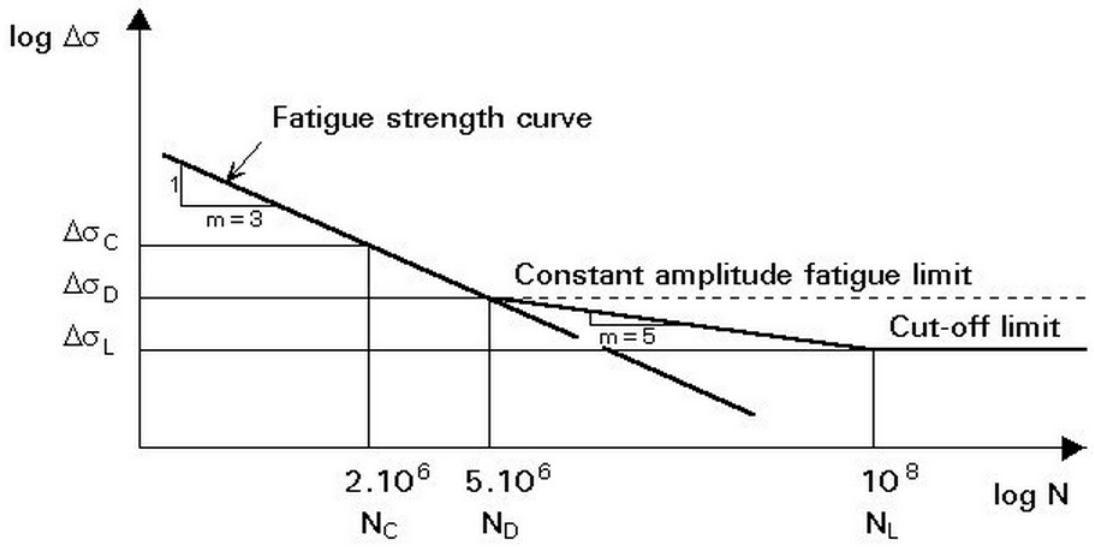

Figure 3.5: Bi-linear SN Curve [28]

The bi-linear SN curve in figure 3.5 has an initial slope of $-1/3$ and thus the second slope, using the Haibach model, becomes $-1/5$.

3.4 Fatigue Damage

Damage to a structure caused by cyclic fatigue loading may be divided into three phases:

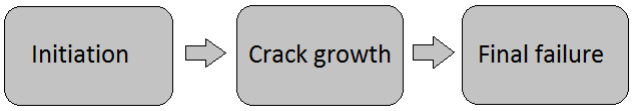

Figure 3.6: Fatigue damage stages

The initiation and crack growth phases make up the total fatigue life of the component. The number of cycles in each phase is strongly dependent on the type of component under consideration. For smooth, un-welded, machined components, the initiation phase make up a major part of the fatigue life. For a welded joint the crack growth phase is most dominating.

Regarding crack initiation of machined components with a smooth surface, the initiation is often a result of a development of slip bands. The surface of the material contains a large number of grains, and some of these may have a lower yield strength than the matrix material. When a structure is subjected to cyclic stress this may result in an extrusion and an intrusion on the surface of the material. This is known as stage one crack growth. Since the initiation is governed by the yield limit, Von Mises stress should be used as input to fatigue calculations in this stage [3].

For welded joints the fatigue strength is governed by "ab initio[1]" defects. Typical defects are listed below [27]:

- Undercut
- Lack of fusion
- Poor weld profile
- Root defect
- Lamellar tearing
- Lack of penetration
- Hydrogen cracking
- Solidification cracking

[1] ab initio: from the beginning

As mentioned above, the crack growth phase make up the major part of the fatigue life of a welded joint. Still, an extension of the total fatigue life of the component can be done by applying post-weld treatments like peening and grinding of the weld toe. This will introduce an initiation phase and prolong the overall life.

Crack growth which is caused by high cycle fatigue is associated with stress levels well below the materials yield limit. For this reason, crack growth parameters may be quantified be linear elastic fracture mechanics (LEFM). Crack growth rate may be divided into three regions; A, B and C.

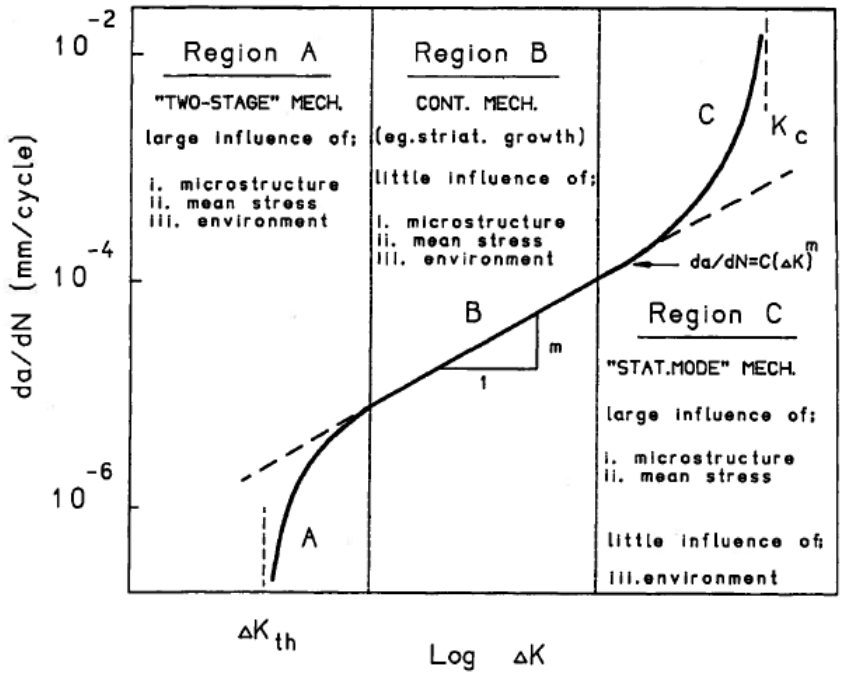

Figure 3.7: Crack growth regions [27]

The crack growth rate, vertical axis in figure 3.7, is represented by $\frac{\mathrm{d}a}{\mathrm{d}N}$ where da represents change in crack length and dN the corresponding number of cycles. The crack growth rate is a function of the stress intensity factor, ΔK which is defined as follows:

$$\Delta K = \Delta S \sqrt{\pi a} F \tag{3.1}$$

Where ΔS represents nominal stress range, F is a geometry dependent form function and a represents the crack length. Region A, the threshold region, represents crack

growth in the vicinity of the fatigue limit. Stress ranges which represent a stress intensity factor below the threshold, K_{th}, will not contribute to crack growth. Region C is known as the final failure region where the crack length increases rapidly until fracture. Conservative fatigue assessments often involves an assumption of failure when the crack enters into this region.

Region B represents stable crack growth. As seen in figure 3.7, the region is given as a linear relationship between stress intensity factor and crack growth rate. The relation is known as the Paris law:

$$\frac{\mathrm{d}a}{\mathrm{d}N} = C(\Delta K)^m \tag{3.2}$$

Where C and m are material parameters. The constant m is known to be equal to the negative inverse slope of SN curves. As decried in section 3.3, the finite life region of SN-curves is represented by $N(\Delta S)^m = \text{constant}$. This implies that the Paris law region, region B, coincides with the finite life region of SN curves.

3.5 Cumulative Damage Assessment

Cumulative damage assessments are carried out to determine how many stress cycles structures are able to resist before failure. For some cases the cumulative damage may be represented in terms of an estimated fatigue life. Structures that are exposed to loading of stochastic nature, this will however be probability dependent. In other words will a predicted lifetime correspond to a predicted loading. Another way to present fatigue damage is by percentual remaining fatigue capacity. Regardless of presentation format, it is essential to keep in mind the that different load amplitudes will have different contribution to the fatigue damage.

In general, the main input to a cumulative damage assessment is stress-to-time series for a given hot spot on the structure. The first step in the assessment is to process the data so it may be presented as stress ranges.

3.5.1 Cycle Counting

In the cumulative damage assessment, the calculated stress cycles must be counted and summed up as stress ranges. For constant amplitude loading, the counting is

a simple process. As for variable amplitude loading, the matter is more advanced. Different methods are applicable for counting of variable amplitude loading induced stress histories. One of the most common methods is rainflow counting;

The main idea behind rainflow counting is to consider the stress/strain-time history as rain flowing down a pagoda roof. General rules that applies may be summarised as [27]:

- ◇ The rain will flow down the roof initiating at the inside of each peak or valley. When it reaches the edge it will drip down.
- ◇ The rain is considered to stop, and a cycle is completed, when it meets another flow from above.
- ◇ Starting from from a peak, the flow also stops when it comes opposite a more positive peak than that from which it started. Starting from a valley, the flow stops when it comes opposite a more negative valley than that from which it started.

From these rules a rainflow plot is made:

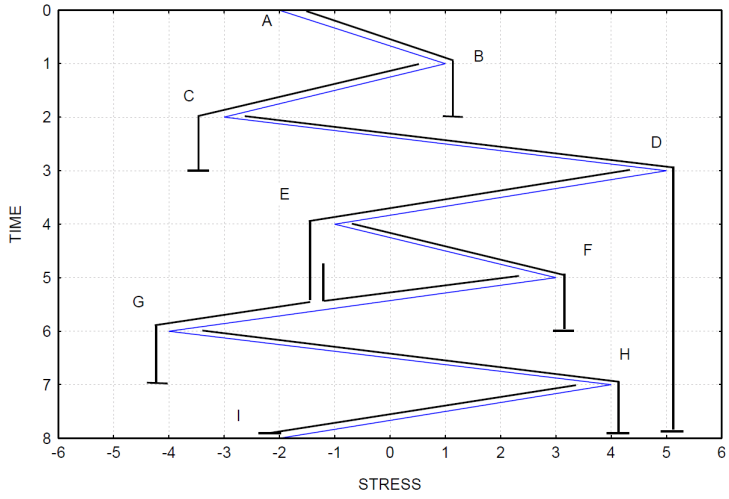

Figure 3.8: Rainflow plot [29]

From the plot, the paths are divided into stress ranges based on the corresponding stress difference, e.g. path B-C in figure 3.8, the stress range is equal to 4 and represents a half cycle.

3.5.2 Stress Range Spectra

The use of stress range spectra is a common way to represent irregular load histories. The stress range spectra is presented as blocks characterized by stress range, $\Delta\sigma_i$, and the number of corresponding cycles, n_i. Figure 3.9 shows a stress range spectrum as well as the corresponding actual "real life" spectrum.

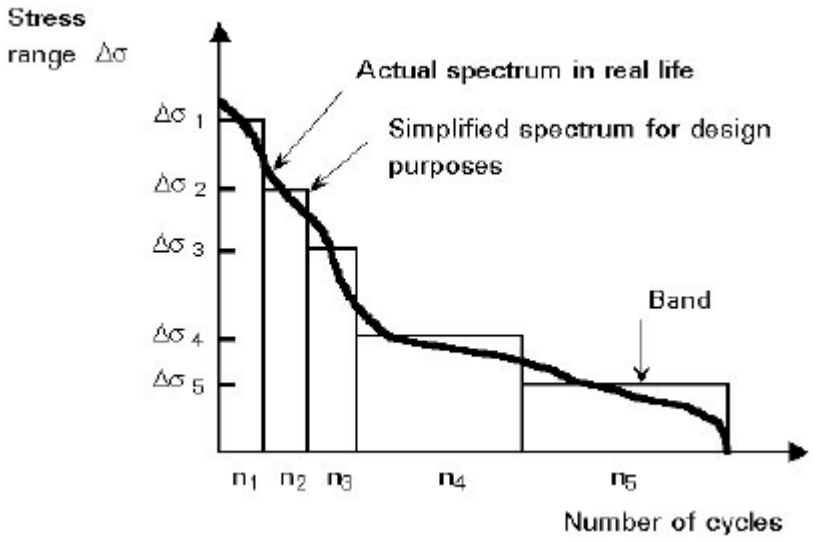

Figure 3.9: Stress Range Spectrum [30]

3.5.3 Palmgren-Miner Summation

Cumulative fatigue damage on structures may be calculated by different methods. The most common way to carry out a fatigue damage calculation is by Miner summation. Due to its simplicity and reasonable accuracy, Miner summation make up the basis for virtually all fatigue design of steel structures [27]. The Palmgren-Miner sum is known as:

$$D = \sum_i \frac{n_i}{N_i} \tag{3.3}$$

The summation is done for i stress ranges and n_i represents the number of cycles accumulated at the given stress level and N_i is the average number of cycles to failure at the same stress level. Further, the Palmgren-Miner rule is defined as: *"Fatigue failure is expected when the Miner sum reaches unity"* [31], i.e. the failure criterion using the

Palmgren-Miner rule becomes:

$$D_{\text{failure}} \geq 1.0 \tag{3.4}$$

Concerning a design situation, this rule is often applied with a correction factor. In DNV-OS-C101 [32] this factor is defined as "Design fatigue factor" or DFF. Regarding wellhead fatigue analyses, the DFF should account for probability of failure, consequences of failure and the degree of inspection possibilities. The rule reads:

$$D_{\text{failure}} \cdot \text{DFF} \geq 1.0 \tag{3.5}$$

3.5.4 Closed Form Approach

A simplified closed form fatigue damage approach may be carried out instead of the Miner-Palmgren approach if the stress range distribution fits a two-parameter Weibull distribution,. This method is presented in DNV-RP-C203 [31] as an alternative method. The closed form approach is derived from the Palmgren-Miner summation. The Weibull distribution for stress ranges may be written as:

$$Q(\Delta\sigma) = \exp\left[-\left(\frac{\Delta\sigma}{q}\right)^h\right] \tag{3.6}$$

$$q = \frac{\Delta\sigma_0}{(\ln n_0)^{1/h}} \tag{3.7}$$

where

$Q(\Delta\sigma)$: Probability of exceedence of the stress range $\Delta\sigma$

q : Weibull scale parameter

h : Weibull stress range shape distribution parameter

$\Delta\sigma_0$: Largest stress range out of n_0 cycles

Further, the equation for fatigue damage calculated on closed form becomes:

$$D = \frac{\nu_0 T_d}{\overline{a}} q^m \, \Gamma\left(1 + \frac{m}{h}\right) \tag{3.8}$$

where

T_d : Design life in seconds

q : Weibull stress range scale distribution parameter

ν_0 : Average zero-crossing frequency

$\Gamma\left(1+\frac{m}{h}\right)$: Gamma function

Equation 3.8 is though only applicable for single slope SN curves.

If fatigue damage has been calculated directly by Palmgren-Miner summation or the closed form approach, it is possible to obtain a predicted fatigue life. The calculation is dependent on the fatigue damage, D, and the corresponding time frame which the stress cycles act within, e.g. if the stress cycles has been extracted from a process of one hour, the predicted fatigue life, in hours, becomes:

$$\text{Fatigue life} = D^{-1} \tag{3.9}$$

It must though be kept in mind that the fatigue life is only valid if the exact same loading acts through the entire lifetime of the structure. For marine structures a wide range of loading characteristics will act on the system. A single one hour analysis will thus not be representable. Instead analyses may be conducted for all expected sea states. The values calculated for the respective sea states should be weighted with the sea states probability of occurrence for each sea state. The weighting may be applied before and after the Palmgren-Miner summation depending on how the fatigue data is organized. For weighting after the Palmgren-Miner summation, the fatigue damage for each individual sea state is multiplied with the probability of occurrence for the given state. The probabilities may be calculated from a wave scatter diagram.

Chapter 4

Loads on a drilling system

A drilling system is subjected to a variety of environmental loads. figure 4.1 shows the loads that contribute to fatigue damage in a subsea wellhead.

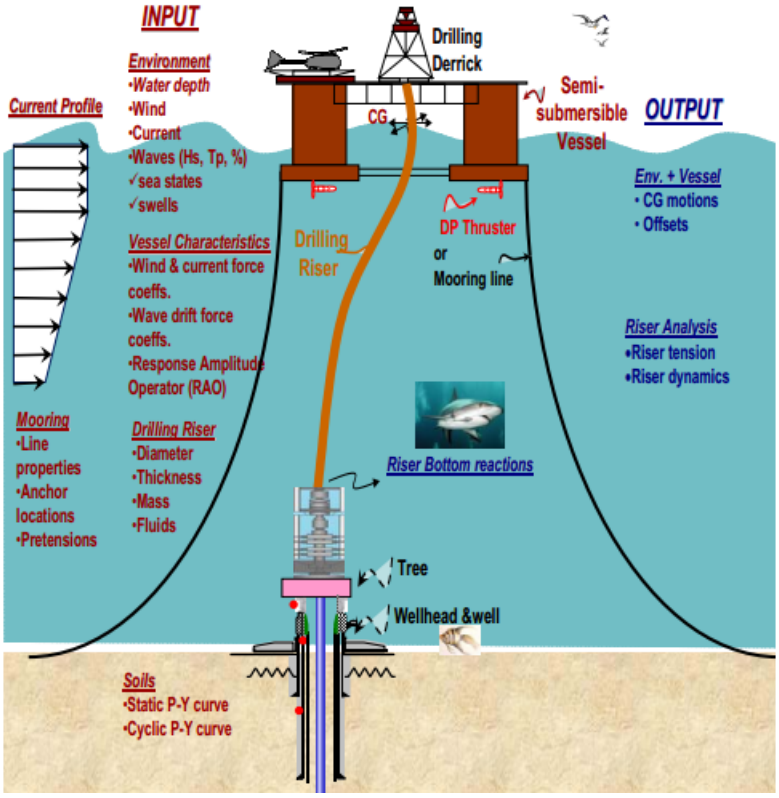

Figure 4.1: Overview of environmental loads and parameters [33]

As mentioned in section 3.1, the loads and forces acting directly on the wellhead stack are considered negligible. When drilling a well, a MODU is connected to the BOP stack and wellhead system through a riser. Thus, environmental forces acting on the MODU and the marine drilling riser are transmitted along the riser and onto the wellhead. These forces are regarded as acting indirectly on the wellhead system. They are dependent

on the hydrodynamic properties of the MODU, riser and the environmental conditions during the operation [7]. In a fatigue context, the dynamic loads are of most interest. Lastly, vortex induced vibrations generally becomes the governing environmental load on drilling risers in water depths exceeding 250 metres [34] and thus contributes greatly to wellhead fatigue. This phenomenon will be explained.

4.1 Waves, Wind & Current

The main contributors to dynamic loading of the drilling system are waves, wind and current.

4.1.1 Waves

It is fair to assume that the wave amplitudes are much smaller compared to the wave lengths, λ, in the ocean where drilling operations take place. This assumption allows employment of regular wave theory. Applying the superposition principle on a range of regular waves gives rise to the generation of sea states resembling the physical reality at sea.

Regular waves

Regular wave theory is based on the assumption of a horizontal seabed and a free surface of infinite horizontal extent. Regular wave theory is also based on potential flow theory, which assumes sea water as an incompressible, inviscid and irrotational flow. From these assumptions, the velocity potential for the wave is derived, solving the Laplace equation. The velocity potential, ϕ, describes the fluid velocity vector $\vec{V}(x, y, z, t) = (u, v, w)$ for a regular wave. For a regular wave in finite water depth, the velocity potential can be written according to Faltinsen [35]

$$\phi_0 = \frac{g\zeta_a}{\omega} \frac{\cosh k(z+d)}{\cosh(kd)} \cos(\omega t - kx) \tag{4.1}$$

where ζ_a is the wave amplitude, g is the acceleration due to gravity, k is the wave number and ω is the wave incident wave frequency. The parameters d and z are not to be confused, and are overall water depth and position in the vertical plane respectively.

Origin is commonly placed at the free water surface. The dispersion relationship for finite water depth, in which the wave number k is found, is

$$k = \frac{g}{\omega^2} \tanh(kd) \tag{4.2}$$

so it is apparent that an iteration procedure is required to find k. It is noted that equation 4.1 is valid regardless of water depth, however, simplifications can be made to make a cleaner expression by assuming shallow[1] or deep[2] water. These simplifications will also affect the wave number k in such a way that iteration will no longer be required in order to determine it, but these simplifications are not included here.

Differentiating the velocity potential once in the spatial plane, (x, y, z), gives the wave particle velocities in the respective directions. Differentiating once more, with respect to time, gives the wave particle accelerations. For x-direction

$$u = \frac{g\zeta_a k}{\omega} \frac{\cosh k(z+d)}{\cosh(kd)} \sin(\omega t - kx) \tag{4.3}$$

$$\dot{u} = g\zeta_a k \frac{\cosh k(z+d)}{\cosh(kd)} \cos(\omega t - kx) \tag{4.4}$$

and similarly can be derived for y-direction. For z-direction

$$w = \frac{g\zeta_a k}{\omega} \frac{\sinh k(z+d)}{\cosh(kd)} \cos(\omega t - kx) \tag{4.5}$$

$$\dot{w} = -g\zeta_a k \frac{\sinh k(z+d)}{\cosh(kd)} \sin(\omega t - kx) \tag{4.6}$$

The wave elevation, ζ, is considered to be a sine wave propagating in positive x-direction

$$\zeta = \zeta_a \sin(\omega t - kx) \tag{4.7}$$

The wave elevation causes a dynamic pressure and the magnitude of the pressure is water depth dependent. The dynamic pressure for finite water depth is

$$P_D = \rho g \zeta_a \frac{\cosh k(z+d)}{\cosh(kd)} \sin(\omega t - kx) \tag{4.8}$$

The dynamic pressure is derived from the pressure term in Bernoulli's equation. Bernoulli's

[1] Shallow water: $h < 0.05\,\lambda$

[2] Deep water: $h > 0.5\,\lambda$

equation governs the majority of the potential flow theory along with Laplace's equation and the appurtenant boundary conditions and assumptions. They are however not included here. The dynamic pressure is negative under a wave through and positive under a wave crest.

Irregular waves

As mentioned, regular waves form the basis for generating irregular waves. The wave elevation of a long-crested irregular wave is represented as a sum of a large number of regular waves, where each regular wave component has a random phase angle ϵ_i [35].

$$\zeta = \sum_{i=1}^{N} \zeta_{a,i} \sin\left(\omega_i t - k_i x + \epsilon_i\right) \tag{4.9}$$

Based on previous experience one shall not use less than 150 frequency components to represent the wave spectrum [3], meaning $N \geq 150$. Further, the wave amplitudes, $\zeta_{a,i}$, may be determined by the wave spectrum characterizing the sea state.

Wave spectrum

The frequency decomposition of the sea state is represented by a wave spectrum, $S(\omega)$. The relation between the spectrum and the wave amplitude is in Faltinsen [35] expressed as

$$\zeta_{a,i} = \sqrt{2S(\omega_i)\Delta\omega} \tag{4.10}$$

where $\Delta\omega$ is the increment over the frequency interval in the wave spectrum. figure 4.2 below illustrates the superposition principle of modelling an irregular wave, as well as the relationship between the frequency domain and time domain.

Finally, the shape of the wave spectrum, $S(\omega)$, needs to be fitted by a curve, the covariance function. The most commonly used and recommended spectral density representations are the modified Pierson-Moscowitz and JONSWAP spectra, based on Gaussian and Rayleigh distributions. The PM spectrum has been developed through measurements in the North Atlantic. The assumption is that if wind blows steadily for a long time over a large area, the waves would come into equilibrium with the wind, and

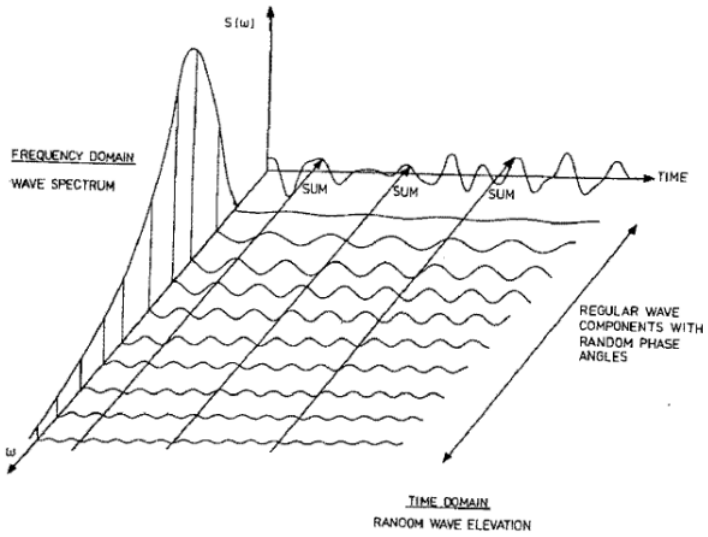

Figure 4.2: Wave generation principle [35]

thus the spectrum defines a fully developed sea. From *DNV-RP-C205* [36] it is defined

$$S_{PM}(\omega) = \frac{5}{16} H_s^2 \, \omega_p^4 \, \omega^{-5} \, \exp\left(-\frac{5}{4}\left(\frac{\omega}{\omega_p}\right)^{-4}\right) \tag{4.11}$$

where H_s is significant wave height and ω_p is peak wave frequency. JONSWAP is in contrast to PM, never fully developed. The assumption is that a sea which continues to develop through non-linear, wave to wave interactions for long periods of time and distances. JONSWAP spectrum is defined in DNV [36]

$$S_J(\omega) = A_\gamma \, S_{PM}(\omega) \, \gamma^{J_p} \tag{4.12}$$

In equation 4.12, A_γ is a normalizing factor given as

$$A_\gamma = 1 - 0.287 \ln(\gamma)$$

and γ is a non-dimensional peak shape parameter and σ is a spectral width parameter that depends on the wave peak frequency ω_p. Finally, the exponent J_p is given as

$$J_p = \exp\left(-\frac{1}{2}\left(\frac{\omega - \omega_p}{\sigma \, \omega_p}\right)^2\right)$$

The PM spectrum is commonly referred to as a broad-banded spectrum, while the

JONSWAP spectrum is referred to as a narrow-banded spectrum. This is illustrated in figure 4.3 below. In studies and analyses, it is common to consider waves propagating

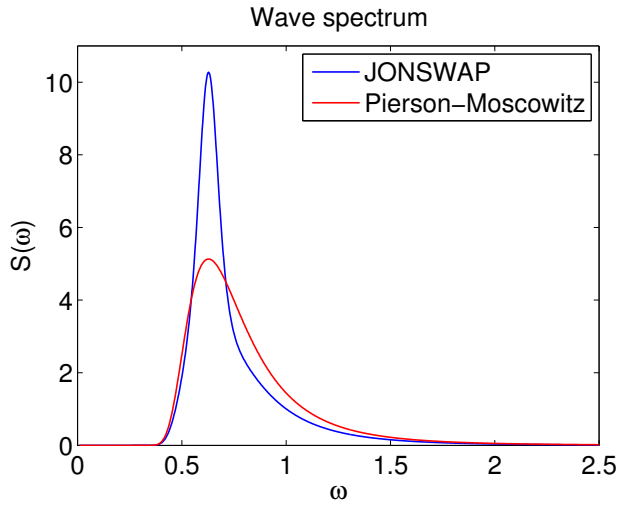

Figure 4.3: Pierson-Moscowitz and JONSWAP spectra

in arbitrary directions. This will terms to the expression for the velocity potential, ϕ, and consequently all expressions that are derived from the velocity potential.

4.1.2 Current

There are several independent phenomena responsible for the occurrence of current: the ocean circulation system resulting in a steady current, the cyclical change in lunar and solar gravity causing tidal currents, wind and differences in sea water density [37]. Current on moored structures is of particular interest, and is as well also important for VIV calculations on risers. The forces and moments exerted by current on a floating object is composed of

- ◇ A viscous part, due to friction between the structure and the fluid, and due to pressure drag
- ◇ A potential part, with a component due to a circulation around the object, and one from the free water surface wave resistance

A rule of thumb recommends that a total current velocity for design analyses of offshore structures in the North Sea is $1\,\mathrm{m\,s^{-1}}$, although when carrying out a fatigue analysis, an estimate like this is not necessarily adequate. This was highlighted by Williams

and Greene [10], where the influence of current profile selection on fatigue damage estimates was investigated. They performed VIV calculations on a riser in two ways. One by applying a statistical determined current profile, such as recommended by DNV, and one by use of accurately measured current data set from site. The analyses with both current profiles predicted the same location for VIV fatigue and similar damage distribution. However, the accurately measured current profile predicted a much less conservative fatigue life.

4.1.3 Wind

Like all environmental phenomena, wind has a stochastic nature which greatly depends on time and location. Wind is usually characterized by fairly large fluctuations in velocity and direction [37]. In some cases gust winds can excite resonant oscillations of offshore structures, of which slow-drift horizontal motion of moored structures is an example.

4.2 Load and Response

There are many environmental loads acting on a drilling system, as was seen on figure 4.1. To represent them in analyses, the wave loads are broken down into first order effects and higher order effects. Vessels in irregular waves are subjected to large, so-called first order, wave forces and moments which are linearly proportional to the wave amplitude and contain the same frequencies as the waves [38]. Further, they are subjected to small, higher order effects, which are proportional to the square and cube of the wave amplitude. In many scenarios, the higher order effects are of less importance to the analysis. However, higher order effects are in some cases the main contributor to excitation as they lie in the natural frequency domain of the vessel in question.

4.2.1 First Order Effects

One advantage of first order theory, or linear theory as it is often referred to, is that it is possible to obtain results in irregular waves by superposing regular waves of different amplitudes, wavelengths and propagation directions shown in equation 4.9. Another

advantage of first order theory is that response of the incident waves can be broken down to response to each wave component from equation 4.9. Since the incident wave is harmonic, then the response will also be harmonic. From Faltinsen [35] it follows that the response to each wave component can be written

$$\zeta_{a,i} \left| H(\omega_i) \right| \sin\left(\omega_i t + \delta(\omega_i) + \epsilon_i\right) \tag{4.13}$$

where $|H(\omega_i)|$ is a transfer function, known also as the response amplitude per unit wave amplitude. It is also noted that there is a phase angle, $\delta(\omega_i)$, between the incident wave and the response. Like regular wave components, the response components can also be superposed

$$\sum_{i=1}^{N} \zeta_{a,i} \left| H(\omega_i) \right| \sin\left(\omega_i t + \delta(\omega_i) + \epsilon_i\right) \tag{4.14}$$

Next, it follows that since it is possible to obtain results in irregular seas by linearly superposing regular wave components, it is sufficient to analyse a structure's response to incident regular wave components of small wave steepness [35]. Regarding response analysis the hydrodynamic problem is commonly divided into two sub-problems.

Diffraction problem

The first sub-problem is to consider the structure being restrained from oscillations and that loads from incident waves are acting on the structure. These loads are called wave excitation loads, composed of Froude-Kriloff and diffraction forces and moments.

Radiation problem

The second sub-problem is to consider the structure being forced to oscillate, but with no incident waves. The hydrodynamic loads that rise here are identified as added mass, damping and restoring forces and moments. Due to linearity, the forces and moments from the two sub-problems respectively can be added together to give the total hydrodynamic forces and moments, see figure 4.4. Added mass, damping and restoring moments and forces as well as Froude-Kriloff and diffraction forces and moments are not discussed further, though it is mentioned that Froude-Kriloff and diffraction make up the mass force term in Morison's equation.

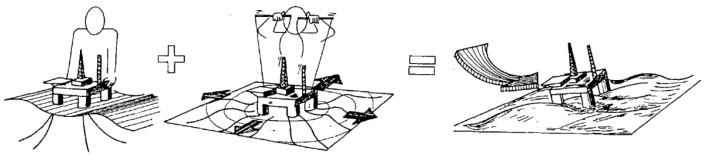

Figure 4.4: Sub-problems - Linear hydrodynamics [35]

Morison's equation

The horizontal force per unit length on a strip of a cylinder, can, according to Morison *et al.* [39], written as

$$\mathrm{d}F = \rho \frac{\pi D^2}{4} C_M \dot{u} + \frac{\rho}{2} C_D \, D \, u \, |u| \tag{4.15}$$

where D is the cylinder diameter, u and $\dot{u}$ are the wave particle velocity and acceleration as seen in equation 4.3 and 4.4. Further, ρ is water density and C_M and C_D are mass and drag coefficients. Equation 4.15 yields a good estimation of forces on semi-submersible cylinders piercing the surface. However, since the riser is long and slender, it is reasonable to assume that it will start to oscillate in the water due to the incident waves and current. To account for this, the Morison's equation can be rewritten. From Faltinsen [35], with a modification with respect to current velocity, the horizontal force per unit length is

$$\mathrm{d}F = \frac{\rho}{2} C_D \, D \, (u + u_c - \dot{\eta}_1) \, |(u + u_c - \dot{\eta}_1)| + \rho \frac{\pi D^2}{4} C_M \, \dot{u} - \rho(C_M - 1) \frac{\pi D^2}{4} \ddot{\eta}_1 \tag{4.16}$$

Here η_1 is the riser's horizontal rigid body motion, u_c is the current velocity. Further it is noted that Morison's equation cannot predict at all the oscillatory forces due to vortex shedding in the lift direction. This will in short be explained in section 4.3.1.

Wind loads on a semi-submersible

The wind forces on a semi-submersible can be approximated by dividing the structure into a number of components, where the components are desired to resemble elementary geometry, such as spheres, flat plates, cylinders and so on. The wind force can then be estimated for each element. Drag coefficients for elementary geometry is given in standards, e.g in DNV [36]. The total wind load is found by adding the contributions from all the individual components [37].

4.2.2 Higher Order Effects

Linear theory implies that the response oscillates at the same frequency as the input, meaning if an incident wave has the frequency ω_i, then the response of the structure will also be ω_i, though often with a phase angle. A semi-submersible has natural periods at around 20 seconds in heave and 1 to 2 minutes in surge and sway. Referring to figure 4.3, it is easy to see that there is hardly any wave energy at these periods. However, response at these periods have been observed and measured meaning it points to the presence of higher order(non-linear) force mechanisms [40], which will be given attention here.

In linear theory, the quadratic velocity term is excluded in Bernoulli's equation. However, including it is a simple way to illustrate the presence of non-linear wave effects [35]. The quadratic velocity term for fluid pressure in x-direction can be written as

$$P = -\frac{\rho}{2}\overrightarrow{V_x^2} \tag{4.17}$$

where $\overrightarrow{V_x}$ is the fluid velocity vector in x-direction. Next, consider an idealized sea state consisting of two wave components of circular frequencies ω_1 and ω_2 propagating in x-direction. The velocities can be approximated such that

$$\overrightarrow{V_x} = A_1 \cos(\omega_1 t + \epsilon_1) + A_2 \cos(\omega_2 t + \epsilon_2) \tag{4.18}$$

Inserting equation 4.18 into the right hand side of equation 4.17 and then applying trigonometric identities gives

$$\begin{aligned} P = -\frac{\rho}{2}\Bigg[&\frac{A_1^2}{2} + \frac{A_2^2}{2} + \frac{A_1^2}{2}\cos(2\omega_1 t + 2\epsilon_1) + \frac{A_2^2}{2}\cos(2\omega_2 t + 2\epsilon_2) + \\ &A_1 A_2 \cos[(\omega_1 - \omega_2)t + \epsilon_1 - \epsilon_2] + A_1 A_2 \cos[(\omega_1 + \omega_2)t + \epsilon_1 + \epsilon_2]\Bigg] \end{aligned} \tag{4.19}$$

In equation 4.19 the term $\frac{A_1^2}{2} + \frac{A_2^2}{2}$ is a mean wave pressure term, and it is constant. On the second line of equation 4.19, the term $\omega_1 - \omega_2$ appears, meaning there is a pressure term oscillating with the frequency $\omega_1 - \omega_2$, or on a more general form, $\omega_j - \omega_k$. This is called difference frequency, and is also often referred to as slowly-varying. The terms $\omega_1 + \omega_2$, $2\omega_1$ and $2\omega_2$ also appear in the first and second line, but these are frequencies that excite floating objects with much higher natural frequencies than that

of a semi-submersible and hence are not considered further here.

Mean wave drift forces

Mean wave drift forces are caused by non-linear(second order) wave potential effects. Mean drift wave forces come from the $\frac{A_1^2}{2} + \frac{A_2^2}{2}$ term in equation 4.19. This is a constant term. Together with the mooring system, these loads determine the equilibrium position in surge, sway and yaw [37]. Viscous effects may contribute to this mean drift force, but is further neglected. One of the advantages of mean wave drift calculation is that it can be obtained without solving the second order velocity potential ϕ_2 [35]. However, as shown above, including the quadratic velocity term in the Bernoulli equation for fluid pressure results in other non-linear forces. Maruo [41] showed in 1960 that the mean drift force is proportional to the square of the reflected wave amplitude and that the wave drift force will always act in the same direction as the wave propagates.

Slowly-varying excitation forces

In the context of a semi-submersible, slowly-varying excitation forces come from the term $\omega_1 - \omega_2$ in equation 4.19. Slowly-varying wave forces and moments come from:

- ◇ Second order hydrodynamic pressure due to the first order wave
- ◇ Interaction between the first order motion and the first order wave
- ◇ Second order potential due to slowly-varying forces on body surface and free-surface

Wind loads can also invoke slowly-varying excitation loads. The slowly varying part of a wave train can be regarded as an imaginary curve joining successive wave crests or wave troughs, see figure 4.5. This figure also shows that the period of the slowly varying part of the wave train is much higher than each individual wave period. This is the part that excites the semi-submersible rigid body motions in surge and sway. Yaw can also be resonated by these slowly-varying excitation forces.

A general formula for slowly-varying excitation loads can be derived in a similar way as the expression for mean wave loads [35], however, for the slowly-varying excitation loads a contribution from the second order potential is required. Starting with equation 4.19 and generalizing it for N wave components instead of 2 components, the slowly-varying

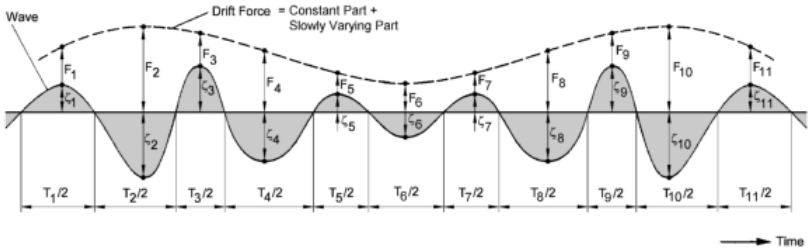

Figure 4.5: Imaginary wave envelope - Drift force frequency [37]

excitation loads in irregular waves can be formally written

$$F_i^{\mathrm{SV}} = \sum_{j=1}^{N}\sum_{k=1}^{N} A_j A_k \Big[T_{jk}^{ic} \cos\{(\omega_k - \omega_j)t + (\epsilon_k - \epsilon_j)\} + T_{jk}^{is} \sin\{(\omega_k - \omega_j)t + (\epsilon_k - \epsilon_j)\}\Big] \tag{4.20}$$

where A is the wave amplitude, ω is wave frequency and ϵ random phase angles. T_{jk}^{ic} and T_{jk}^{is} can be interpreted as second order transfer functions for the difference frequency loads and are independent of the wave amplitudes, but are functions of ω_j and ω_k [35]. Furthermore, it follows that the linear wave radiation damping is small at resonance in the slowly-varying force domain. The consequence of this can be amplifications of the slowly-varying motions. The second order transfer functions are difficult to find, and state of the art research in this area is still going on [42].

Newmans's approximation

Newman proposed an approximation to the difficult nature of slowly varying forces. This approximation reduces the CPU time significantly. Another desirable consequence is that the second order velocity potential will not have to be calculated [35]. By proposing that the coupled transfer function T_{jk}^{ic} and T_{jk}^{is} can be approximated by the uncoupled transfer functions T_{jj}^{ic}, T_{jj}^{is}, T_{kk}^{is} and T_{kk}^{ic}, this can be achieved. This approximation works because the cross coupled transfer functions do not change very much with frequency, and slowly-varying motions occur when ω_j is close to ω_k. A multitude of software uses this approximation to reduce computation time, one example being SIMO[3].

[3]SIMO is a time domain simulation program for study of motions and station keeping of multibody systems, developed at Marintek, Trondheim. http://www.sintef.no/home/MARINTEK/Software/Oil-and-Gas/

4.3 Vortex Induced Vibrations

One of the most common event related to fatigue damage in subsea equipment is the phenomenon of vortex induced vibrations (VIV) caused by current loadings [21]. Slender offshore structures like anchor lines, risers and free spanning pipelines that are exposed to current may experience vibrations [43]. These vibrations are caused by forces from vortices that are shed from both sides of the slender structure. This type of vibration is called vortex induced vibrations, VIV, and this phenomenon is a vibration at resonance. In regards to the frequency response, the classical definition of lock-in is often perceived as the regime where the frequency of oscillation and the vortex formation frequency are close to the natural frequency of the structure. However, recent studies have shown that there are high deviations from this classical result. Bodies have been seen to vibrate with large amplitude, at hundreds of times the natural frequency [44]. This emphasizes the apparent lack of complete knowledge of VIV as a phenomenon.

The phenomenon has been the cause of problems in drilling operations in the past, where it was seen that a pipe failed while drilling a well from a jack-up in the Irish Sea during the late 1970s. In 1982 there was a spectacular double failure of a subsea wellhead on a well being drilled in the Atlantic margin [45]. This demonstrates the impact from VIV induced forces on a riser in terms of fatigue damage.

Vortex induced vibration of deepwater drilling risers due to steady current flow does occur [46]. VIV of riser systems is caused by cyclic shedding of vortices in the wake of the riser under loading from ocean currents. From a safety perspective, the fatigue failure mode with the most serious consequence, is failure of the conductor below the wellhead. An example of a wellhead failure is mentioned in Hopper [47], where it was concluded that the failure was caused by VIV. Wellheads of today are fundamentally similar to those which suffered failure, emphasizing the required attention of wellhead fatigue, as well as the ability to correctly predict VIV response in computer software. Actual measured VIV response is typically less than what software predicts [46].

4.3.1 Estimation of VIV Loads

The current state of the laboratory art imposes a physical and numerical restriction on the experiments that are run. Six degree of freedom problems are reduced to *one* degree of freedom (in rare cases *two* degrees of freedom). How this reduction impacts

the calculations and simulations is still not clear, but it points to the complexity of this phenomenon [48].

In VIV analyses it is common practice to consider that the environmental loads propagate in the same direction. This direction is referred to as the in-line direction. Crossflow VIV acts perpendicular to the in-line direction and because of this, Morison's equation cannot predict at all the oscillatory forces due to vortex shedding frequency in the lift direction. In [49] Morooka *et al.* presents a method to estimate the VIV force through clever use of Morison's equation. The horizontal force per unit length from VIV

$$\mathrm{d}F_{\mathrm{VIV}} = \frac{1}{2}\rho\Big((u - \dot{\eta}_1) + u_c\Big)^2 D\,\overline{C}_L\,\cos\Big(2\pi\overline{f_s} + \varphi\Big) \tag{4.21}$$

where $\overline{f_s}$ is the average vortex shedding given by $\overline{f_s} = \frac{|\overline{U}|\,St}{D}$, St is the Strouhal number, D is the riser diameter, $\overline{U}$ is the cumulative average velocity of the oscillatory flow given by $\overline{U} = \frac{\int_{t_1}^{t_2}\Big((u-\dot{\eta}_1)+u_c\Big)\,\mathrm{d}t}{t_2-t_1}$, $\overline{C}_L$ is the average amplitude of the transversal force coefficient, u_c is the current velocity, u is the wave particle velocity, φ is the transverse force phase and $\dot{\eta}_1$ is the horizontal rigid body motion velocity of the riser.

The total transverse force per unit length can then be obtained by applying Morison's equation to represent the fluid reaction as well as accounting for VIV force from equation 4.21

$$\mathrm{d}F_{\mathrm{transverse}} = \mathrm{d}F_{\mathrm{VIV}} - C_D\,\frac{\rho D}{2}\,|V_r|\,\dot{\eta}_2 - C_M\,\frac{\rho\pi D^2}{4}\ddot{\eta}_2 \tag{4.22}$$

Here, $\dot{\eta}_2$ and $\ddot{\eta}_2$ are the velocity and acceleration of the riser in the transverse direction. $|V_r| = \sqrt{(u + u_c + \dot{\eta}_1)^2 + \dot{\eta}_2{}^2}$ corresponds to the relative velocity between the structure and the fluid.

Chapter 5

Static And Dynamic Response Analysis

The difference between static response analysis and dynamic response analysis is the inclusion of inertial effects, which in static analysis are normally ignored or neglected. In dynamic analysis the time dependence is explicitly considered because the calculation of inertial, and damping if present, forces required derivatives with respect to actual time to be taken. Problems of static nature may also be time dependent, but inertial forces are still normally neglected or ignored.

5.1 Static Response Analysis

Problems of static nature are classified as either linear or non-linear. Linear static analysis deals with static problems in which the response is linear to the input of applied forces, meaning that if the applied forces are doubled, the displacement and internal stresses also double. Static problems outside this domain are classified as non-linear [50]. While in linear analysis the solution always is unique, this many not be the case in non-linear problems. That means the solution achieved may not necessarily be the solution sought [51]. The static analysis part of this thesis involves the establishment of a BOP stack's stiffness characteristics.

The static equilibrium equation is

$$\boldsymbol{K}\boldsymbol{r} = \boldsymbol{R} \tag{5.1}$$

where $\boldsymbol{K}$ is the global stiffness matrix, $\boldsymbol{r}$ is the global displacement vector and $\boldsymbol{R}$ is the total nodal load vector. Traditionally the difficult part is to find the stiffness matrix. Once the stiffness matrix is known, the resulting displacement from corresponding a load

can be obtained. The stiffness matrix depends on the choice of elements the structure is modelled with and computing it can require high processing power. The stiffness matrix is in many cases also dependent on geometry and can change as a result of displacement changes. This makes the problem non-linear

$$\boldsymbol{K}(\boldsymbol{r})\boldsymbol{r} = \boldsymbol{R} \tag{5.2}$$

Regarding non-linear problems, iterative methods and incremental load procedures are implemented to calculate the stiffness matrix, which means calculating the stiffness matrix is an even more extensive job. This is mentioned later in this chapter. Next follows a brief review of elements and how to obtain the global system stiffness matrix.

5.1.1 Elements in Finite Element Analysis

In finite element analysis, structure models are meshed with a finite number of elements. These elements are *one*, *two* or *three* dimensional and characterized by a number of nodes. Nodes have assigned degrees of freedom, meaning they describe what kind of deformation the element can assume. Thus, if a node has no rotational DOF, then the element cannot rotate. The most commonly used elements can be seen in figure 5.1.

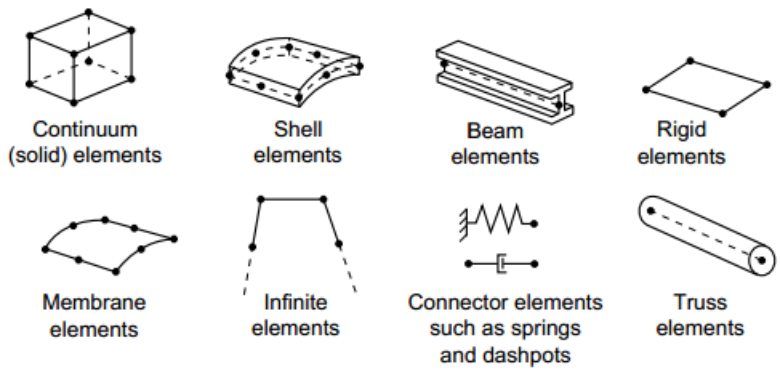

Figure 5.1: Commonly used element families [52]

In FEA, the displacement of elements subjected to loads is assumed. The assumed displacement pattern is described through a set of interpolation polynomials. The accuracy of the solution is dependent on the order of the polynomial. In general, the approximate solution may be represented by an nth order polynomial with $n+1$ nodes.

The displacement pattern in x-direction for the one-dimensional two-noded bar element seen in figure 5.2

$$u(x) = \sum_{i=1}^{2} N_i(x)\, u_i = \boldsymbol{N}\boldsymbol{v} \tag{5.3}$$

where $N_i(x)$ is the interpolation polynomial, sometimes also referred to as a shape function, for node i.

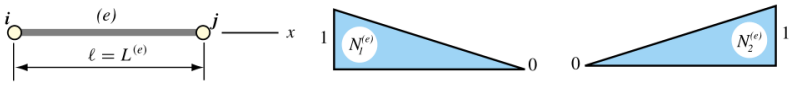

Figure 5.2: Two-noded bar element and displacement patterns [50]

There is one interpolation polynomial for each node in the element. The shape function can describe any translation along the principal axes and any rotation about the principal axes. It is noted that if the node is restrained from certain DOFs, then this is reflected in the shape function. Furthermore, the interpolation polynomial must satisfy the following

$$\begin{aligned} N_i(x = x_i) &= 1 \\ N_i(x = x_j) &= 0 \\ \sum_{i=1}^{n+1} N_i &= 1 \end{aligned} \tag{5.4}$$

The shape functions in figure 5.2 satisfy this requirement. Lagrange polynomials are commonly used as they always satisfy the requirement, although it is not the only way. Hermite polynomials are also used widely for shape functions for beams. From Moan [53], for an nth degree polynomial, the Lagrange polynomials can be established by

$$N_i = \prod_{j}^{n+1} \frac{x - x_j}{x_i - x_j}, \qquad \text{for } j \neq i \tag{5.5}$$

In this thesis, 3-D beam elements with six degrees of freedom in each node and solid elements with 20 nodes and three degrees of freedom in each node will be given attention. These are the elements used in the FEM model of the BOP and this is in accordance with the JIP [3].

3-D beam element

The 3-D beam elements applied in this thesis is often referred to as a space frame elements. It has 6 degrees of freedom in each node, see figure 5.3. The element is

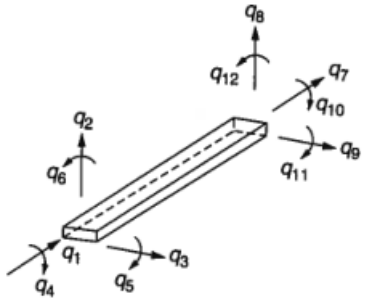

Figure 5.3: 3D beam element [54]

capable of resisting axial forces, bending moments about the two principal axes in the plane of its cross section and lastly twisting moment about its centroidal axis [54]. The element stiffness matrix will have dimension 12×12. This matrix is a result of superposing the sub-stiffness matrices consisting of axial stiffness, torsional stiffness and bending stiffness, respectively. The shape function that describes the translational mode

(a) Translation mode (b) Rotation mode

Figure 5.4: Mode shapes 3-D beam [55]

shape for node 1 seen in figure 5.4a is $N_1 = 1 - 3\frac{x^2}{L^2} + 2\frac{x^3}{L^3}$ and the shape function that describes bending mode for the same node seen in figure 5.4b is $N_2 = x\left(-1 + 2\frac{x}{L} - \frac{x^2}{L^2}\right)$.

Cubic solid element

The cubic solid elements applied in the 3D element model in this thesis are quadrilateral isoparametric serendipity elements, 20-node bricks. The term serendipity refers to the

interpolation. It is based on the corner and midside nodes only [52]. This cubic element has 3 degrees of freedom in each node, translation in x, y and z-direction. For this

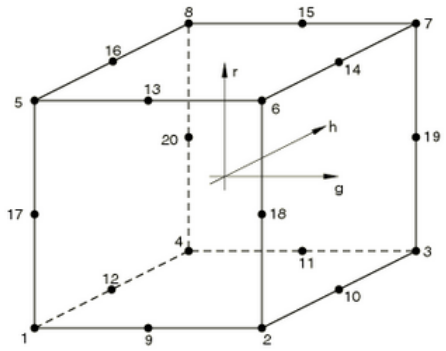

Figure 5.5: 20-node brick element [52]

element there are 20 interpolation polynomials. The interpolation polynomial for corner node 1 on figure 5.5 is $N_1 = -\frac{1}{8}(1-g)(1-h)(1-r)(2+g+h+r)$. This interpolation polynomial can describe any form of translation of node 1 along the three principal axes. Since the nodes in this element have no rotational degrees of freedom, the nodes cannot rotate. The stiffness matrix of this 20-node brick element will have dimension 60×60.

5.1.2 The System Stiffness Matrix

The system stiffness matrix $\boldsymbol{K}$ in equation 5.1 can be established by directly adding the contributions from all the element matrices [53]

$$\boldsymbol{K} = \sum_{j}^{\text{NEL}} \boldsymbol{a}_j^T \, \boldsymbol{k}_j \, \boldsymbol{a}_j \tag{5.6}$$

where $\boldsymbol{a}_j$ is the connectivity matrix (or topology matrix) which holds information about where element j belongs in the global system. Further, the local element stiffness matrix is defined through use of the shape functions discussed above.

$$\boldsymbol{k} = \int_V \boldsymbol{B}^T E \boldsymbol{B} \, \mathrm{d}V \tag{5.7}$$

here $\boldsymbol{B} = \boldsymbol{\nabla} \boldsymbol{N}$ and $\boldsymbol{\nabla}$ is the gradient operator matrix. Once $\boldsymbol{k}$ is known for all elements, the global stiffness can be obtained. E is the Young's modulus.

Non-linear stiffness

In equation 5.1, the stiffness-displacement relationship is linear. However, describing structural behaviour with this relation is not always sufficient. This leads to the term $\boldsymbol{K}(\boldsymbol{r})$ in equation 5.2 which is composed of two terms, a linear term and a non-linear term [51].

$$\boldsymbol{K}(\boldsymbol{r}) = \boldsymbol{K}_0 + \boldsymbol{K}_g(\boldsymbol{r}) \tag{5.8}$$

The non-linear term is a correction due to non-linear geometrical effects. An overview of the different stiffness concepts expressed in a load-displacement environment can be seen in figure 5.6. In the figure, $\boldsymbol{K}_0$ is the linear stiffness, $\boldsymbol{K}_g$ is the geometric correction term, $\boldsymbol{K}_I$ is the tangent stiffness and $\boldsymbol{K}$ is the secant stiffness.

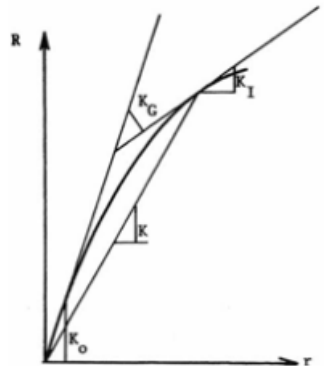

Figure 5.6: Stiffness concepts [51]

There are methods that can be applied to solve the non-linear stiffness problem, for which it is convenient to rewrite equation 5.2 on differential form

$$\boldsymbol{K}(\boldsymbol{r})\boldsymbol{r} = \boldsymbol{R} \longrightarrow \underbrace{\frac{\mathrm{d}}{\mathrm{d}r}\left(\boldsymbol{K}(\boldsymbol{r})\boldsymbol{r}\right)}_{\boldsymbol{K}_I(\boldsymbol{r})} \mathrm{d}r = \mathrm{d}\boldsymbol{R} \tag{5.9}$$

where $\boldsymbol{K}_I(\boldsymbol{r})$ is the tangent stiffness. This formulation makes it possible to solve equation 5.8 by initial value problem or incremental methods, which can be replaced by or combined with iterative methods [51].

Load incremental method

Non-linear structural problems can be solved by the incremental application of the external load, $\boldsymbol{R}$. For each increment of the loading, $\Delta\boldsymbol{R}$, the corresponding displacement increment, $\Delta\boldsymbol{r}$, is calculated by using the tangent stiffness, $\boldsymbol{K}_I(\boldsymbol{r})$, known from the previous increment. The tangent stiffness is calculated based on the known displacement and stress condition before a new load increment is applied. The total displacement is obtained by adding all the displacement increments thus far [51]. At load increment number $m+1$, this gives the following relations

$$\Delta\boldsymbol{R}_{m+1} = \boldsymbol{R}_{m+1} - \boldsymbol{R}_m \tag{5.10}$$

$$\Delta\boldsymbol{r}_{m+1} = \boldsymbol{K}_I^{-1}(\boldsymbol{r}_m)\,\Delta\boldsymbol{R}_{m+1} \tag{5.11}$$

$$\boldsymbol{r}_{m+1} = \boldsymbol{r}_m + \Delta\boldsymbol{r}_{m+1} \tag{5.12}$$

This method is called the Euler-Cauchy method. However, this method does not achieve total equilibrium. The residual forces that remain in each increment, $\boldsymbol{R} - \boldsymbol{R}_{\text{int}}$, can be accounted for when calculating the next corresponding displacement increment (equation 5.11), and thus improving the solution. This gives

$$\Delta\boldsymbol{R}_{m+1} = \boldsymbol{R}_{m+1} - \boldsymbol{R}_m \tag{5.13}$$

$$\boldsymbol{R}_{\text{eq}} = \boldsymbol{R}_m - \boldsymbol{R}_{\text{int}}(\boldsymbol{r}_m), \qquad \longleftarrow \text{equilibrium correction} \tag{5.14}$$

$$\Delta\boldsymbol{r}_{m+1} = \boldsymbol{K}_I^{-1}(\boldsymbol{r}_m)\,\Delta\boldsymbol{R}_{m+1} - \boldsymbol{K}_I^{-1}(\boldsymbol{r}_m)\,(\boldsymbol{R}_{\text{int}}(\boldsymbol{r}_m) - \boldsymbol{R}_m) \tag{5.15}$$

$$\boldsymbol{r}_{m+1} = \boldsymbol{r}_m + \Delta\boldsymbol{r}_{m+1} \tag{5.16}$$

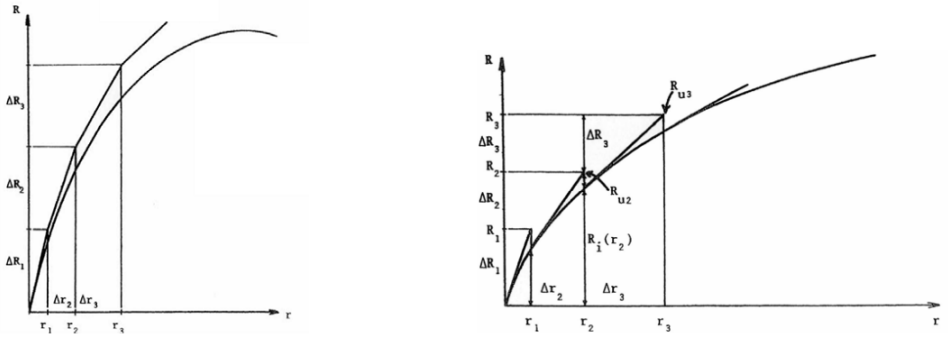

(a) Euler-Cauchy (b) Modified Euler-Cauchy

Figure 5.7: Euler-Cauchy load incremental method [51]

The equilibrium correction is of great significance, and the impact is illustrated by before and after illustrations, see figure 5.7. The smooth line is the true solution of the stiffness.

Iterative method

Non-linear structural problems can also be solved by iteration. One of the most frequently used method is the Newton-Raphson method [51]. An iterative method solves $\Delta \boldsymbol{r}_{m+1} = \boldsymbol{K}_I^{-1}(\boldsymbol{r}_m)\,[\boldsymbol{R} - \boldsymbol{R}_{\text{int}}]$ in each iterative step, and requires that $\boldsymbol{K}_I$ is updated in each iterative step as well. This is time consuming and it is recommended that the stiffness is updated less frequently, but it is not ideal to not update it as well. The difference in one update of $\boldsymbol{K}_I$ per iteration compared to no update of $\boldsymbol{K}_I$ is seen in figure 5.8. Iterative and incremental methods are also often combined. The external load

(a) No update of $\boldsymbol{K}_I$ (b) One update of $\boldsymbol{K}_I$

Figure 5.8: Newton-Raphson iteraton [51]

is then applied incrementally and in each load increment equilibrium is achieved by iteration [51]. There are also more advanced solutions procedures available, such as arc-length methods. These are however methods that are applied when it is of interest to investigate what happens beyond limit points, such as material yield limit. This is, however, not of interest in this thesis.

5.1.3 Abaqus - Finite Element Software

Abaqus/CAE is a FE software for finite element analysis and computer-aided engineering. It was initially designed to address non-linear physical behaviour. Abaqus contains a library consisting of many element types, including solid elements and beam elements for three-dimensional applications used for this thesis. A common Abaqus procedure involves a pre-processing sequence, a simulation sequence, and a post-processing sequence.

Pre-processing

In this sequence, the modeling takes place. Once the model is built, it needs to be assigned material properties. What type of elements to use and how to meshing is also done here. Appropriate boundary conditions to the model is determined, and loads acting on it.Instead of modelling, models can be imported from input files. Abaqus communicates well with other software, and can read a range of input files. Often, in imported model files, material properties and elements are prescribed. Frequently, modelling is done utilizing different symmetry properties of the object, meaning loading and boundary conditions must then be applied with great caution. These must be applied in accordance with the symmetry, axi-symmetry or anti symmetry properties of the model. If the object is modelled as a whole, less caution must be taken, but longer CPU time should be expected.

Simulation

In this sequence, it is common to choose what sort of output is desired from the simulation. Stresses, strains, displacements, velocities, accelerations, forces to name a few. How many time steps to be stored in the solution is chosen as well. For computing intensive tasks, use of parallel computing can be advantageous.

Post-processing

Once simulation has executed, the post-processing starts. An important note concerning the post-processing sequence is that the analyst is always responsible for the FE results. In this lies the notion that experience and knowledge is required of the analyst. In the post-processing sequence, all the output that was chosen in the simulation sequence can be reviewed.

5.1.4 The Effective Tension Concept

Another important static topic is the concept of effective tension. In the literature the concept of effective tension is referred to when explaining the behaviour of slender marine structures [56]. For a marine riser, the inside may be filled with drilling mud, and the content need to be kept in equilibrium by stresses in exactly the same way

as the riser steel wall, which means the concept of effective tension is nothing more than the cross-section resultant, resulting from integrating the entire cross section of the riser [56], see figure 5.9. From this we can derive a total cross section axial force as

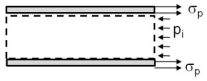

Figure 5.9: Effective tension - Cross section [56]

$$T_{\text{eff}} = \int_{A_p} \sigma_p \, \mathrm{d}A_p - \int_{A_i} \rho_i \, \mathrm{d}A_i \tag{5.17}$$

$$= T_p - \rho_i A_i \tag{5.18}$$

and to account for the lack of external pressure stresses at all cross sections, there must also exist a force $\rho_e A_e$ such that

$$T_{\text{eff}} = \int_{A_p} \sigma_p \, \mathrm{d}A_p - \int_{A_i} \rho_i \, \mathrm{d}A_i + \int_{A_e} \rho_e \, \mathrm{d}A_e \tag{5.19}$$

$$= T_p - \rho_i Ai + \rho_e A_e \tag{5.20}$$

Furthermore, the effective tension, at any point along the riser, can be obtained most simply by considering the equilibrium of the segment between the point and the riser top end taking into account the riser top tension and the segments apparent weight [57]. The effective tension concept for the whole riser is illustrated in figure 5.10.

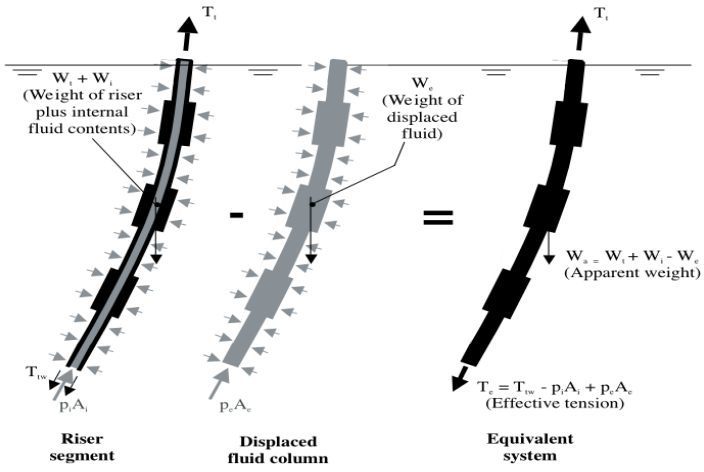

Figure 5.10: Effective tension illustration [57]

5.2 Dynamic Response Analysis

In wellhead fatigue analysis there are two analysis choices that must be made. There is the choice between a coupled and a de-coupled analysis model. The other choice is the solution approach which can be done in time-domain or in frequency-domain [9].

In this context, *coupled* analysis entails a global model of the entire drilling system. This implies that displacements, forces and moments on the entire system can be considered in the same environment in one analysis [58]. Alternatively, *decoupled* analysis is considered a two-stage procedure where two separate models are used to predict the behaviour of the entire drilling system. The first model, a global model, commonly represents the drilling system from the upper flex joint to the top of the BOP stack. The second model, a local model, represents the remaining part of the drilling system, i.e. from the top of the BOP stack to the bottom of the wellhead system [58].

Time-domain simulation yields the solution directly as a function of time. This is a natural choice of solution approach in the case of deterministic loading with the load given as a function of time [59]. In frequency-domain simulations an arbitrary excitation can be written as an infinite sum of harmonic components. This can be expressed mathematically by Fourier transformation. The sum of all these components yields the excitation function, which expresses the excitation in the frequency-domain. The same process can be applied to the response. Solution in the frequency-domain expresses directly the sensitivity of a structure to the load frequency [59], which can in some cases be of high interest, especially for structures with a frequency dependent mass, damping or stiffness matrix. However, choosing frequency domain solution will require linearisation of non-linear relationships, and to avoid such linearisation, time-domain should be the chosen approach for wellhead fatigue load estimation [9].

5.2.1 Riflex

This section describes the computer program Riflex; a FE software distributed by MARINTEK which performs static and dynamic analysis of slender marine structures. In recent years MARINTEK has developed the software tool SIMA. SIMA incorporates Riflex and other similar software in a computer package that address analysis of structures in marine environments. Though Riflex is applied using SIMA in this thesis, this section will address Riflex as it is described in the Riflex user manual [60] and theory manual [61].

Riflex is commonly applied when performing dynamic analysis on riser systems. Since a riser is relative small in diameter it may be defined as a slender structure. Other structures like pipelines and fish farms follows the same definition and is thus compatible with Riflex. In general slender structures is characterized by [61]:

- ◇ Small bending stiffness
- ◇ Large deflection
- ◇ Large upper end motion excitation
- ◇ Non-linear cross section properties
- ◇ Complex cross section structure

For slender structures in a marine environment the hydrodynamical loads acting on a body may be calculated by Morison's equation (equation 4.15) which is described in section 4.2.1. On the other hand, the software is not able to compute the dynamic behaviour of large structures like ships and platforms. This implies that the floater's response behaviour must be pre-calculated. Commonly the floater's response behaviour is determined from model tests, or calculated with dedicated software. Further, the response behaviour of the floater may be presented as a response amplitude operator. The RAO can be considered as a hydrodynamical transfer function which can determine the relationship between wave loads and the floater's response:

$$x(\omega) = H(\omega)\,\zeta_0(\omega) \tag{5.21}$$

where x, H and ζ_0 represents response amplitude, hydrodynamical transfer function and wave amplitude, as functions of wave frequency, respectively.

Riflex structure

Riflex is divided into five modules. Global models are either made in the input module, INPMOD, or it can be imported from an external file. The main environmental data are also defined in INPMOD. The next step is to perform a static analysis of the system in the STATMOD module. The results are used to define the initial configuration for the dynamic analysis. The third step is to perform the time domain dynamical analysis in the DYNMOD module. Input to the DYNMOD module comprises of results from the STATMOD module, environmental data and data that defines forced vessel displacements in the analysis. From DYNMOD it is possible to obtain the dynamic

response of the system. Lastly, the OUTMOD module, a post-processor, generates a result file from the other modules.

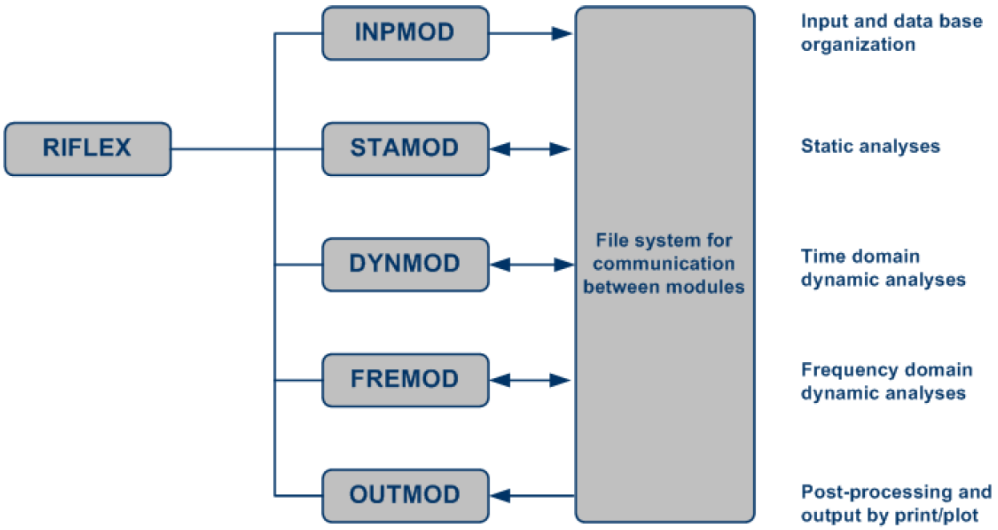

Figure 5.11: Riflex modulus [60]

The modelling technique in Rilfex is shown in figure 5.12. It consists of defining supernodes, lines, segments and elements. Supernodes may be classified as free, fixed

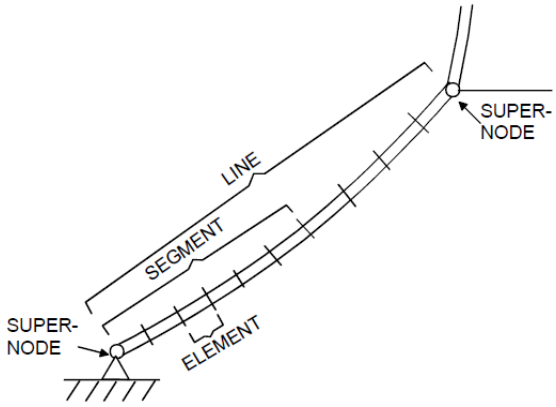

Figure 5.12: Riflex modelling [60]

or prescribed. Lines are defined as linear structural elements between two supernodes. Different segments can exist within a line. A segment is defined as a part of a line with uniform cross section properties and element lengths.

Analysis options in Riflex

There are four different types of analyses which are available in Riflex [60], though not all of them are implemented in Sima at current time.

- ◇ Static analyses
- ◇ Static parameter analyses
- ◇ Dynamic time domain analysis
- ◇ Frequency domain analysis

In this thesis, the dynamic time domain analysis is of interest and will be further assessed. It is possible to perform both a complete non-linear time domain analysis and a linearised time domain analysis. By application of the linearised approach, CPU time is saved, but the results may be inaccurate if the system contains significant non-linearities. Regardless of approach, time domain analyses are carried out using step-by-step numerical integration.

5.2.2 Solving the Dynamic Equation of Motion

The dynamic equation of motion, equation 5.22, is a second order differential equation which, in this context, cannot be solved analytically. This means that the solution must be obtained by numerical approximation. Such numerical approximation is done by the application of numerical integration methods. One of the main concepts behind numerical integration is to divide the time series into time steps or time intervals. These methods relay on solving the dynamic equation of motion at each time step [59].

$$\boldsymbol{M}\ddot{\boldsymbol{u}}(t) + \boldsymbol{C}\dot{\boldsymbol{u}}(t) + \boldsymbol{K}\boldsymbol{u}(t) = \boldsymbol{Q}(t) \tag{5.22}$$

Here $\boldsymbol{M}$ is the system mass matrix, $\boldsymbol{C}$ is the system damping matrix and $\boldsymbol{K}$ is the system stiffness matrix, $\ddot{\boldsymbol{u}}$, $\dot{\boldsymbol{u}}$ and $\boldsymbol{u}$ are acceleration vector, velocity vector and displacement vector, respectively. $\boldsymbol{Q}$ is the load vector.

Initially, the start values for $\ddot{\boldsymbol{u}}$, $\dot{\boldsymbol{u}}$ and $\boldsymbol{u}$ at $t = t_0$ are known. Then, at each time step, new values for $\ddot{\boldsymbol{u}}$, $\dot{\boldsymbol{u}}$ and $\boldsymbol{u}$ are calculated using the result from the previous time step. The solution at the end of each interval is determined by assuming a certain variation in the acceleration over the time interval. Large time steps may thus lead to inaccurate

assumptions. The velocity and displacement are found at each time step by integrating the assumed acceleration once and twice, respectively. This implies that the calculated displacements and velocities are dependent on how the accelerations are assumed to vary in the interval. This procedure is exemplified for one DOF for the interval between time step k and $k+1$.

$$\dot{u}_{k+1} = \dot{u}_k + \int_0^h \ddot{u}(t)\,\mathrm{d}t \tag{5.23}$$

$$u_{k+1} = u_k + \int_0^h \dot{u}(t)\,\mathrm{d}t \tag{5.24}$$

where h is the length of the interval. The velocity and displacement that are found from equation 5.23 and 5.24 are inserted into equation 5.22, which subsequently is solved with respect to $\ddot{u}(t)$ as shown in equation 5.25.

$$\ddot{u}(t) = \frac{1}{m}\left(Q(t) - c\dot{u}(t) - ku(t)\right) \tag{5.25}$$

It follows that if the magnitude of $\ddot{u}(t)$ is satisfactorily equal to the assumed acceleration, then the assumption has proven to be correct. Otherwise, a new assumption of the acceleration is made until satisfactorily equilibrium is obtained between $\ddot{u}(t)$ and the assumed acceleration. Several methods on how to assume the variation in acceleration over the time interval exist. Two methods will be described further; one by assuming constant average acceleration over the time interval and one by assuming linearly varying acceleration over the time interval.

Constant average acceleration

The constant average acceleration method is also known as the trapezoidal rule. Like the name of the method implies, the acceleration is constant over the interval. The magnitude of the acceleration is equal to the average of the known acceleration at the start of the interval and the assumed acceleration at the end of the interval.

$$\ddot{u}(t) = \frac{1}{2}(\ddot{u}_k + \ddot{u}_{k+1}) \tag{5.26}$$

Integrating equation 5.26 leads to linear velocity and quadratic displacement, see figure 5.13b.

Linear acceleration

The linear acceleration method, comprises assuming linearly varying acceleration over the interval. The acceleration over the interval can be expressed accordingly

$$\ddot{u}(t) = \ddot{u}_k + \left(\frac{\ddot{u}_{k+1} - \ddot{u}_k}{h}\right) t \tag{5.27}$$

Integrating equation 5.27 leads to quadratic velocity and cubic displacement, see figure 5.13a. This is, in general, a more accurate method than constant average acceleration. However, the method is only conditionally stable in contrast to the constant average acceleration method which is unconditionally stable.

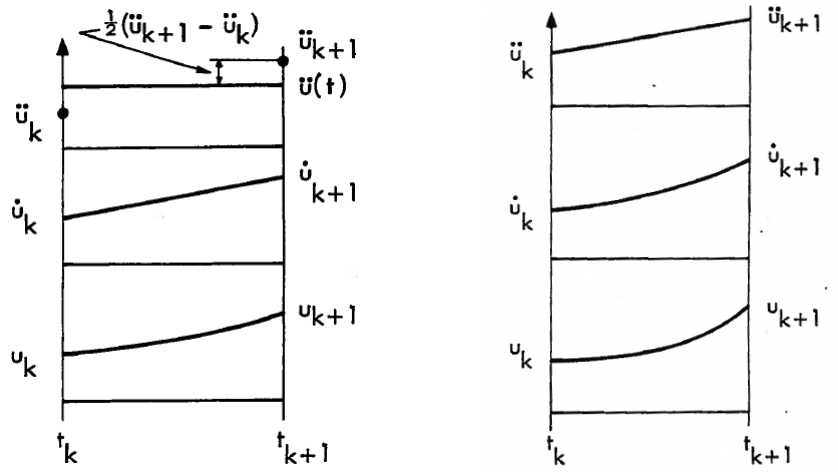

(a) Constant average acceleration (b) Linearly varying acceleration

Figure 5.13: Assumed variation in the acceleration over a time interval [59]

Newmark-β

Riflex applies the Newmark-β familiy for response analysis of slender structures. Hence only these methods will be described. The methods in the Newmark-β family are separated by different values for β. Two of these methods are linear and constant average acceleration, which are described above. These methods corresponds to values for $\beta = \frac{1}{6}$ and $\beta = \frac{1}{4}$, respectively. Values for γ determine if the method introduces artificial damping or not. In most cases artificial damping is not desirable and $\gamma = \frac{1}{2}$ is applied. Further, the equations which give the relationship between displacement, u,

velocity, $\dot{u}$ and acceleration, $\ddot{u}$ at the time t and $t + h$:

$$\dot{u}_{t+h} = \dot{u}_t + (1 - \gamma)h\ddot{u}_t + \gamma h\ddot{u}_{t+h} \tag{5.28}$$

$$u_{t+h} = u_t + h\dot{u}_t + \left(\frac{1}{2} - \beta\right) h^2\ddot{u}_t + \beta h^2\ddot{u}_{t+h} \tag{5.29}$$

where $\tau = \theta\Delta t \geq 1.0$. Equation 5.28 and 5.29 are known as Newmarks general integration equations and applies for all methods [59].

Stability

As mentioned above there is a difference between the methods in terms of stability. A method is considered to be stable if the amplitude of an object in free vibration does not change when the number of time steps are changed, e.g. a pendulum oscillating in vacuum; there is no damping, the amplitude should remain constant. Hence it is preferable to perform a sensitivity study when applying methods that are conditionally stable.

Linearised numerical integration

Linearised numerical integration is based on a linearisation of the dynamic equation of motion at static equilibrium position [61]. System matrices are computed prior to the integration and remains constant throughout the procedure. This represents lower CPU time in comparison to updating the matrices for each time step.

Non-linear numerical integration

Non-linear numerical integration is a beneficial method if the system under consideration is expected to suffer considerable non-linearities during the analysis. In general, the non-linearities that may occur in structures may be summarized as [59]:

- ◇ Non-linear material properties
- ◇ Geometrical non-linearities
- ◇ Non-linear effects caused by interaction between the structure and its environment

System matrices must be updated for each step to account for system non-linearities. The recalculation of the matrices may be done by iterations using Newton-Raphson methods or by incremental methods which are described in section 5.1.2. Riflex applies the Newton-Raphson method, which recalculates the incremental stiffness matrix $\boldsymbol{K}_{Ik}$ and damping matrix $\boldsymbol{C}_{Ik}$ for each iteration step within each time step.

Damping

Damping is a phenomena that causes loss of dynamic energy for an oscillating object. Many types of damping exist. The most relevant types for drilling systems may be summarized as structural damping, hydrodynamical damping and soil damping. A challenge is represented in how the damping should be described when dynamic analyses are carried out.

Soil damping is relevant in relation to the dynamic interaction between the wellhead and the soil. The characteristics of the damping is highly dependent on the properties of the soil, which again is dependent on the location of the well. Soil damping may be divided into two different groups; damping which is caused by propagation of wave energy away from the structure (wellhead in this case) and damping caused by cyclic shear deformations in the soil [59]. For application in Riflex, soil damping may be implemented in a spring together with the corresponding soil stiffness.

Hydrodynamical damping may be divided into two categories; viscous damping and potential damping. Viscous damping is proportional to the water particle velocity squared and may, for slender structures, be calculated by Morion's formula. Potential damping is related to the structure's generation of waves and is proportional to the particle velocity. For dynamic analysis using software like Riflex the dynamic response behaviour of the MODU is, as mentioned in section 5.2.1, implemented as an RAO. This implies that hydrodynamical damping is only calculated for the riser. The geometrical properties of a riser implies that viscous effects are highly dominating compared to potential damping.

Structural damping is due to friction and gliding in the material and connections in the structure [59]. This kind of damping is usually hard to determine directly. Instead the structural damping may be determined by a relation between damping, mass and

stiffness.

$$\boldsymbol{C} = \alpha_1 \boldsymbol{M} + \alpha_2 \boldsymbol{K} \tag{5.30}$$

This is known as proportional damping or Rayleigh damping and is applied by Riflex when performing time domain analyses.

Chapter 6

Fatigue Assessment of Subsea Wellheads

Currently, no applicable codes for determination of fatigue in subsea wellheads exist. It is therefore reasonable to assume that companies are using different techniques and methods when performing wellhead fatigue analyses. However, a joint effort between companies is in progress to establish a leading method. This joint effort is the ongoing JIP on structural well integrity as described in section 1.2.1.

In this chapter there will be given a summary of techniques and methods for performing fatigue assessments of subsea wellheads. The main contribution is the paper "Wellhead Fatigue Analysis Method" by DNV [3] which is a result from the JIP. The methodology presented below will have a foundation in an interpretation of this paper, but with contributions from other articles written on the subject. In the literature it is mentioned that the stiffness of the BOP stack should be appropriate. Nevertheless, no descriptions of methods for implementation of the BOP stack stiffness in global analyses are given. The stiffness of the BOP is therefore not a part of the current methodology. Common practice in relation to dynamic analyses of drilling systems is to model the BOP stack with infinitely high stiffness, as mentioned in scope of this thesis. Inclusion of realistic BOP stack stiffness will be presented in the modelling and analysis chapter, chapter 7.

Proposed methodologies for performing of subsea wellheads primarily comprise a local and a global response analysis. When combining these analyses, it is possible to gather the necessary information to carry out a fatigue damage assessment. The goal is to obtain an estimated fatigue life of the wellhead. An overview of the different steps in the local and global analyses is given in figure 6.1. Regarding the local analysis, the purpose is two sided. The first purpose is to develop load-to-stress curves for relevant hot spots in the wellhead system. The second purpose is to establish wellhead boundary conditions for the global response analysis. The purpose of the global response analysis is to develop moment-time series. The moment-time series from the global response

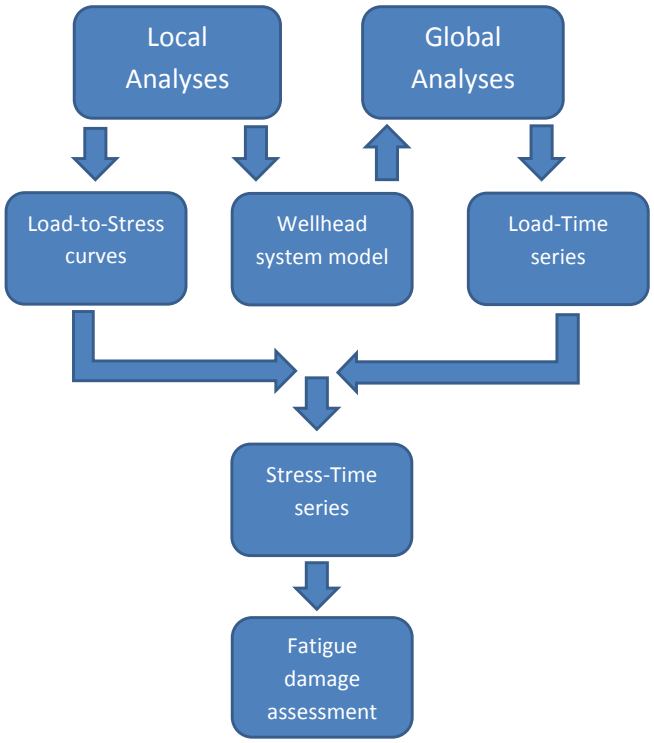

Figure 6.1: Analysis Overview

analysis is mapped with the load-to-stress curves from the local analysis. The result is stress-time series. Further, the stress-time series act as input to the fatigue damage assessment. The result can comprise of a fatigue life estimate for the relevant hot spot in the wellhead.

6.1 Local Response Analysis

The purpose of the local analysis is two sided. The first purpose is to develop the load-to-stress curves for relevant hot spots in the wellhead system. The second purpose is to establish wellhead boundary conditions for the global response analysis. The modelling and analysis should be carried out in a FEM software. Regarding the extent of the model, it is only necessary to model the drilling system from the wellhead datum and below. The wellhead should be modelled in its entirety including conductor, wellhead housing, cement and casings. If a fatigue assessment of connectors, BOP or XT is of interest, this may be carried out by executing a detailed analysis of these components. This is though not of interest in this thesis.

6.1.1 Wellhead Modelling

A correct representation of the wellhead system and its boundary conditions is essential to obtain realistic results. The complexity of the system represents great challenges related to modelling and many different inputs are needed. These inputs may be summarised as:

- ◇ Interacting loads
- ◇ Soil properties
- ◇ Wellhead geometry
- ◇ Material properties
- ◇ Friction forces and contact definitions

Interacting Loads

When modelling the wellhead system it is necessary to limit the vertical extent of the model. DNV [3] proposes to model 50 meter below mudline. This implies that the weight of the casing that is not included in the model must be applied as a vertical force. A representation of the contact forces between the pipes in the wellhead is necessary to allow the pipes to slide relative to each other.

Static loads which originates from components which are not included in the model must be applied as a vertical force at the wellhead datum. Examples of such components are BOP stack and riser.

Soil Stiffness

The soil stiffness is found by the use of stress-displacement(P-y) curves. The soil is modelled as non-linear springs. The curves are given as a function of stress, which makes it necessary to convert the P-y data into a force-displacement relation. This is done by multiplying the stress with the area of the pipe which is in contact with the given layer of soil. The spring equation is recognized as:

$$P = ky \tag{6.1}$$

where P, k and y are force, spring stiffness and displacement respectively. It is noted that P-y curves may be expressed in several variations, by either force, force per distance, pressure or stress to name a few.

Template Stiffness

The template may be modelled in its full geometry or as springs, dependent on available data. Modelling of the template in its entirety will result in additional modelling time and CPU time. If the template is modelled as a spring, it is important to acknowledge the symmetric properties of the template. For a regular 4- or 6-well template with a central positioned manifold, the stiffness will not be axi-symmetric.

6.1.2 Stress Concentration Factors

Stress concentrations occur in geometrical irregularities like welds and cut-outs. In DNV DNV RP-C203 [31], an SCF may be defined as *the ratio of hotspot stress range over nominal stress range*. The expression for SCF is:

$$\text{SCF} = \frac{\Delta\sigma_{\text{hotspot}}}{\Delta\sigma_{\text{nominal}}} \tag{6.2}$$

where nominal stress is the stress calculated from the net cross section of the component. SCFs may be obtained in two ways. Either by conducting a separate FEM analysis of the hot spot or by application of standardised values from codes. SCFs should, if applicable, be included when calculating hot spots stress.

6.1.3 Establishment of Wellhead Boundary Conditions

The wellhead stiffness is an essential parameter in a wellhead fatigue assessment. As explained in section 6.1.1, the soil interacting with the wellhead will affect the flexibility of the system. A wellhead model which is implemented in the global analysis is shown in figure 6.2. The purpose of the model is to include the stiffness from the soil and guidebase/template as well as the wellhead stiffness itself in a freely supported beam with a lateral spring attached. The stiffness characteristics of the wellhead model can be obtained by applying load to the wellhead datum.

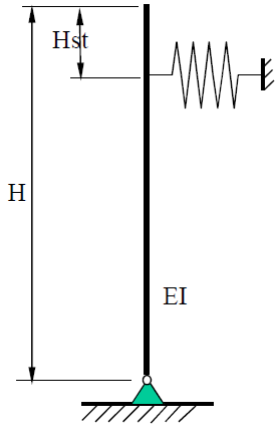

Figure 6.2: Wellhead beam model [3]

Hørte *et al.* [3] propose two load cases to be applied to the wellhead datum. One where pure moment is applied and one where pure shear force is applied. The next step is to determine displacements and rotations which correspond to the loads. The result comprises of four different curves, where displacements and rotations are plotted as functions of moment and shear force. From this it is possible to obtain the bending stiffness, EI, of the beam as well as the lateral spring stiffness. The system shown in figure 6.2 is subsequently implemented in the global model as a representation of the wellhead system.

6.1.4 Load-to-Stress Curves

Load-to-stress curves are also obtained by loading the wellhead datum. The loading is divided into two steps. The first step is to apply the static loads which originates from components, which are not included in the model, as a vertical force. Examples of such components are BOP stack and riser. . The second step is to apply cyclic, incremental bending moment at the wellhead datum. The bending moment is a result of loads that act in the flex joint. These loads are transferred from the riser and are combinations of shear force and bending moment. The BOP stack acts as a moment arm for the shear force which results in bending moment at the wellhead datum. When considering forces which act in the wellhead datum, the bending moment is the only load which varies in time, i.e. it is sufficient that the analysis are carried out with bending moments of all reasonable magnitudes.

6.2 Global Response Analysis

Global response analyses requires a model of the entire drilling system. Accurate representations of different components and physical features are essential to gain accurate results. The following section will address methods for modelling drilling systems for application in global response analyses. Examples of applicable software for modelling and global analyses are Orcaflex[1] and Riflex[2].

Through the life of a subsea well, the wellhead experiences fatigue loads from different operations. The operations are commonly known as drilling, workover and completion. The operations comprises of different phases with certain configurations, e.g the drilling operation comprises of phases with different mud density and casing installed. This implies that separate global models must be built to accurately represent each operation. The operation under consideration in this thesis is a drilling operation. The drilling system configuration will hence be considered further. The main inputs needed for the analyses may be summarized as:

- ◇ Response transfer function for MODU
- ◇ Riser data
- ◇ Tension system data
- ◇ BOP stack data
- ◇ Flex joint stiffness
- ◇ Wellhead data from local analysis
- ◇ Environmental parameters

The tensioner data may be implemented in the global model in different ways dependent on desired accuracy. The simplest way is to insert a constant top tension at the top of the riser. A more realistic way is to assign a spring with linear or non-linear stiffness. Modern tension systems are, as described is section, not able to keep a constant tension in the riser. Thus the spring should simulate the deviation from the constant tension.

In software tools like Riflex, all structural components are modelled as beam or bar elements. As for the BOP stack, common practice in relation to dynamic analyses of drilling systems is to model the BOP stack with infinitely high stiffness. The implementation of the improved BOP stack stiffness will be evaluated in chapter 7.

[1]Orcaflex: *A software package for the analysis of offshore marine systems*
[2]Riflex: *A software program for analysis of slender marine structures*

The wellhead may, as described in section 6.1.1, be implemented with as a beam and spring model.

6.2.1 Current Modelling

A general assumption is that current will yield non-conservatism in regards to wellhead fatigue. This is due to the increased hydrodynamical damping that acts on the system. A consequence of this is smaller riser displacement amplitudes. Smaller displacements in the riser implies smaller loading ranges at the lower flex joint. This induces smaller moment ranges at the wellhead datum and thus smaller stress ranges in hot spots. Nevertheless, if an investigation of a drilling system loaded with current is desired, DNV [3] recommends a current profile that will be exceeded 90 % of the time to yield conservatism. If a consideration of VIV should be included in the analysis, more accurate current data must be obtained. Three different ways to obtain these data were presented by Williams and Greene [10]; by non exceedance data, by EOF current data and by measured current profiles. For VIV calculation, dedicated software tools must be applied.

Non exceedance data

Current data from the drilling site itself is rarely known. This means that data from a nearby location must be applied in the model when conducting analysis. This is done by extrapolating the data from the nearby location. These data are usually provided in terms of return periods and values of non-exceedance, i.e. the 90 % exceedance value recommended in JIP [3] corresponds to 10 % non-exceedance value. This method represents a simplified current profile and is therefore not a good input for a VIV analysis.

EOF current data

An EOF[3] is used to simplify current data and transfer them into series of energetic modes. The advantage with this method, is that detailed current data can be applied to dynamic analyses without imposing additional significant CPU time. Forristall and

[3]EOF: Empirical Orthogonal Functions

Cooper [62] conclude that EOF combined with the inverse FORM[4] is ideal for the use in fatigue analyses of risers. The joint probability that results from combining energetic mode amplitudes may be presented by scatter plots in the same way as wave heights and periods, i.e the stress/force histograms from a dynamic response analysis may be weighted on the basis of the probability of occurrence for both waves and current.

Measured Current profiles

The most accurate current data is gained through measurements at the actual drilling site. Such measurements are commonly taken at different water depths with intervals between 30 minutes and 1 hour and a total period of at least one year [10]. The extent of the measurements implies relative large amounts of current data which will impose some extra CPU time in an analysis.

6.2.2 Selection of Sea States

The generation of waves in global analyses is based on input in terms of H_s and T_p which may be sampled from a wave scatter diagram. Typical scatter diagrams consist of a joint distribution between significant wave height, H_s, and the spectral peak wave period, T_p. For historical operations, scatter diagrams which are generated for each operational phase using measured wave data, is the most ideal input. For planned operations, a scatter diagram shall be selected dependent of the length of the operation and time of year [3]. In addition, the scatter diagram should be chosen with regards to operation site.

6.2.3 Results from Global Analysis

The main results from the global analyses are moment-time series from the wellhead datum. The moment-time series, together the with load-to-stress curves from the local response analysis, make out the foundation for the fatigue damage assessment.

[4]FORM: First Order Reliability Method

6.3 Fatigue Damage Assessment

The next step is to carry out a fatigue damage assessment in order to estimate the fatigue life of given hotspots. Initially, the load-to-time series are mapped with the load-to-stress curves. The load-to-time series are obtained from the global response analyses and the load-to-stress curves are obtained from the local response analyses. Stress concentration factors should be included if applicable before proceeding. Further a cycle counting procedure is carried out. The rainflow counting algorithm is an example of such a procedure. The counting allows the stress-time series to be divided into blocks which represent given stress ranges. According to the JIP [3], the stress-time series should be divided into a minimum number of 100 blocks. Each stress range will have a corresponding number of cycles. The fatigue damage may then be calculated by Palmgren-Miner summation.

$$D = \sum_{i=1}^{k} \frac{n_i}{N_i} \tag{6.3}$$

The summation is done for k stress ranges and n_i represents the number of cycles accumulated at the given stress level and N_i is the average number of cycles to failure at the same stress level. DNV [31] presents a modified version of the Palmgren-Miner summation which incorporates SN parameters:

$$D = \frac{1}{\bar{a}} \sum_{i=1}^{k} n_i (\Delta\sigma_i)^m \tag{6.4}$$

where

D : Fatigue damage in phase p of a drilling/workover/completion operation

n_i : Number of cycles in stress block i

N_i : Number of cycles to failure

m : Slope of SN curve

$\Delta\sigma_i$: Stress range at stress block i

$\bar{a}$: Empirical constant

k : Number of stress blocks

A bi-linear SN curve should be applied to account for variable amplitude loading. The fatigue damage must be calculated separately for each slope.

$$D_{\text{phase}} = D_{\text{slope 1}} + D_{\text{slope 2}} \tag{6.5}$$

The resulting fatigue damage, D_{phase}, now represents the fatigue damage of a given phase of the operation. Summing up the damage from each phase will give the total damage subjected to the wellhead:

$$D_{\text{total}} = \sum_{\text{phase}=1}^{k} D_{\text{phase}} \tag{6.6}$$

where k represents the number of phases in the operation. As described in section 3.5.3 the structure is expected to collapse when the Palmgren-Miner sum reaches unity.

A representation of remaining fatigue capacity in percent could be presented as shown in figure 6.3 if the calculated fatigue damage is lined up chronological with respect to each phase,

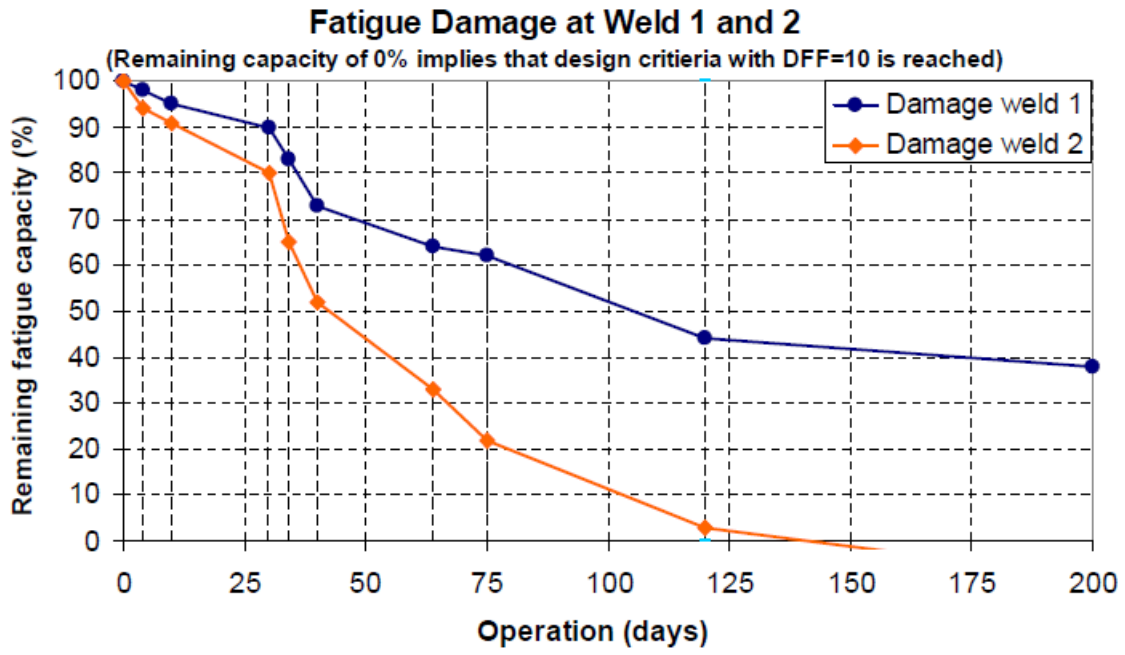

Figure 6.3: Remaining fatigue capacity [3]

The drilling system configuration may have significant impact on the estimated fatigue damage relative to other configurations. The changes in configuration is represented by

changes in slope as seen in figure 6.3. The changes in slope have a significant effect on the estimated fatigue life and thus underlines the importance of analysing all planned operations and phases until estimated collapse of the wellhead is reached.

Chapter 7

Modelling & Analysis

A wellhead fatigue assessment of an example drilling system has been carried out as part of the thesis. This chapter addresses the local modelling and analysis of a BOP stack. Further the global modelling and analysis of a drilling system is described. The next chapter addresses the results of this wellhead fatigue assessment.

In regards to global modelling of drilling systems, the BOP stack is commonly assumed to have infinitely high stiffness. The main objective in the thesis is to investigate if this is a good assumption. The investigation is conducted by implementing more realistic BOP stack stiffness properties in the global model. The more realistic BOP stack model will further be referred to as an elastic BOP stack model. The effects of BOP stack modelling are evaluated with regards to estimated fatigue damage in the wellhead. This approach involves that two fatigue assessments must be carried out, one for each representation of the BOP stack. In order to apply an elastic BOP stack in a global model, its stiffness properties must first be obtained. This was done by investigation of a detailed 3D element model of a BOP stack in Abaqus. A detailed description of this investigation is given in section 7.1.

When the elastic BOP stack model is implemented in the global model of the drilling system, global response analyses are run. The global response analyses are run for a global model that incorporates an infinitely stiff BOP stack model and for a global model that incorporates the elastic BOP stack model. The global response analyses calculates the moment as function of time at the wellhead datum. These moment-time series are imported to Matlab together with provided load-to-stress curves. The load-to-stress curves describes the relationship between moment at the wellhead datum and stress that occur in a hot spot in the wellhead. The load-to-stress curves are further mapped with the moment-time series, the result is stress-time series. The stress-time series are counted as stress cycles. Finally, the estimated fatigue damage in the hot spot in the wellhead is calculated using Palmgren-Miner summation.

The modelling and analysis is a process of high complexity. To maintain overview of the process, it was divided into many small and structured steps. The process can be summarized with the steps illustrated in figure 7.1.

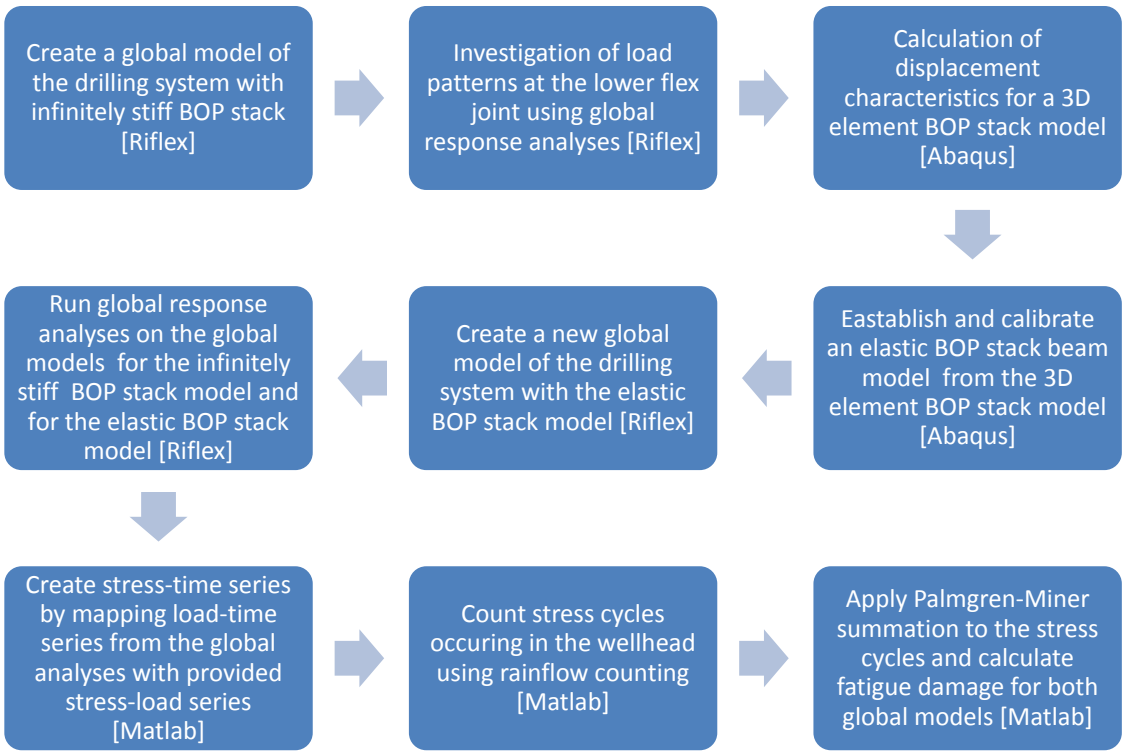

Figure 7.1: Flow chart of modelling and analysis

It appears from the flowchart in figure 7.1 that different models of the BOP stack is applied in the studies which are carried out in this thesis. An overview of the different models have thus been made and is shown in figure 7.2.

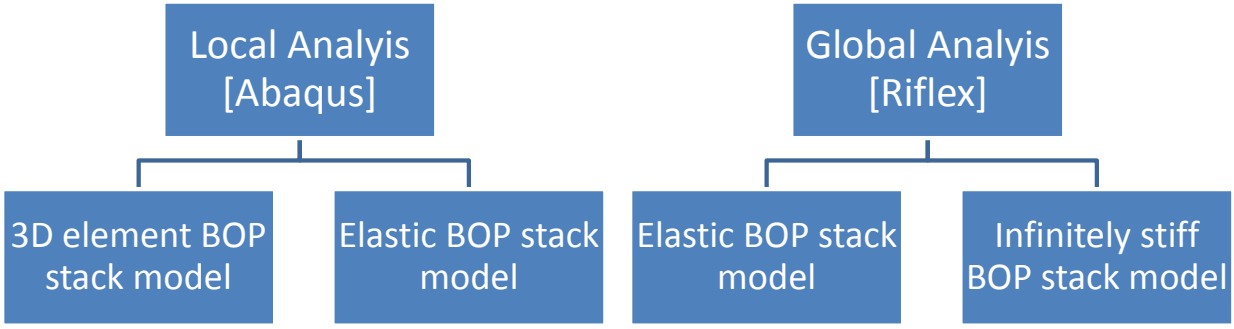

Figure 7.2: BOP stack models - Overview

Chapter 6 treats a general approach for fatigue damage assessment of wellheads and contains a section that addresses local analyses. The local analyses in chapter 6 describe the development of load-to-stress curves for hot spots in the wellhead. This must not be confused with the local analyses which are addressed in this chapter. The purpose of the local analysis in this chapter is to investigate the stiffness properties of the BOP stack.

7.1 Calibration of the Elastic BOP Stack

7.1.1 Local Analysis Model Setup

The purpose of the local analysis was to investigate and quantify the stiffness properties of the BOP stack. The basis for the analysis was a detailed 3D element model of the BOP stack. The 3D element model was provided by Statoil and is shown in figure 7.3.

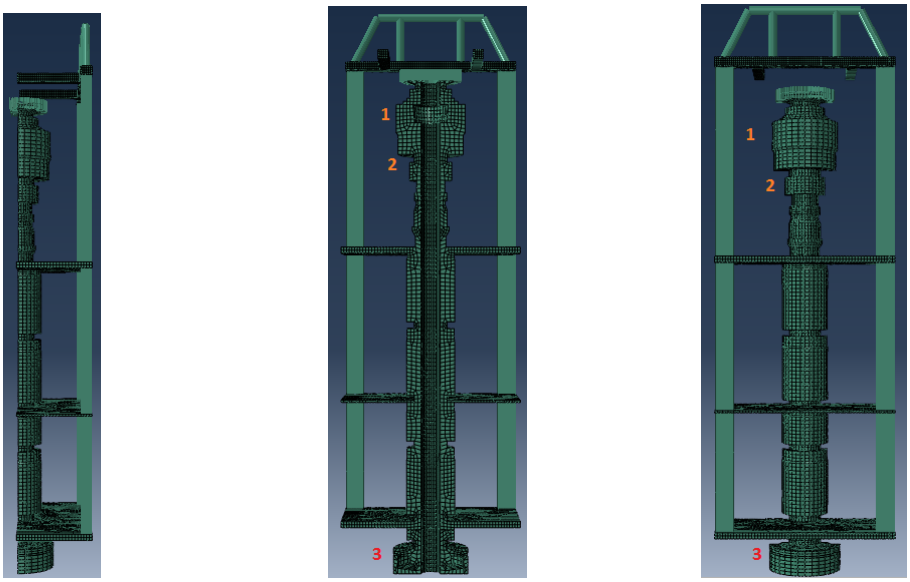

(a) Side view (b) Front view (c) Back view

Figure 7.3: 3D element BOP stack model provided by Statoil

Before the model was imported to Abaqus, the model input file was condensed and sanitized such that the imported model represents an arbitrary BOP stack, thus making it suitable for public dissemination. Before the 3D element model could be applied in analyses, some changes had to be made. These changes comprised redefinition

of material properties, material orientations, constraints that connects the framework to the solid body and nodes that connects the wellhead connector to the body. See appendix A for complete detail of the BOP. The 3D element model does not represent the details of the LMRP connector. Instead it is represented by a rigid transition between the BOP and LMRP, see index 2 in figure 7.3b. Since the connector in the model is rigid, it is reasonable to believe that it is more robust than what is the case in reality. In order to make the LMRP connector less rigid, the area where the LMRP connector is located was edited. By edited, it is meant that the wall thickness in the 3D element model was reduced. The wall thickness in the LMRP section was reduced by 5 % in addition to the sanitation. This modification may affect the final estimated fatigue damage in the wellhead and will be evaluated in chapter 8. The specifics of the 3D element BOP stack model in its revised form are given in table 7.1.

Mass (dry weight)	190×10^3	[kg]
Mass (in water)	162×10^3	[kg]
Center of gravity (x,y,z)	(0 , 0 , 7.57)	[m]
Height	12.4	[m]
Material density	7850	[kg/m^3]

Table 7.1: 3D element BOP stack model specifics

The boundary conditions for the detailed BOP model can be found in table 7.2 where I means fixed and O means free. The purpose of the local analysis was to quantify

	X	Y	Z	RX	RY	RZ
Bottom	I	I	I	I	I	I
Symmetry plane	O	I	O	I	O	I

Table 7.2: Boundary conditions of the detailed BOP model

the stiffness properties of the BOP stack so that it could be implemented in the global model. The global model is built in Riflex which means that the BOP stack must be modelled as a beam. This beam should have the same stiffness properties as the 3D element model. Consequently a beam was modelled in Abaqus. The idea was to calibrate this beam so that its stiffness properties are the same as the 3D element model. In order to investigate the stiffness characteristics of the 3D element model, loads were applied. The magnitude of these loads was obtained from global analyses of the drilling system.

7.1.2 Establishment of Load Pattern

The BOP stack is mainly subjected to loads from the riser, as described in chapter 4. In Riflex, the riser is connected to the BOP stack in the lower flex joint. Hence, this is where the loads are transferred from the riser to the BOP stack. Consequently this is where the loads are applied in the 3D element model, see index 1 in figure 7.3b. The loads acting in the lower flex joint are three dimensional and comprises axial force, bending moment and shear force. These loads vary differently in time, hence it is essential to determine the relative magnitude of these variables. This was done by executing global response analyses of the complete drilling system. Values for shear force, moment, axial force and displacement were extracted at the lower flex joint. A description of how the global model is built can be found in section 7.2.1

For this purpose, three different significant wave heights, H_s, from the scatter diagram in Faltinsen [35] were chosen. The corresponding spectral peak periods, T_p, were selected on the basis of the highest number of wave observations, see bold entries in table 7.8. The three combinations of H_s and T_p were then used to generate irregular sea in Riflex. Irregular sea was generated using a JONSWAP spectrum with three parameters, JONSWAP 3P. The global response analysis had a simulation length of 3700 seconds. One global response analysis was run for each combination of H_s and T_p. The extracted shear force, axial force and moment as well as the displacement were plotted as functions of time. At the time step where the largest displacement was observed, the corresponding shear force, axial force and moment was read. These load pairs were further used to calibrate the elastic BOP model. To avoid the influence of transient effects, the first 100 seconds of the analyses were omitted. The remaining part of the simulation should at this point remain be in a steady-state condition. See appendix B.1 for all plots for this procedure.

The moments that are extracted from Riflex have a negative sign. These moments act clockwise. In the local model, moments were applied to coincide with the coordinate system in Abaqus and the sign may therefore change.

7.1.3 Calibration Procedure

The input stiffness parameters of the elastic BOP stack in the global model should be obtained by calibrating an elastic beam model in Abaqus. The calibration was done by

using the 3D element model of the BOP stack as the frame of reference. The calibration philosophy is shown in figure 7.4. The idea was to calibrate the beam so that its stiffness properties are the same as the 3D element model. The beam was subsequently implemented in the global model in Riflex.

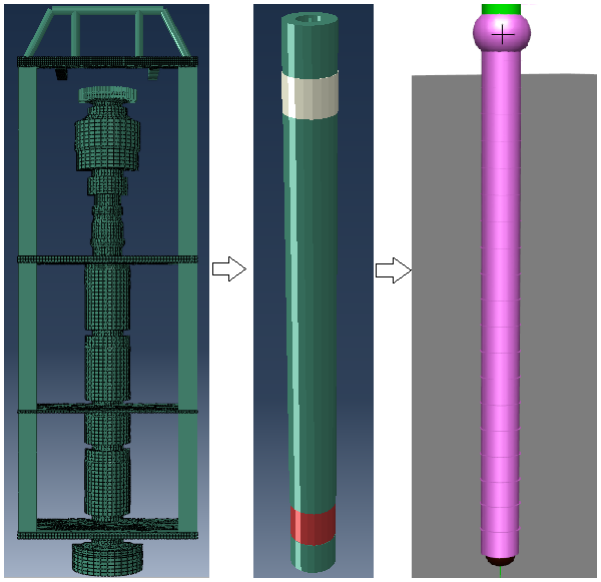

Figure 7.4: BOP calibration philosophy

Initially, the elastic beam model in Abaqus was divided into 5 different segments, as seen in the middle of figure 7.4. The white and red segment represents the LMRP- and wellhead connector, respectively. The idea was to load the 3D element BOP stack model and the elastic beam BOP model with equivalent loads. The calibration was done by comparing the relative displacement between the 3D element model and the elastic beam model.

Loading

In order to carry out the calibration process, the 3D element model had to be loaded with the three load combinations which were obtained from the global response analyses, as described in section 7.1.2. These loads were processed in order to be applicable in the 3D element model.

A challenge is represented by the fact that only half the 3D element BOP was modelled. This challenge was solved by only applying loading in the symmetry plane. Hence,

the BOP stack will only experience displacement in its symmetry plane. For the same reason, the magnitude of the loads gathered from Riflex was halved before implementation. This is to account for the fact that only half the cross sectional area is present and thus only half the stiffness is present.

The 3D element BOP stack consists of 3D solid elements. The nodes in a 3D solid element are not allowed to rotate. This implies that it is not possible to impose pure moment in a single node. This was solved by assigning nodal forces in the vertical direction with opposite sign. This created a moment about the mid point of the lower flex joint as shown in figure 7.5. The magnitude of the point loads was calculated using Excel and a summary of these calculations are shown in appendix B, section B.2

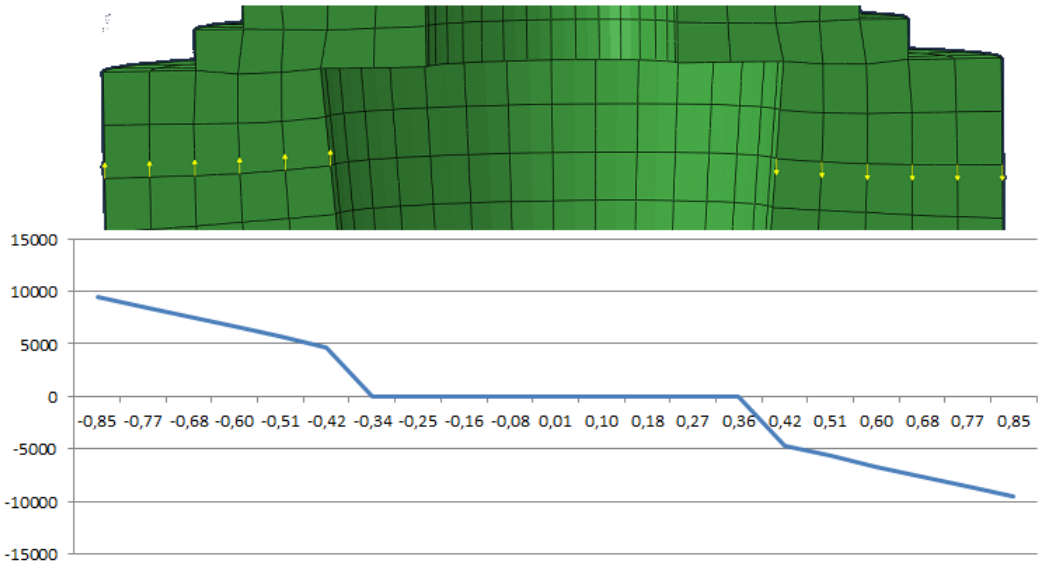

Figure 7.5: Moment distribution [N m]

Abaqus allows the loading to be applied in different steps. This option makes it possible to impose gravity loads in one step. In the next step the axial force, shear force and moment were implemented. To avoid local yielding, the forces were divided on twelve different nodes at the same vertical location. The gravity loads were implemented in terms of an acceleration of 9.81 $\frac{m}{s^2}$. The density of the steel was changed from 7850 $\frac{kg}{m^3}$ to 6825 $\frac{kg}{m^3}$ to account for the presence of sea water.

The same load characteristics applied in the 3D element BOP were also applied in the elastic beam model. All the loads were implemented in one single node. Since the beam is fully modelled and axi-symmetrical, it was not necessary to process the loads.

Calibrating the elastic beam model

The purpose of the calibration was to obtain an elastic beam model which has the same stiffness properties as the 3D element BOP stack model. The calibration was conducted by visually comparing displacement curves between the 3D element model and the elastic beam model. The calibration process was considered to be successful when the displacement curves coincided.

The main parameter which affects the displacement magnitude of the elastic beam model is the bending stiffness, EI. The Young's modulus, E, is a material parameter and may not be changed. This implies that the second moment of area, I, must be changed. The formula for the second moment of area for a pipe may be written as:

$$I = \frac{\pi}{64}\left(d_o^4 - d_i^4\right) \tag{7.1}$$

The inner diameter of the pipe, d_i, is set to $18\,3/4''$ as a default parameter. It is thus only possible to alter the outer diameter, d_o. The thickness of the elastic beam model was altered to obtain new displacements. If the displacements relative to the 3D element model were to small, the beam model was too stiff. Consequently the pipe diameter in the elastic beam model was reduced. If the displacements relative to the 3D element model were to large, the beam model was too elastic. Consequently the pipe diameter in the elastic beam model was increased. Plotting of results after each run as done in Matlab[1] and calculation of input parameters was done in Excel. The method may be described as a trial and error process, the input parameters (different pipe thickness) for each run were decided on the basis of engineering judgement. A more thorough description of the calibration process is found in appendix B.3.

7.2 Global Response Analysis

In this thesis, the effects of BOP stack modelling on estimated wellhead fatigue damage are investigated. This implies that global response analyses must be conducted for two separate global models. The global models are identical with the exception of the BOP

[1]Matlab: "A high-level language and interactive environment for numerical computation, visualization, and programming" [63]

stack structural properties. One global model comprises of an infinitely stiff BOP stack. The other global model comprises of an elastic BOP stack.

7.2.1 Model Setup

In this section, a description of the overall global model configuration is given, see table 7.3. The global analyses are conducted in Riflex and carried out in water depth set to 350 meter. The coordinate system is set with the origin at mean sea level. The start points in table 7.3 refers to the coordinate at the top of each component. The flex joints and the RAO of the support vessel are not listed in the table. The upper flex joint is located at the top of the riser. The RAO is located at mean sea level. The lower flex joint connects the bottom end of the riser to the BOP stack.

	Start point [m]	Length/component [m]	No. of components
10′ Joint	30.18	3.05	1
30′ Joint	27.13	9.14	2
75′ Naked joint	8.85	22.86	6
75′ Buoy. joint	−128.31	22.86	9
10′ Riser joint	−334.05	3.05	1
BOP stack	−337.1	11.40	1
Wellhead	−348.50	4.6	1

Table 7.3: Overall model configuration

Riser

The riser was modelled by use of several different riser joints. Each riser joint has its own set of properties. These are listed in table 7.4. The lower part of the riser, which

	75′ Buoy. Joint	75′ Joint	30′ Joint	10′ Joint	
Mass per unit length	1000	600	730	1100	[kg/m]
Buoyancy area, AE	1.05	0.3	0.32	0.38	[m^2]
Axial stiffness, EA	7.06×10^9	〃	〃	〃	[N]
Bending stiffness, EI	2.3×10^8	〃	〃	〃	[N m^2]
Torsion stiffness, GI	4.4×10^4	〃	〃	〃	[N m^2]
Hydrodynamic diameter	1.25	0.50	〃	〃	[m]

Table 7.4: Riser Joint Properties

is connected to the BOP stack, is commonly a 10 foot naked joint. Upwards from this joint, the riser was modelled with as many 75 foot joints as possible. The riser should end about 30 meter above sea level as this is commonly the position of the drill deck. The choice of top joints was decided to accommodate this.

Proper tension in the riser is desirable to prevent buckling of the riser and to make sure that the LMRP may be disconnected easily at all time. Rune Yttervik proposed that the tension in the LMRP connector should be 50 tonnes and the top tension should be in the vicinity of 300 tonnes. The top tension was applied in Riflex to the line right beneath the upper flex joint. The desired tension in the LMRP connector was obtained

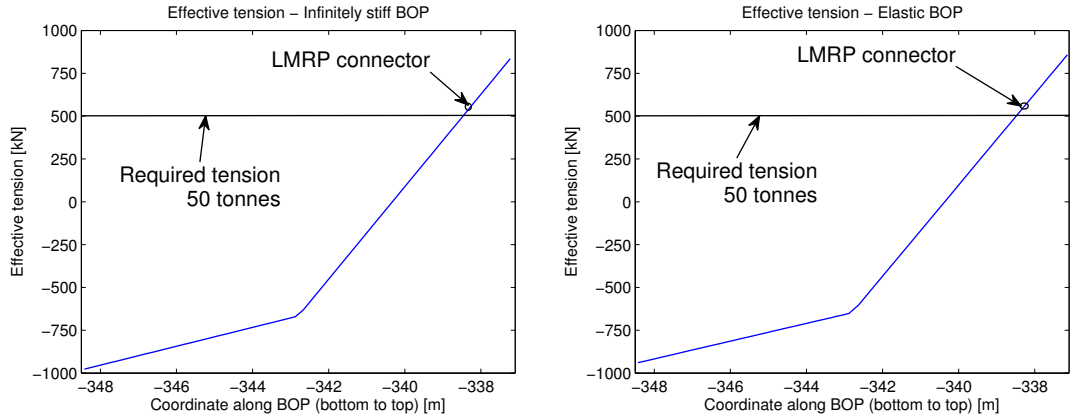

(a) Infinitely stiff BOP (b) Elastic BOP

Figure 7.6: Effective tension in the BOP stack

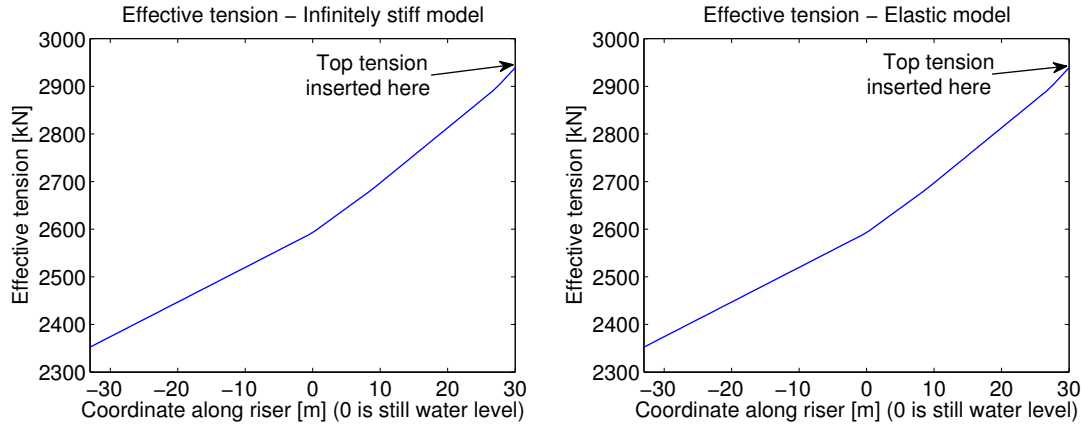

(a) Infinitely stiff model (b) Elastic model

Figure 7.7: Effective tension in the upper part of the riser

iteratively by applying buoyancy elements to some 75 foot joints and followed by a static

analysis. The static analysis yields the tension in the riser and the BOP stack. The number of buoyancy elements was altered until the desired tension of 50 tonnes in the connector was obtained. The final riser setup that satisfies this tension requirement is found in table 7.3. The tension characteristics for the riser and BOP stack are plotted in figure 7.7 and 7.6, respectively. The buoyancy joints were placed well below the free surface. This ensures that the riser response is kept to a minimum.

Support vessel

The support vessel was modelled by inserting a set of displacement RAOs at mean sea level. The displacement RAOs describe the response of the support vessel in all six degrees of freedom. RAOs are separated by different wave attack angels. In the global response analyses, waves are exclusively propagating in the x-direction. Hence, RAOs describing any other direction were omitted. Consequently the RAOs for sway, roll and yaw were omitted. The RAO describing surge direction is given below, while the RAOs for heave and pitch can be found in appendix C.

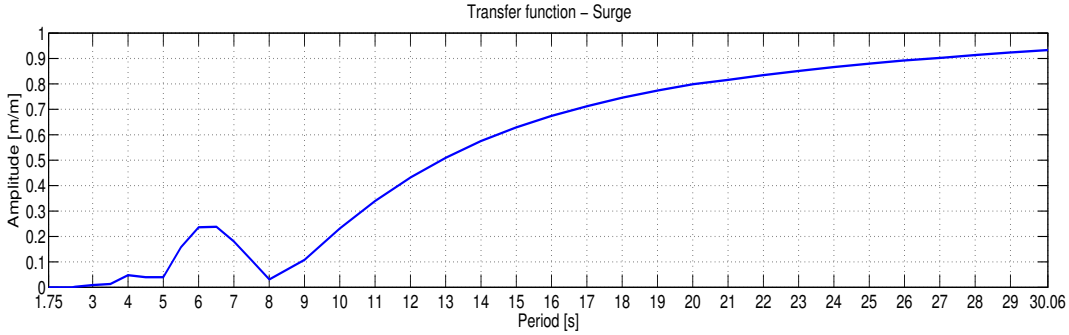

Figure 7.8: RAO - Surge - Amplitude ratio

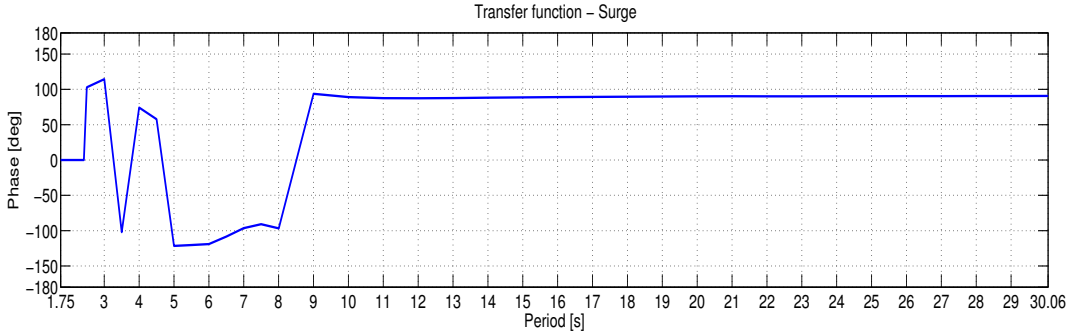

Figure 7.9: RAO - Surge - Phase

Blowout preventer stack

Global response analyses were conducted for two separate global models. The global models are identical with the exception of the BOP stacks structural properties. One global model comprises of the infinitely stiff BOP stack. The other global model comprises of the elastic BOP stack. In both global models the length of the BOP stack was considered as the distance between the wellhead datum and the mid point of the flex joint in the 3D element model. However, the mass comprises the entire 3D element BOP stack model, see table 7.1. To conserve the mass of the 3D element BOP model and to obtain the correct center of gravity, both the elastic BOP model and the infinitely were split into sections. The key parameters of the infinitely stiff BOP stack model is summarized in table 7.5 and the key parameters of the elastic BOP stack is summarized in table 7.6. More detailed information can be found in appendix C, section C.3. To represent the stiffness properties of the elastic BOP stack model, it was required

	Length [m]	Mass/length [kg/m]	EI [N m^2]	EA [N]
Section 1	5.70	5731	1×10^{11}	1×10^{12}
Section 2	5.70	27 602	1×10^{11}	1×10^{12}

Table 7.5: Key parameters infinitely stiff BOP

to split it into a higher number of sections than the infinitely stiff BOP stack model. Nevertheless, the two BOP models have the same center of gravity and total mass.

	Length [m]	Mass/length [kg/m]	EI [N m^2]	EA [N]
Section 1	0.70450	5731	8.089×10^9	1.134×10^{11}
Section 2	0.79444	5731	7.390×10^9	1.072×10^{11}
Section 3	4.20106	5731	8.089×10^9	1.134×10^{11}
Section 4	4.097	27 602	8.089×10^9	1.134×10^{11}
Section 5	0.70354	27 602	8.833×10^9	1.198×10^{11}
Section 6	0.89946	27 602	8.089×10^9	1.134×10^{11}

Table 7.6: Key parameters elastic BOP

Wellhead system

The wellhead system was modelled as a beam with a corresponding spring. The procedure for generating this model is described in section 6.1.3 and is in accordance with the JIP [3]. The extent of creating this model is large and requires a detailed model of the wellhead system and all its components. This is not a part of the thesis and the wellhead system data was hence provided by Statoil. The specifics of the beam are given in table 7.7.

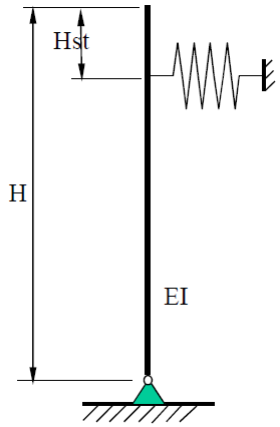

Figure 7.10: Wellhead beam model [3]

Length, H	4.6	[m]
Stick up, Hst	1.5	[m]
Axial stiffness, EA	9.6×10^7	[kN]
Bending stiffness, EI	1.4×10^6	[kN m^2]
Torsion stiffness, GI	6.7×10^5	[kN m^2]
Stiffness lateral spring	35×10^3	[kN/m]
Position lateral spring below wellhead datum	1	[m]

Table 7.7: Soil Beam Model

The lower end of the wellhead beam model was placed 3.1 meter into the soil, with the lateral spring positioned 0.5 meter above the seabed. The wellhead beam model stretches up to 1.5 meter above the seabed. The wellhead beam model is fixed from translations at the lower end, but is free to rotate about x and y axis.

Flex joint

The lower flex joint connects the BOP stack to the riser and the upper flex joint connects the riser to the support vessel. Flex joint stiffness is often assumed to be linear. Linear stiffness represents a simplification of the lower flex joints non-linear stiffness. Thus, non-linear stiffness characteristics for typical flex joints were applied. The specifics can be found in appendix C in table C.7 and C.8.

7.2.2 Input to the Global Response Analysis

Environment

The sea states which were employed were selected from a scatter diagram from the North sea, taken from Faltinsen [35]. Drilling operations are rarely carried out in waves higher than 8 meter. This acts as the upper boundary for the significant wave heights sampled from the scatter diagram. All of the sea states within this boundary were employed. This comprises of a total of 128 sea states. See table 7.8 for the complete scatter diagram. Irregular waves were generated by using a JONSWAP wave spectrum with three parameters, JONSWAP 3P. The analyses were conducted with the absence

Spectral peak	Significant wave height [m]								
period [s]	1	2	3	4	5	6	7	8	Sum
3	59	9	0	0	0	0	0	0	68
4	403	212	8	0	0	0	0	0	623
5	1061	1233	146	6	0	0	0	0	2446
6	1569	3223	831	85	4	0	0	0	5712
7	1634	5106	2295	481	57	3	0	0	9576
8	1362	5814	3896	1371	315	39	2	0	12 799
9	982	5284	**4707**	2406	898	207	27	2	14 513
10	643	4102	4456	2960	1564	571	136	20	14 452
11	395	2846	3531	2796	1879	950	347	88	12 832
12	232	1821	2452	2163	1696	**1069**	528	197	10 158
13	132	1098	1543	1437	1228	885	533	**261**	7117
14	74	634	901	849	748	575	387	226	4394
15	41	355	497	458	398	309	217	138	2413
16	22	194	263	231	191	142	98	64	1205
17	12	105	135	110	84	58	37	23	564
18	7	56	67	50	35	21	12	7	255
19	4	30	33	2	13	7	4	2	95
21	2	16	16	10	5	2	1	0	52
22	2	17	15	7	3	1	0	0	45
Sum	8636	32 155	25 792	15 422	9118	4839	2349	1028	99 319

Table 7.8: Joint frequency of significant wave height and spectral peak period [35]

of current. A parameter study on the influence of current was carried out. This study is described in section 7.4.1

Calculation parameters

The global response analyses were carried out using non-linear numerical integration. It may be discussed whether non-linear numerical integration is necessary. The alternative is application of linear numerical integration. It is reasonable to believe that occurrences of non-linearities will be few and have a relatively small impact on the response of the system. Nevertheless, linear numerical integration is not implemented in the SIMA software package at current time. The Newmark-β procedure was chosen. The inverse β parameter was set to 4 which represents the assumption of constant average acceleration between time steps. This is more thoroughly described in section 5.2.2.

Method	Non-Linear Numerical Integration
Procedure	Newmark-β
Invers β	4 (Constant average acceleration)
γ	0.5 (No artificial damping)
Proportional Damping	Updated
Stiffness damping factor	0.02
Mass damping factor	0
Time series length	3700 seconds
Load time increment	1 second
Response time step	0.250 second

Table 7.9: Calculation parameters

The JIP [3] recommends a simulation length of one hour. To avoid the influence of transient effects, the simulation length was set to 3700 seconds. It was estimated that the first 100 seconds contains the transient effects which subsequently were omitted when the results were post-processed.

The time step length is another important parameter in the numerical integration procedure. The time step determines how frequent the response is calculated. A large time step implies a less frequent calculation of the response. Consequently some response amplitudes may not be captured which may lead to an inadequate numerical solution. This may be avoided by using a time step length with good resolution. A good resolution implies obtaining about 10 time steps within an eigenperiod.

For this global model the eigenfrequencies of the system may be divided into two groups. Firstly, the BOP stack which is rigidly connected to the wellhead has certain set of eigenfrequencies. Secondly, the riser which is connected to the BOP by a flex joint has a different set of eigenfrequencies. Despite the fact that a frequency domain eigenvalue

analysis would be the preferred step to make, this option is not implemented in SIMA at current time and is thus not conducted. Instead a global response analysis was conducted. The resulting response was evaluated and it was seen that a time step length of 0.25 seconds gives a resolution which is well above 10 steps per response period. The excitation frequencies must also be considered and this was done by evaluating the smallest spectral peak period in the scatter diagram. This corresponds to a spectral peak period of 3 seconds, i.e. there are 12 time steps within the spectral peak period. This is considered as acceptable.

7.3 Fatigue Damage Assessment

The results from the global response analyses acts as input to the fatigue damage assessment. The assessment was carried out by programming a Matlab script and is identical for the two global models. The chosen procedure is described in this section. The Matlab script can be found in its entirety in appendix D.2.

7.3.1 Calculation of Stress in the Wellhead

Moment-time series at the wellhead datum were imported from Riflex. This was done for all 128 sea states that were simulated. Subsequently, the moment-time series was converted to stress-time series. This conversion was done using load-to-stress curves. These curves were generated with basis in load-to-stress tables provided by Statoil. The tables were provided in terms of discrete points.

To make these points applicable for a mapping algorithm the points were fitted with a line using spline interpolation. This resulting interpolation function describing the line is given as stress as function of moment. This is exemplified in figure 7.11 for cement level 25 meter.

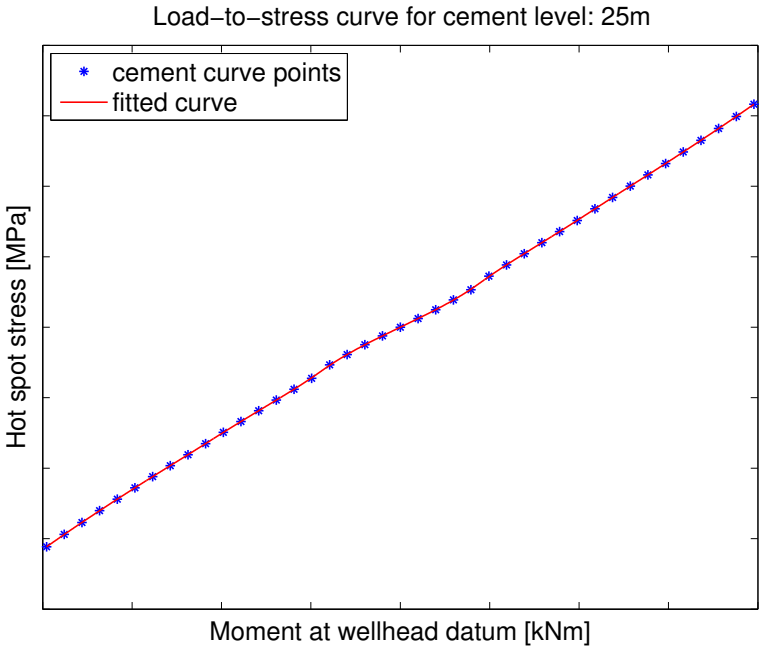

Figure 7.11: Load-to-stress curve - cement level: 25 m

The axes in figure 7.11 have been removed on request from Statoil. The mapping algorithm inserts a discrete moment value in the interpolation function. The product is a discrete stress value. This was done for all discrete moment values. The result was stress-time series which describe the stress variations in the given hot spot. The next step is stress cycle counting.

In conjunction with the fatigue assessment method, uncertainties are related to the modelling of cement between the conductor and wellhead housing. Reinås *et al.* [4] describe a significant sensitivity of cement modelling with respect to estimated fatigue damage in the wellhead. They emphasize the importance of effective cement level between the 30″ conductor and the 20″ surface casing. With effective cement level it is meant the goodness of the connection between the casings and cement. To account for this uncertainty, different load-to-stress tables were provided for different cement levels; 0 m, 2 m, 5 m, 10 m, 20 m and 25 m beneath mudline. It is expected that the different load-to-stress tables will estimate different fatigue damage. The tables were provided for a hot spot which is located in a weld which connects the wellhead to the 20″ casing.

7.3.2 Cycle Counting

Stress cycles were counted using WAFO[2] functions [64]. The counting procedure starts with the recognition of turning points. The turning points are local stress peaks or valleys. Further a rainflow counting algorithm is employed. The output from the algorithm is two vectors. One vector contains whole cycles, the other vector contains half cycles. It is still debated in the literature how to handle the half cycles. Some ignore them, some count them as a whole cycles and some count them as half cycles [65]. In this procedure, half cycles were counted as half cycles.

Stress cycles that have the same stress range are put in the same stress range bin. The number of stress cycles in each bin is counted. In regards to half cycles, the number of cycles in each bin is divided by two. Stress ranges are governing in calculations of fatigue damage.

7.3.3 Fatigue Damage Calculation

The fatigue damage was calculated using Palmgren-Miner summation

$$D = \frac{1}{\bar{a}} \sum_{i=1}^{k} n_i (\Delta\sigma_i)^m \tag{7.2}$$

The SN input to equation 7.2 depends on the choice of SN curve. SN input was gathered from DNV-RP-C203 [31]. Fatigue damage was calculated by the use of SN curve class: F1. This is an SN curve with two slopes. As described in section 3.3.1, SN curves with two slopes represent variable amplitude loading. This meant that the Palmgren-Miner summation formula had to be be rewritten to a piecewise defined equation.

$$D = \begin{cases} \frac{1}{\bar{a}(m_1)} \sum_{i=1}^{k} n_i (\Delta\sigma_i)^{m_1}, & \text{for } q \leq \Delta\sigma < \infty \\ \frac{1}{\bar{a}(m_2)} \sum_{i=1}^{k} n_i (\Delta\sigma_i)^{m_2}, & \text{for } 0 < \Delta\sigma < q \end{cases} \tag{7.3}$$

[2]WAFO:A toolbox of Matlab routines for statistical analysis and simulation of random waves and random loads [64]

where

i : Stress range number i

k : Total number of stress ranges

q : Corresponding stress value for knee point for SN curve

$\bar{a}$: SN curve parameter where $\log \bar{a}$ represents the intercept with the $\log N$ axis

n_i : Number of stress cycles in stress bin i

m : Inverse slope of SN curve, $m_1 = 3$, $m_2 = 5$

$\Delta\sigma$: Stress Range for stress block i

The fatigue damage, D, was calculated for one sea state at the time. This implies that the Matlab script was looped with respect to the different combinations of spectral peak periods and significant wave heights. The SN curve class: F1, in DNV-RP-C203 [31], contains two slopes. Hence, the damage had to be calculated with respect to which slope each stress cycle corresponded to. The total weighted damage, D_{total}, for all sea states for a one hour operation is then

$$\begin{aligned} D_{\text{total}} &= \sum_{l=1}^{S} \frac{N_l}{N_{\text{total}}} \cdot D \\ &= \sum_{l=1}^{S} \frac{N_l}{N_{\text{total}}} \cdot \begin{cases} \frac{1}{\bar{a}(m_1)} \sum_{i=1}^{k} n_i (\Delta\sigma_i)^{m_1}, & \text{for } q \leq \Delta\sigma < \infty \\ \frac{1}{\bar{a}(m_2)} \sum_{i=1}^{k} n_i (\Delta\sigma_i)^{m_2}, & \text{for } 0 < \Delta\sigma < q \end{cases} \end{aligned} \tag{7.4}$$

where, in addition to equation 7.3,

D_{total} : Total weighted fatigue damage for one hour operation

l : Sea state number l

S : Number of sea states

N_l : Number of observations for sea state l

N_{total} : Total number of sea state observations

Equation 7.4 can be explained in the following way. For sea state, l, the fatigue damage, D, was calculated. The fatigue damage, D, was multiplied by the probability of occurrence for that sea state, $\frac{N_l}{N_{\text{total}}}$. The probability of occurrence for each sea state

is given in table 7.10. In this way the calculated fatigue damage was weighted. This was done for all sea states, from 1 to S. All the weighted damage contributions were summed up yielding the total damage for one hour in the given hot spot.

Spectral peak period	Significant wave height [m]								
[s]	1	2	3	4	5	6	7	8	Sum
3	0.0594	0.0091	0	0	0	0	0	0	0.0685
4	0.4058	0.2135	0.0081	0	0	0	0	0	0.6273
5	1.0683	1.2415	0.1470	0.0060	0	0	0	0	2.4628
6	1.5798	3.2451	0.8367	0.0856	0.0040	0	0	0	5.7512
7	1.6452	5.1410	2.3107	0.4843	0.0574	0.0030	0	0	9.6417
8	1.3713	5.8539	3.9227	1.3804	0.3172	0.0393	0.0020	0	12.8868
9	0.9887	5.3202	4.7393	2.4225	0.9042	0.2084	0.0272	0.0020	14.6125
10	0.6474	4.1301	4.4866	2.9803	1.5747	0.5749	0.1369	0.0201	14.5511
11	0.3977	2.8655	3.5552	2.8152	1.8919	0.9565	0.3494	0.0886	12.9200
12	0.2336	1.8335	2.4688	2.1778	1.7076	1.0763	0.5316	0.1984	10.2277
13	0.1329	1.1055	1.5536	1.4469	1.2364	0.8911	0.5367	0.2628	7.1658
14	0.0745	0.6383	0.9072	0.8548	0.7531	0.5789	0.3897	0.2275	4.4241
15	0.0413	0.3574	0.5004	0.4611	0.4007	0.3111	0.2185	0.1389	2.4295
16	0.0222	0.1953	0.2648	0.2326	0.1923	0.1430	0.0987	0.0644	1.2133
17	0.0121	0.1057	0.1359	0.1108	0.0846	0.0584	0.0373	0.0232	0.5679
18	0.0070	0.0564	0.0675	0.0503	0.0352	0.0211	0.0121	0.0070	0.2567
19	0.0040	0.0302	0.0332	0.0020	0.0131	0.0070	0.0040	0.0020	0.0957
21	0.0020	0.0161	0.0161	0.0101	0.0050	0.0020	0.0010	0	0.0524
22	0.0020	0.0171	0.0151	0.0070	0.0030	0.0010	0	0	0.0453
Sum	8.6952	32.3755	25.9688	15.5277	9.1805	4.8722	2.3450	1.0350	100

Table 7.10: Probability of occurrence for sea states - scale factor $\times 100$

The expected fatigue life in days was calculated on the basis of weighted fatigue damage for one hour:

$$\text{Fatigue life} = \frac{1}{24_{\text{hours}} \cdot D_{\text{total}}} \tag{7.5}$$

It is emphasized that this estimate is only valid as long as the global configuration of the drilling system remains the same. In addition the sea states must keep occurring with the same rate as used for input for the one hour fatigue damage calculation.

The stress range bins and the corresponding number of cycles in the bins were plotted

as stress range histograms. This was done to enable an evaluation of stress range distributions for each sea state. A weighted stress range histogram was obtained by weighting the stress range histograms for each sea state. The principle is illustrated in figure 7.12. The weight factors are the probability of occurrence for the sea states in table 7.10.

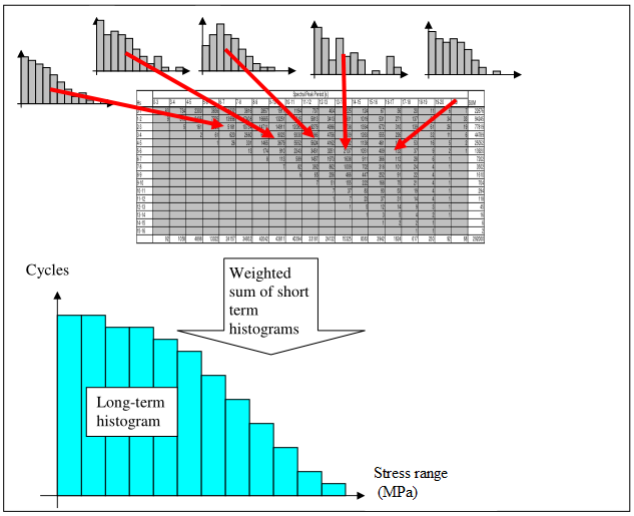

Figure 7.12: Weighting of stress range histograms - principle [3]

7.4 Parameter and Sensitivity Study

The analyses that have been described have been conducted in an environment without the presence of current. Current is assumed to affect the estimated fatigue life. In addition, there are other parameters that can affect the estimated fatigue damage. Such parameters are lower flex joint stiffness and the global damping factor (potential damping). Global response analyses were conducted in both global models where these parameters were changed in order to investigate the influence on estimated fatigue damage. However, the most important factor to investigate is the relative difference in estimated fatigue damage with respect to the two BOP stack models.

The 3D element model of the BOP stack does not represent the details of the LMRP and wellhead connectors. Hence it is reasonable to assume that the stiffness in these areas is too high. It is thus of interest to alter the elastic BOP model. The alteration was done by changing the bending stiffness of the elastic BOP model in the sections

that corresponds to the location of the connectors. Consequently the relative difference in estimated fatigue damage may prove to be of greater between the infinitely stiff BOP model and the elastic BOP model. A bending stiffness sensitivity study was conducted to investigate the influence of connector stiffness on estimated fatigue life.

The studies which are described are carried out individually and do not influence one another.

7.4.1 Current

Application of a low velocity current profile in the global response analyses was conducted in order to assess the relative difference in terms of estimated fatigue damage between the two BOP stack models. On recommendation from Rune Yttervik, the current profile employed was $0.1\,\mathrm{m\,s^{-1}}$ the first 200 meter below still water level and diminishes linearly to zero at 350 meter below still water level. It follows that this current profile does not necessarily reflect an accurately measured current profile. It has been emphasized how detailed and accurate current measurements affect estimated fatigue damage [10]. However, this study makes it possible to validate the assumption that current yields conservative fatigue damage estimates.

7.4.2 Structural Damping Factor

Structural damping is usually hard to determine and is often alternatively determined by a linear combination of mass and stiffness, $\boldsymbol{C} = \alpha_1 \boldsymbol{M} + \alpha_2 \boldsymbol{K}$. In the main study, α_1 was set to 0 and α_2 was set to 0.02. Similar to analyses the conducted by Reinås *et al.* [9], α_2 was set to 0.01.

7.4.3 Lower Flex Joint Stiffness

The stiffness of the lower flex joint affects the transfer of loads from the riser to the BOP stack, and will thus influence the moments at the wellhead datum. The main study was carried out with non-linear lower flex joint stiffness. In this study, a linear lower flex joint stiffness was applied. The stiffness was based on a linearisation of the non-linear stiffness, between 0 and 10 degrees deflection. The non-linear stiffness properties is found in table C.8. The linearised stiffness is 93 $^{\mathrm{kN\,m}}/_{\mathrm{deg}}$.

7.4.4 Bending Stiffness

The bending stiffness in the sections which corresponds to the wellhead connector and LMRP connector may be overly stiff. The bending stiffness for these two sections was obtained by conducting a calibration procedure. The obtained bending stiffness for the wellhead and LMRP connector is 7.39×10^9 N m^2 and 8.83×10^9 N m^2, respectively. In this study the bending stiffness was altered in section 2 and 5 in the global model. This was done to investigate the impact this may have on the estimated fatigue damage. It is noted that the obtained bending stiffness for these two sections are not the same. However, in this parameter study, the same bending stiffness was applied in both sections. The following bending stiffness was applied: 1×10^8 N m^2 and 5×10^8 N m^2, 1×10^9 N m^2 and 5×10^9 N m^2 and finally 1×10^{10} N m^2 and 5×10^{10} N m^2.

It is emphasized that there is no certainty that the actual bending stiffness in the wellhead connector and LMRP connector lie in the listed domain. However, the study will reveal the estimated fatigue damage sensitivity to change in connector bending stiffness.

Chapter 8

Results and discussion

In this chapter results from the analyses are presented. The results will be discussed and assumptions that are made will be addressed.

The following studies were conducted: One main study, three parameter studies and six sensitivity studies. For each study, it was required to carry out two global response analyses in Riflex. One for the global model that comprises the infinitely stiff BOP stack model and one that comprises the elastic BOP stack model. For each global model, 128 different sea states was simulated for 3700 seconds. The CPU time for each global model was approximately five hours.

8.1 Calibration of the Elastic BOP Stack

8.1.1 Establishment of load patterns

Global response analyses were carried out to establish load patterns that could be applied in the 3D element model. It was initially assumed that the displacement of each node in the 3D element BOP stack model would vary approximately linearly with the load. This implies that if the applied load is doubled, the displacement is doubled. This must though not be misunderstood with the relative displacement between each node which is non-linear.

Based on this assumption, three sea states were selected. For each sea state, a global response analysis was carried out in Riflex. It was assumed that the loads which are transmitted from the riser act in the rotation point of the lower flex joint. Hence, this point became the reference point from which results were gathered in Riflex. Further, axial force, shear force, moment and lateral displacement were plotted in time, see figure 8.1. An assumption was that the combined load pattern was greatest when the

displacement is largest. The time step with the largest displacement is marked with red marker, see figure 8.1. Hence, this load pattern was applied in the calibration process. The load patterns for each of the selected sea states are shown in table 8.1. The specifics of the establishment of load patterns are given in appendix B.1

	Sea state #1	Sea state #2	Sea state #3	
T_p	13	12	9	[s]
H_s	8	6	3	[m]
Axial force	8.06×10^5	8.14×10^5	7.78×10^5	[N]
Moment	-2.82×10^5	-2.52×10^5	-1.71×10^5	[N m]
Shear force	6.32×10^4	5.63×10^4	4.02×10^4	[N]
Displacement	0.0818	0.0734	0.0523	[m]

Table 8.1: Forces, moments and displacements in lower flex joint at corresponding sea states

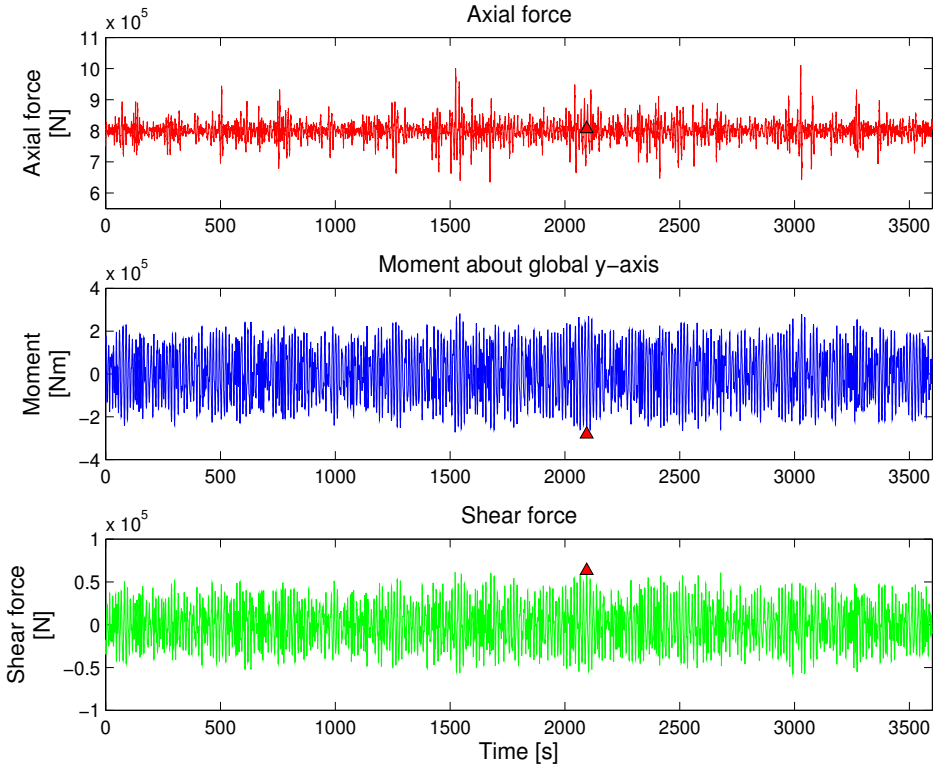

Figure 8.1: Load combination for $H_s = 8$, $T_p = 13$, at time of max displacement

Loads were extracted at the location of the lower flex joint. Subsequently, these loads were processed and then implemented in Abaqus. The loads were applied to the 3D element BOP stack model and the elastic BOP stack model. The load pattern from the sea state with significant wave height 8 meter and spectral peak period 13 seconds was chosen as input parameters for the calibration process. The loads from the two other sea states were used to verify if the assumption of linear varying displacement is correct.

8.1.2 Calibration Procedure

An elastic beam model of the BOP stack was modelled and calibrated as described in section 7.1.3. The idea was to calibrate the beam so that its stiffness properties are the same as the 3D element model. The beam was subsequently implemented in the global model in Riflex. The inner diameter of the BOP stack, as well as the Young's modulus of steel are fixed parameters. The thickness of the elastic beam model were thus altered. Satisfying displacement resemblance between the elastic BOP model and the 3D element model was obtained after 5 runs. The main results from the calibration process are given in table 8.2. A thorough description of this calibration procedure can be found in appendix B.3.

Run\Section	1	2	3	4	5
1st run	0.25	0.05	0.25	0.05	0.025
2nd run	0.5	0.2	0.5	0.3	0.5
3rd run	0.38	0.2	0.38	0.2	0.38
4th run	0.25	0.25	0.25	0.25	0.25
5th run	0.24	0.23	0.24	0.45	0.25

Table 8.2: Calibration of pipe thicknesses [m] of the elastic BOP stack model

The mass of the elastic BOP model was set equal to twice the mass of the 3D element model to account for symmetry modelling. The center of gravity was not considered. There are two reasons for this. Firstly, the expected displacement is in the range of millimetre and gravity will hence not contribute significantly to bending. Secondly, no velocity or acceleration is present and inertial forces are thus negligible. The calibration process involved visual evaluation of the displacements of the 3D element BOP stack model and the elastic BOP stack model. Selected displacement plots are shown in figure 8.2.

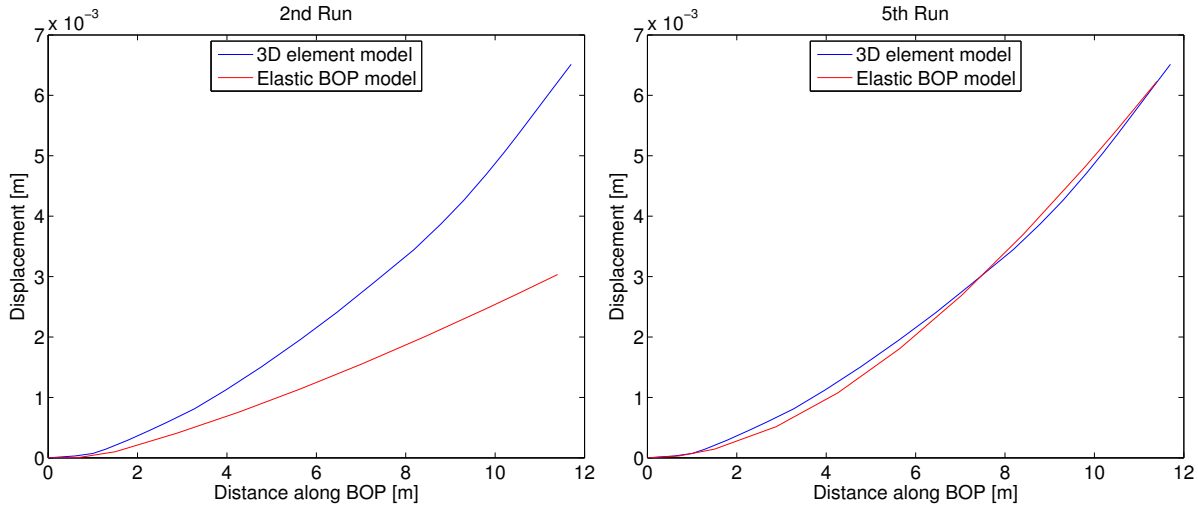

Figure 8.2: 2nd and 5th run of the calibration procedure, load pattern from $H_s = 8$, $T_p = 13$

The calibration procedure resulted in satisfying resemblance in the 5th run, as seen in figure 8.2. The plotting was done for different vertical nodes along the two BOP models. The final properties of the elastic BOP is shown in table 8.3.

	d_i [m]	Thickness [m]	d_o [m]	I [m^4]	EI [N m^2]
Section 1	0.47625	0.24	0.956	0.0385	8.09×10^9
Section 2	"	0.23	0.936	0.0352	7.39×10^9
Section 3	"	0.24	0.956	0.0385	8.09×10^9
Section 4	"	0.25	0.976	0.0421	8.83×10^9
Section 5	"	0.24	0.956	0.0385	8.09×10^9

Table 8.3: Final elastic BOP build - local model

To validate the results from the calibration procedure, load from two other sea states were applied. It is seen in figure 8.3 that satisfying resemblance was achieved also here. The plots and tables for the calibration procedure are given in appendix B and calculation of stiffness parameters from geometrical values are given in table B.8.

An important area of discussion is how realistic the stiffness properties of the 3D element BOP stack model is. Initially, it was assumed that the wellhead and LMRP connectors would contribute significantly to reducing the overall stiffness in the BOP stack. This assumption made the basis for how the sections were distributed in the elastic beam model. The idea was that section two and four would represent the wellhead and LMRP connector, respectively. It was though revealed that the connectors had almost the same

stiffness as the rest of the BOP stack. This explains the continuous displacement field shown in figure 8.2. The reason for this is the fact the connectors are modelled in solid steel. It is reasonable to assume that the stiffness properties of the connectors would be different if they had been modelled in full detail.

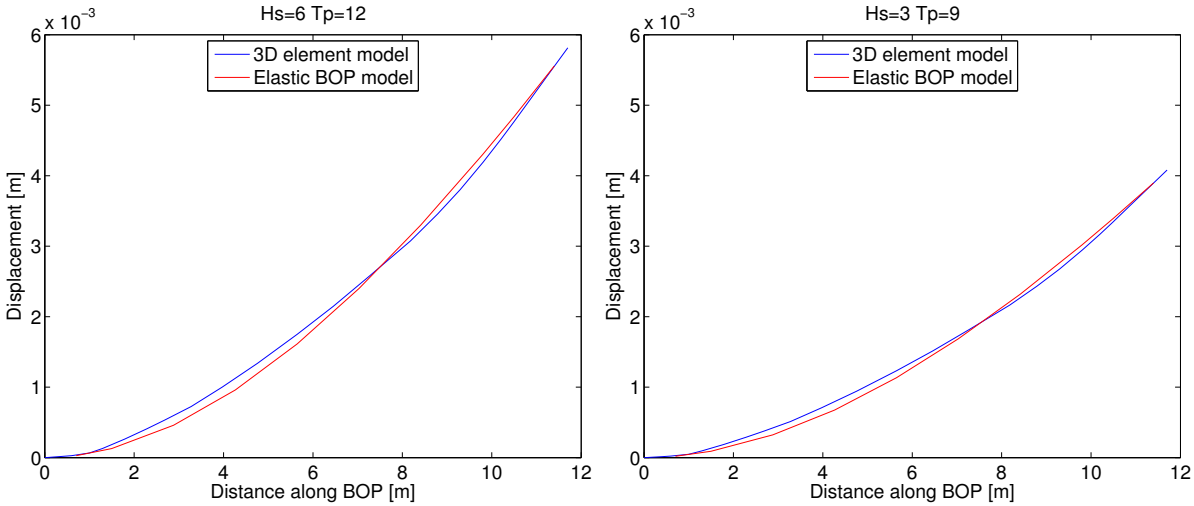

(a) Sea state #2 (b) Sea state #3

Figure 8.3: Verification of the calibration procedure, 3D element model vs. elastic BOP model

If the lowest realistic stiffness of the connectors is of interest than they should be modelled with maximum machining tolerances. Some imperfections could be implemented in the BOP stack model to represent a BOP stack with long service time.

The elastic BOP model that has been developed may be too stiff. This introduces an uncertainty which is an important factor in the evaluation of the final estimated fatigue damage.

8.2 Global Response Analyses

Global response analyses were carried out for two global models. One global model comprises the infinitely stiff BOP stack. The other comprises the elastic BOP stack model. The purpose of the global analysis was to produce moment-time series in the wellhead datum for different sea states. In this section a presentation of the results from the global response analyses is given.

8.2.1 Displacement and Load Characteristics

Semi-submersible motion characteristics

The motion characteristics of the semi-submersible is exemplified for a sea state where $H_s = 8$m and $T_p = 13$s in figure 8.4. It is seen that the semi-submersible oscillates about origin, and has maximum displacement peaks of 2.34 meter in the positive direction and -2.51 meter in the negative direction.

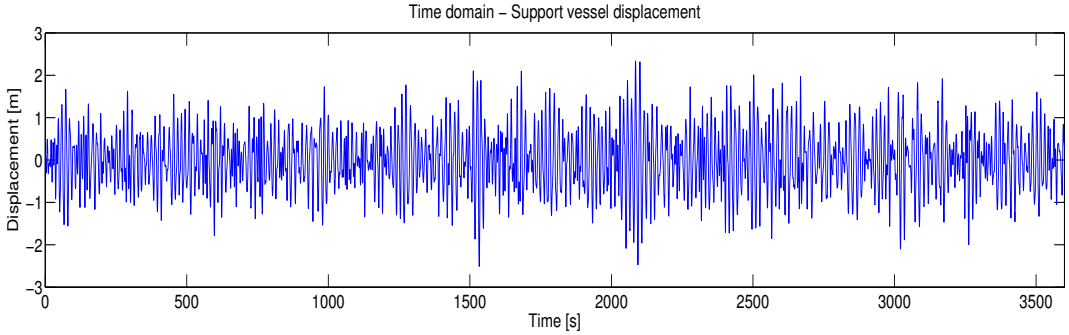

Figure 8.4: Displacement - Time domain, $H_s = 8$m, $T_p = 13$s

The RAOs of the semi-submersible is shown in section 7.2. An uncertainty is connected to the development of the RAOs. It is uncertain if higher order hydrodynamical effects are included. In order to investigate this uncertainty, the time series in figure 8.4 was transformed into the frequency domain using Fast Fourier Transform.

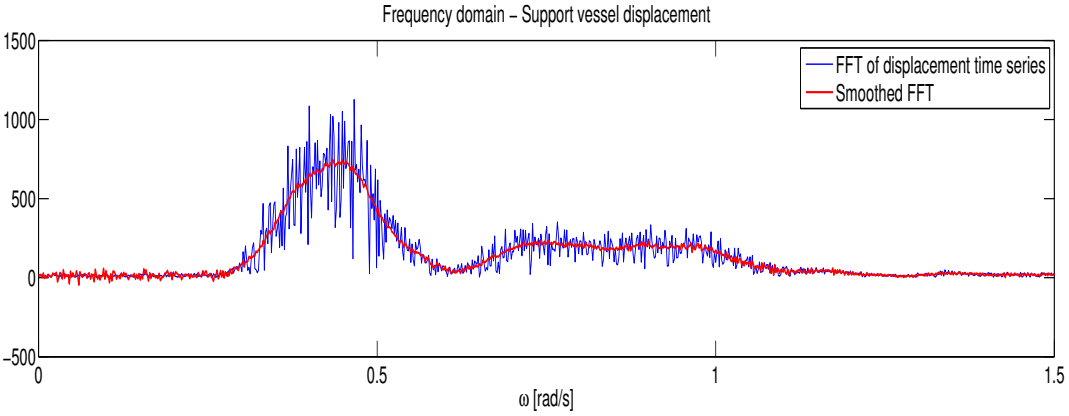

Figure 8.5: Dispalcement - Frequency domain, $H_s = 8$m, $T_p = 13$s

In figure 8.5 it can be seen that the frequencies that excite the semi-submersible the most, lie in the interval of 0.4 to 0.5 rad/s. Some excitation is also seen in the interval

of 0.7 to 1 rad/s. These frequencies are equivalent to periods of 12.5 to 15.7 s and 6 to 9 s. In other words, the semi-submersible is excited by frequencies that lie in the same interval as the wave frequencies. In addition, figure 8.5 shows that there is no excitation in the low frequency area, emphasizing that slowly-varying forces are not included in the RAOs. Hence, the global response analyses carried out in this thesis cannot capture such effects. These are often dominant effects on a moored system. This should be discussed when evaluating estimated fatigue damage.

Drilling system displacement

The drilling system's displacement as a function of time is an important factor in regards the moment distribution in the system and thus the stresses occurring in the wellhead. In figure 8.6 a selected plot of the the maximum displacement during a time series of one hour is shown.

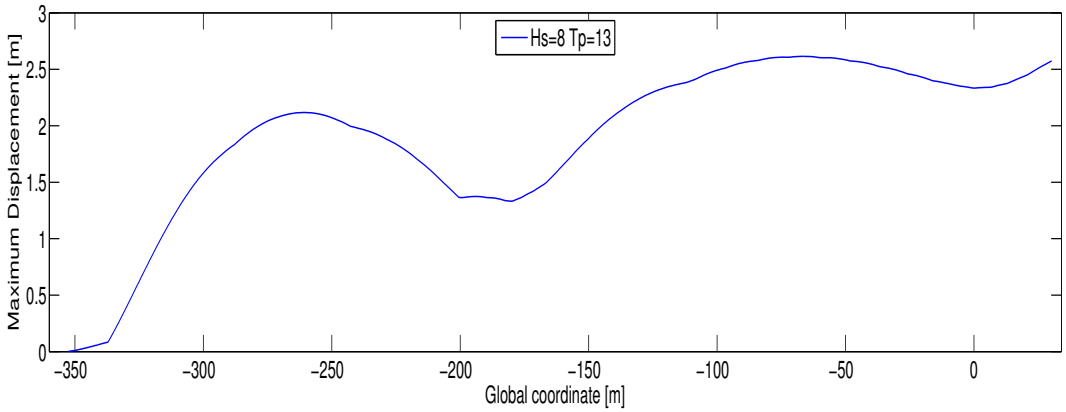

Figure 8.6: Maximum displacement

In the figure it is seen that there is a sudden change in angle in the transition between the BOP stack (to the left) and the riser. This implies the presence of moment and shear force in the lower flex joint. These forces contribute to an amplification of the stress ranges occurring in the wellhead. The angle between the BOP stack and the riser is dependent on the stiffness of the lower flex joint. Hence, the magnitude of shear force and moment is dependent on the stiffness of the lower flex joint. This will be discussed when evaluating the results from the lower flex joint parameter study.

Moments along the drilling system

Figure 8.7 represents the maximum moments along the riser. It is seen that the moment increases drastically when in the area where the wellhead and BOP stack is located. This is due to the sudden increase in bending stiffness in the transition between the riser and the BOP stack.

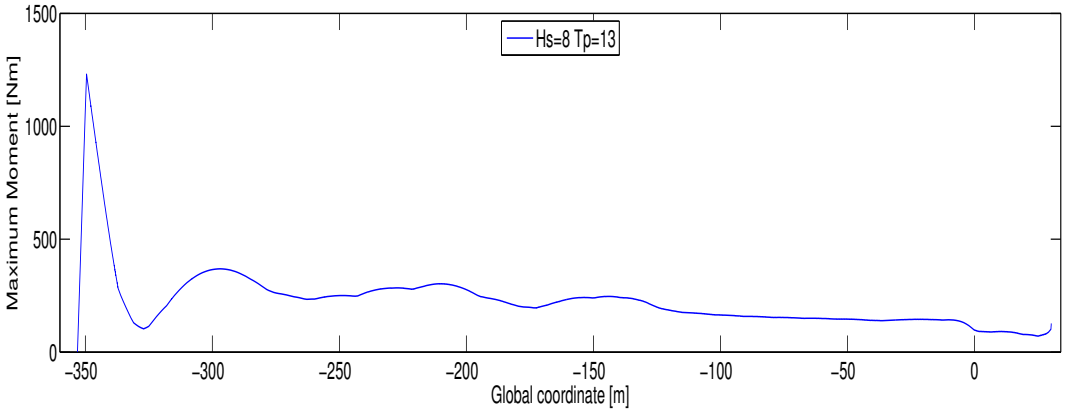

Figure 8.7: Maximum moment

The reduction in moment close to the bottom of the wellhead is due to the boundary conditions of the wellhead model. The wellhead model is shown in figure 7.10 in section 7.2.1. The lower boundary conditions of the wellhead model are free rotation- and fixed translation degrees of freedom. Hence, no bending moment will be present in the lower node of the system.

BOP stack curvature and displacement

The two BOP stack models comprises of different bending stiffness. A difference in regards to curvature along the riser was hence expected. Figure 8.8 represents the curvature for the two BOP stack models for one sea state, and plot(a) reflects the impact given by the LMRP and wellhead connector. Plot(a) also represents greater curvature than plot(b), though the magnitude of the curvature for both BOP stack models are small.

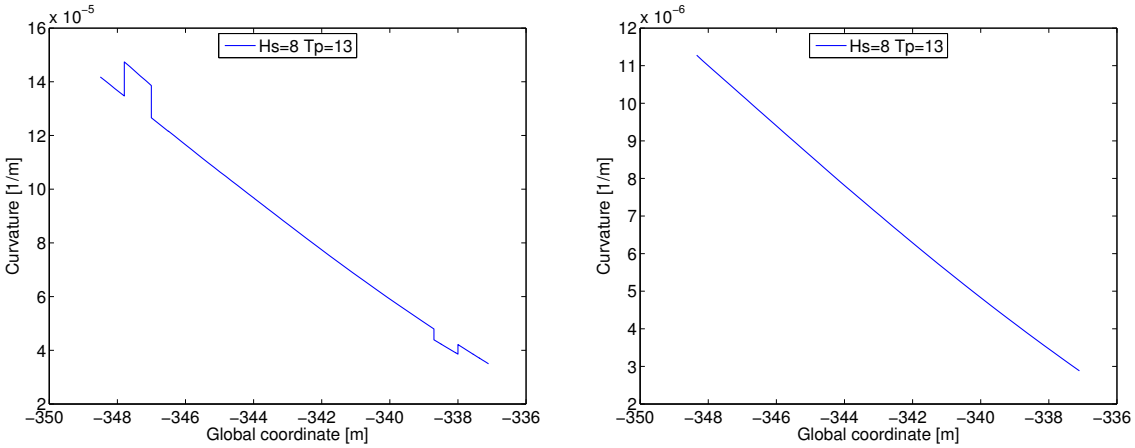

(a) Elastic BOP stack

(b) Infinitely stiff BOP stack

Figure 8.8: Maximum Curvature

Maximum displacements of the two BOP models are extracted from a global response analysis with sea state $H_s = 8$m, $T_p = 13$s and plotted in figure 8.9. The effects of BOP stack elasticity are evident in the figure. The elastic BOP bends slightly, resulting in a non-linear displacement pattern along the BOP length. Hence the elastic BOP stack model has a slightly larger displacement at the top end compared to the infinitely stiff BOP stack model. The infinitely stiff BOP stack model does not bend and has thus a linear displacement pattern along its length.

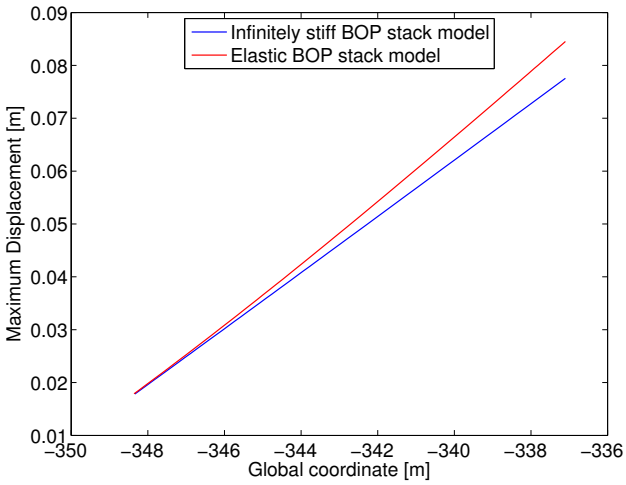

Figure 8.9: BOP Maximum Displacement

8.3 Fatigue Damage Assessment

The fatigue damage assessment was carried out using Matlab. Moment-time series for all global response analyses for all studies were post processed in Matlab. The amount of calculated data is comprehensive, thus only selected plots and tables are presented in the following section and in the appendices.

8.3.1 Mapping of Load-to-time Series

Moment-time series from the wellhead datum were imported from Riflex to Matlab. The first 100 seconds of the series were omitted to remove the influence of transient effects. The result is one hour moment-time series. A selected plot is shown in figure 8.10. Further the mapping algorithm produced stress-time series. Before counting the stress

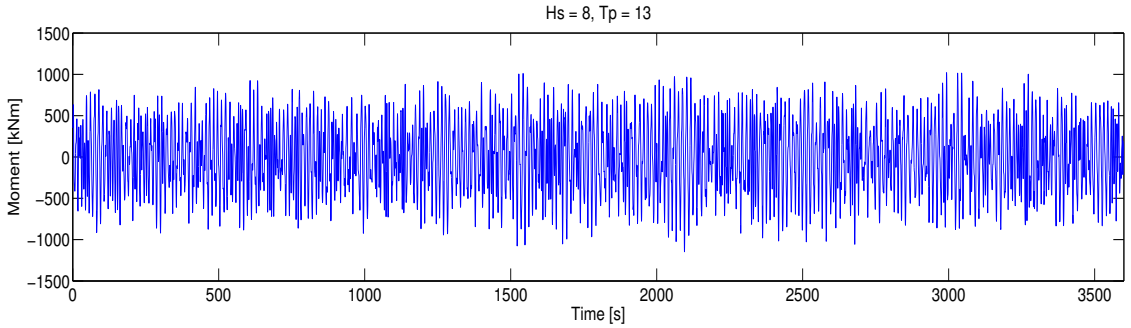

Figure 8.10: Moment-time series (transient effects are omitted)

cycles, an establishment of turning points was conducted. The stress-time series were plotted with markers at the turning points to enable a visual validation, an example is shown in figure 8.11. Turning points acts as input to the rainflow counting procedure.

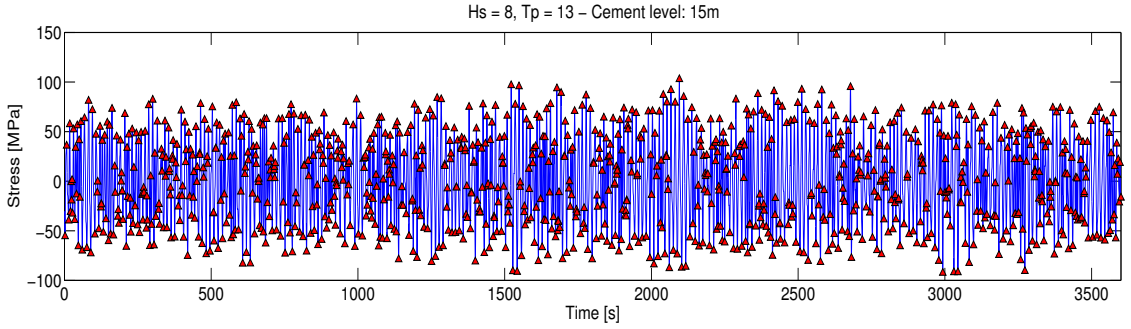

Figure 8.11: Turning points, $H_s = 8$ m, $T_p = 13$ s

8.3.2 Cycle Counting

The rainflow cycle counting was carried out using WAFO functions in Matlab. Output from the counting procedure is given in terms of whole cycles and half cycles. Half and whole cycles were gathered in stress range histograms to simplify the further calculations. The development of stress range histograms was done by putting different stress ranges in bins and assigning the bins with a value reflecting the number of stress ranges within. The size of the bins were set to 1 MPa, e.g. a stress range of $\Delta\sigma = 21.8$ MPa would be put in bin that contains stress ranges from $\Delta\sigma = 21.5$ MPa to $\Delta\sigma = 22.4$ MPa.

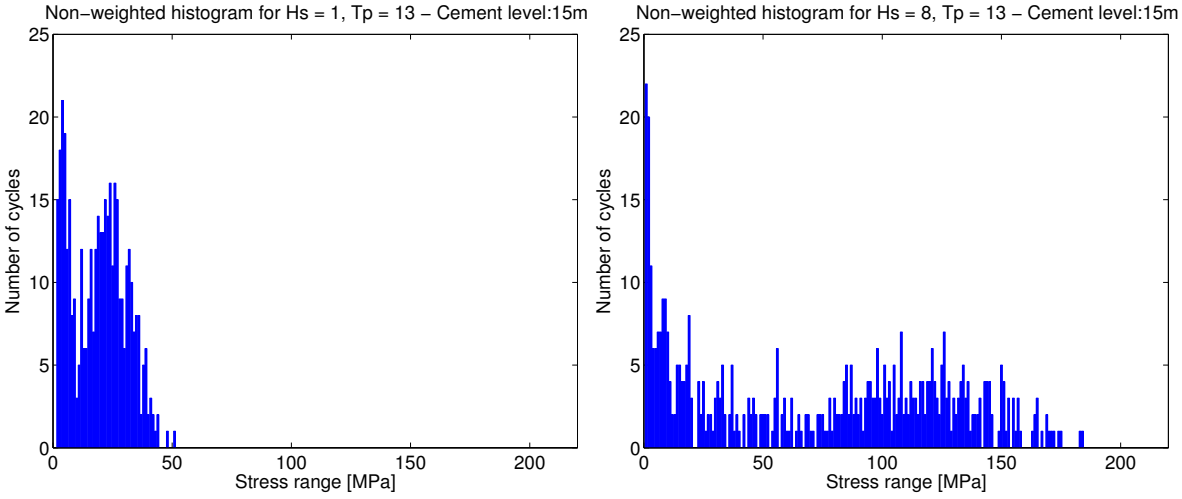

(a) (b)

Figure 8.12: Stress range histograms - Elastic BOP model

Two selected histograms are presented in figure 8.12, both resulting from one hour global response analyses. The difference in terms of stress range distribution between the two sea states is justified by the significant wave height. The excitation loads in a sea state where $H_s = 8$ m are significantly larger than the excitation loads in a sea state where $H_s = 1$ m, thus giving rise to larger stress ranges in plot (b).

8.3.3 Wellhead Fatigue Damage - Main Study

The main objective in this thesis was to investigate the effects of implementing improved BOP stack stiffness properties in the global response analyses with respect to estimated fatigue damage. The fatigue damage is presented as a fraction of one, where one, in compliance with the Palmgren-Miner rule, represents collapse. The fatigue damage for

the two BOP stack models are shown in table 8.4. In this table the fatigue damage is presented in terms of significant wave height and cement level. The damage from each H_s is a result from global response analyses carried out with all sea states in the H_s block. A H_s block contains all the corresponding spectral peak periods from the applied scatter diagram. The table also includes the estimated total weighted fatigue damage for a one hour drilling operation and the percentual difference in fatigue damage between the two BOP stack models. It is noted that difference in terms of estimated fatigue damage imposed by the two BOP stack models is small.

H_s	BOP	Cement level [m]							
[m]	Model	0	2	5	10	15	20	25	
1	Elastic	0.0308	0.0266	0.0226	0.0551	0.0386	0.0274	0.0148	$[10^{-4}]$
	Inf. stiff	0.0302	0.0259	0.0220	0.0545	0.0379	0.0269	0.0146	
2	Elastic	0.7912	0.8191	0.7005	1.0436	0.8751	0.7458	0.5319	$[10^{-4}]$
	Inf. stiff	0.7931	0.8164	0.6944	1.0439	0.8745	0.7459	0.5295	
3	Elastic	1.0886	1.3391	1.0237	1.3504	1.1885	1.0305	0.8120	$[10^{-4}]$
	Inf. stiff	1.0819	1.3252	1.0182	1.3482	1.1829	1.0258	0.8017	
4	Elastic	0.8402	1.1357	0.7973	1.0208	0.9051	0.7829	0.6265	$[10^{-4}]$
	Inf. stiff	0.8381	1.1301	0.7923	1.0209	0.8993	0.7798	0.6231	
5	Elastic	0.5909	0.8206	0.5485	0.6904	0.6176	0.5380	0.4232	$[10^{-4}]$
	Inf. stiff	0.5867	0.8170	0.5475	0.6856	0.6152	0.5351	0.4242	
6	Elastic	0.3685	0.5180	0.3273	0.4149	0.3742	0.3240	0.2512	$[10^{-4}]$
	Inf. stiff	0.3662	0.5171	0.3277	0.4144	0.3731	0.3231	0.2513	
7	Elastic	0.2096	0.2958	0.1748	0.2327	0.2081	0.1763	0.1353	$[10^{-4}]$
	Inf. stiff	0.2097	0.2959	0.1748	0.2327	0.2078	0.1760	0.1354	
8	Elastic	0.1121	0.1522	0.0880	0.1180	0.1068	0.0899	0.0668	$[10^{-4}]$
	Inf. stiff	0.1135	0.1541	0.0888	0.1189	0.1077	0.0906	0.0674	
Total	Elastic	4.0318	5.1071	3.6826	4.9259	4.3139	3.7147	2.8618	$[10^{-4}]$
	Inf. stiff	4.0193	5.0817	3.6656	4.9190	4.2984	3.7032	2.8473	
Percentual difference		0.3094	0.4975	0.4612	0.1402	0.3604	0.3087	0.5077	[%]

Table 8.4: One hour fatigue damage for all T_p within all H_s at different cement levels

The fatigue damage estimates presented in table 8.4 were calculated by weighting the fatigue damage from each individual sea state. To validate these estimates, another approach was carried out. The stress range histograms were weighted before application

of the Palmgren-Miner summation. The result is one histogram which contains weighted stress cycles for all sea states, for each BOP stack model, for each study. Figure 8.13 represents such histograms from the main study, cement level: 15 m. The histograms

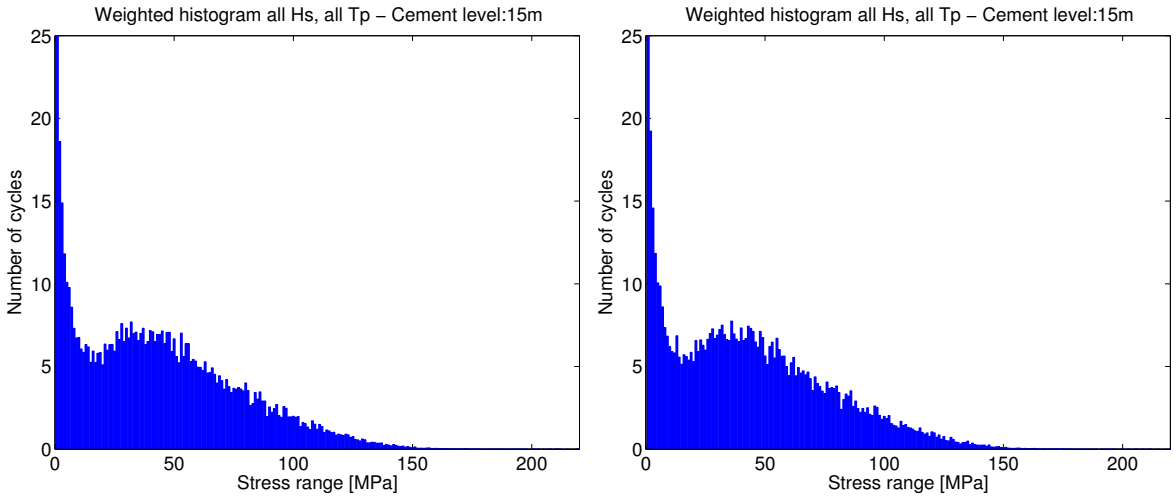

(a) Elastic BOP (b) Infinitely stiff BOP

Figure 8.13: Weighted stress range histograms for all sea states

shows a close resemblance in terms of stress range distribution and only a slight difference between the two models is seen visually. The alternative approach yielded the same fatigue estimates as the original one. Further the estimated fatigue damage will be presented in fatigue life which is given in days, see equation 7.5. This is done to give a more legibly presentation compared to presentation in the fatigue damage format. Estimated fatigue life of the wellhead for the two BOP stack models is shown in figure 8.14. From table 8.4 it is seen that, regardless of cement level, the elastic BOP stack

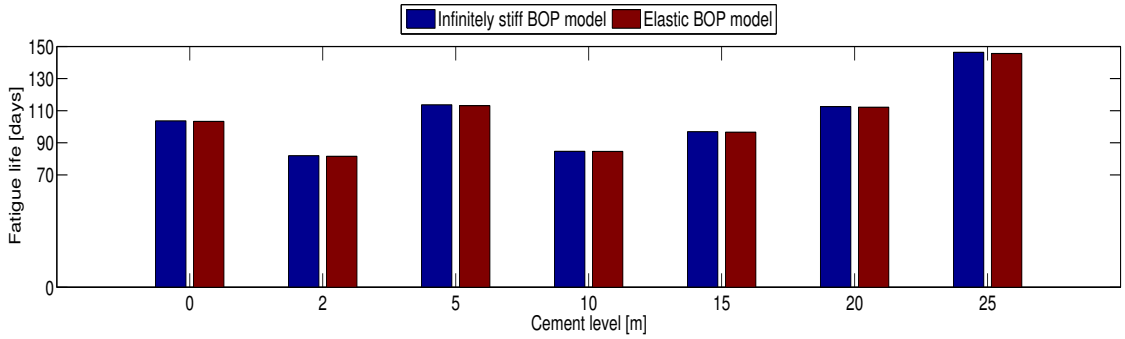

Figure 8.14: Fatigue life [days] - Main study

model imposes the largest total fatigue damage to the wellhead. Hence, the result is

opposite of what was expected. This is though not always the case for each individual sea state, e.g for sea states with $H_s = 8$ m; here the infinitely stiff BOP stack model imposes the largest fatigue damage. This is also seen for some cement levels for $H_s = 7$ m. In other words, larger excitation loads contribute more to the estimated fatigue damage imposed by the infinitely stiff BOP stack model compared to the elastic BOP stack model The authors believe that there are mainly two factors that affects the difference in estimate fatigue damage imposed by the two BOP stack models.

Firstly an assumption was that the infinitely stiff BOP stack model would impose larger estimated fatigue damage to the wellhead compared to the elastic BOP stack model. The assumption is justified by the basic rule of mechanics that larger stiffness should give larger moments in the BOP and thus larger estimated fatigue damage in the wellhead. The formula for bending moment of a beam as a function of second moment of area, Young's modulus and curvature reads:

$$M = -EI \frac{\partial^2 w}{\partial x^2} \tag{8.1}$$

As seen in the formula, larger bending stiffness EI yields larger moment, M.

Secondly, an assumption was that the BOP stack's dynamic behaviour would contribute more to the estimated fatigue damage in the wellhead imposed by the elastic BOP stack model compared to the infinitely stiff BOP stack model. This assumption is justified by the contribution from the BOP stack's significant mass properties. The influence from dynamic mass contributions are assumed to be large if any motion in the BOP stack is present. Further it is known that the displacement characteristics of the BOP stack is directly connected to the structural stiffness. Hence, a less stiff BOP stack will, in principle, experience larger displacements than a stiffer BOP stack. Larger displacements imply larger motions and thus larger dynamic mass contributions. Righting moments in the BOP stack and wellhead will try to counteract this motion, and thus giving contributions to stresses in the hot spot. These assumptions imply that the elastic BOP stack will experience larger motions than the infinitely stiff BOP. The relative impact on the estimated fatigue damage in the wellhead from larger BOP stack motions may be most significant when relatively small excitation forces are present. This is justified by an assumption that the infinitely stiff BOP stack will experience close to zero motions when relatively small loads are present. It is also assumed that the motions of the elastic BOP stack is large enough to make dynamic mass contributions significant

when relatively small loads are present.

To investigate the second assumption, the displacement in the lower flex joint was examined. The investigation was carried out by conducting global response analyses for both global models. Global response analyses were conducted in Riflex for all H_s at $T_p = 9$ seconds. The result is presented in terms of mean displacement from displacement-timer series of one hour, see figure 8.15. It is seen that the mean displacement

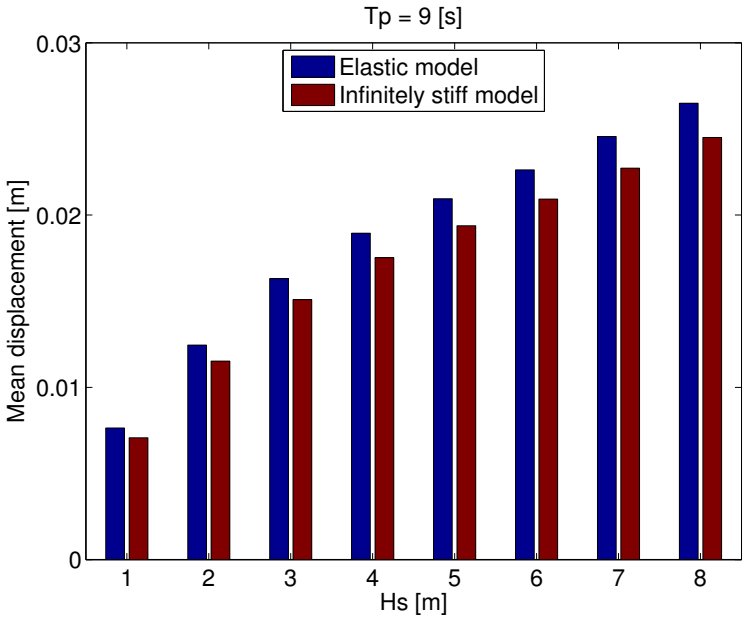

Figure 8.15: Mean displacement at lower flex joint for all H_s and $T_p = 9$. Non-linear flex joint stiffness

is roughly 7.5% greater for the case with elastic BOP stack model compared to the case with infinitely stiff BOP stack model. See table D.1 for complete listing. According to the second assumption, larger displacement should impose larger fatigue damage in the wellhead. However, the weighted fatigue damage estimates from $H_s = 8$m, listed in table 8.4, indicate that the infinitely stiff BOP stack imposes the largest fatigue damage in the wellhead. This means that the first assumption is most governing for high excitation loads.

The total weighted fatigue damage estimates in table 8.4 indicate that the elastic BOP model imposes the largest fatigue damage. Hence, the second assumption is considered to be the most governing. It is though noted, as mentioned earlier, that the difference in terms of estimated fatigue damage imposed by the two BOP stack models is small.

8.4 Results - parameter and sensitivity study

8.4.1 Parameter study #1 - Current

In a fatigue assessment it is considered conservative to omit current. By including current in global response analyses, the hydrodynamical damping on the MODU and riser will increase. This will decrease the dynamic loading on the wellhead and thus decrease the fatigue damage in hot spots. This parameter study confirms this statement. The rainflow counting of the stress-time series is presented as weighted histograms of

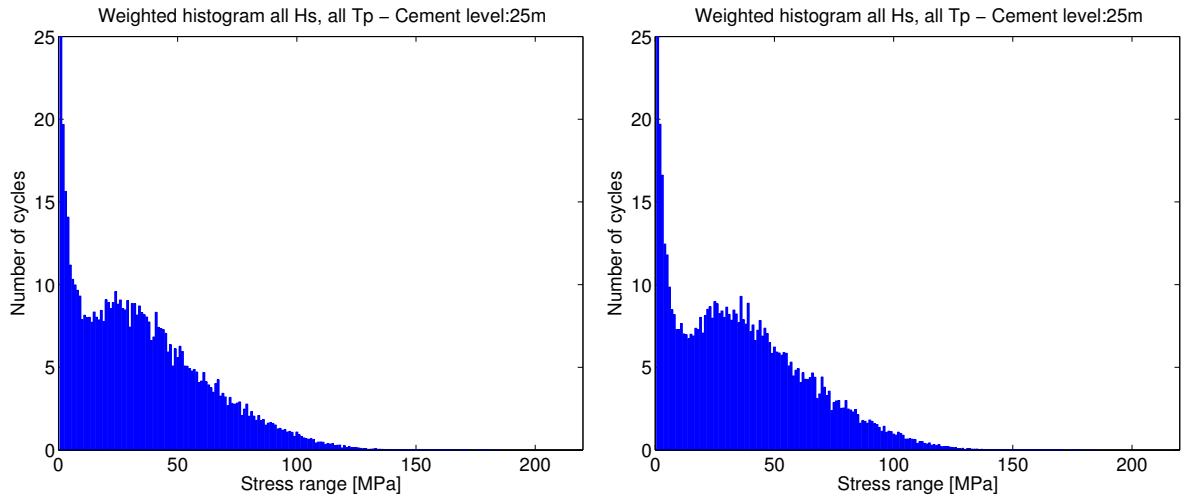

(a) Elastic BOP - Current

(b) Elastic BOP - No current

Figure 8.16: Weighted stress histograms for elastic BOP model with and without current

stress ranges for a cement level of 25 meter. Figure 8.16 shows weighted stress range histograms with and without current for the elastic BOP stack model. Visually, it is hard to spot the difference between the two histograms in. However, the average stress range is 36.1 MPa with current and 38 MPa without current. The impact from the inclusion of current is an increased fatigue life by 9.5 to 11.5 percent, depending on the cement level, see figure 8.17. The estimated fatigue life for all cement levels are summarized in table 8.5. Like the main study, the difference in terms of estimated fatigue life between the two BOP stack models is in the vicinity of 0 to 0.5 percent.

The applied current profile for this parameter study is considered to be of a small magnitude. It can be argued that if the magnitude of the applied current profile is increased, then fatigue life will also increase. This emphasizes the conservativeness of analyses that are run with absence of current.

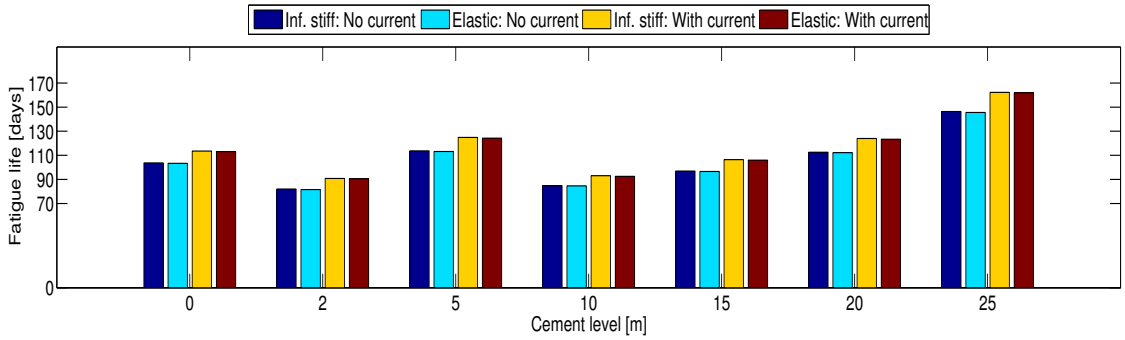

Figure 8.17: Fatigue life [days] - Parameter study #1 - Current

Cement	No current		Current included	
level [m]	Inf. model	Elastic model	Inf. model	Elastic model
0	103.67	103.35	113.51	113.12
2	81.99	81.59	90.79	90.51
5	113.67	113.14	124.87	124.27
10	84.71	84.59	93.02	92.50
15	96.94	96.59	106.41	105.94
20	112.52	112.17	124.02	123.34
25	146.34	145.60	162.28	161.96

Table 8.5: Fatigue life [days] - Parameter study #1 - Current

8.4.2 Parameter study #2 - Global structural damping factor

In the main study global response analyses were conducted with global structural damping factor $\alpha = 0.02$. In previous studies done by Reinås *et al.* [9] and Russo *et al.* [12], analyses have been conducted with $\alpha = 0.01$. Reducing the structural damping factor reduces the overall damping in the drilling system and should lead to a decrease in estimated fatigue life of the wellhead system. Reducing the structural damping factor

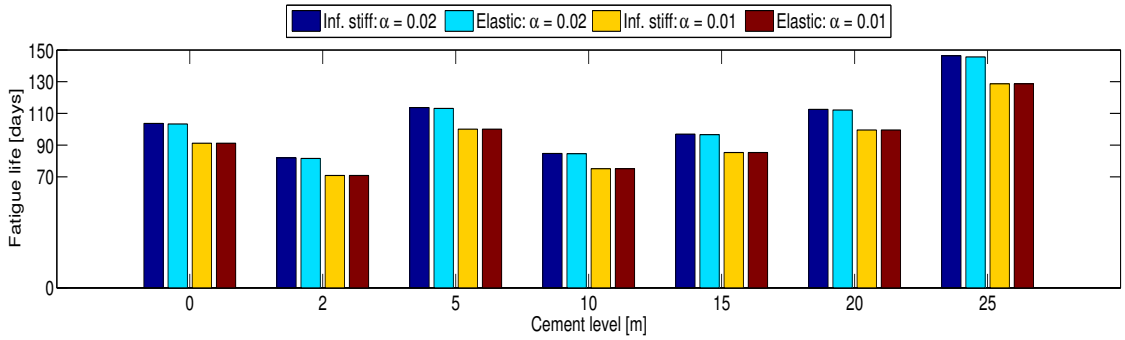

Figure 8.18: Fatigue life [days] - Parameter study #2 - Global damping factor

has no significant effect on the difference, in terms of estimated fatigue life, between the elastic BOP stack model and the infinitely stiff BOP stack model. The difference is shown in table 8.6. The difference in estimated fatigue life between the two BOP stack models is between 0 to 1 percent. However, compared to the analyses where $\alpha = 0.02$, a decrease in fatigue life by 19 to 21 percent is observed. Increased damping factor corresponds to reduced conservatism in regards to wellhead fatigue estimates. Figure

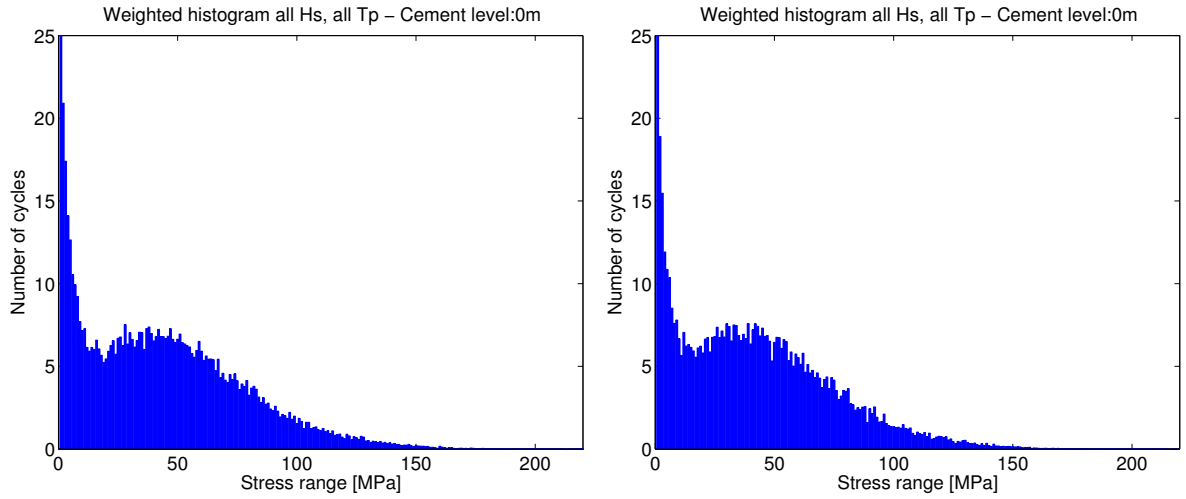

(a) Elastic BOP - $\alpha = 0.01$ (b) Elastic BOP - $\alpha = 0.02$

Figure 8.19: Weighted stress histograms, elastic BOP model with $\alpha = 0.01$ and $\alpha = 0.02$

8.19 shows weighted stress range histograms with structural damping factor $\alpha = 0.01$ and $\alpha = 0.02$ for the elastic BOP stack model. For $\alpha = 0.01$ there is a higher number of stress cycles with higher stress ranges than for $\alpha = 0.02$. The reduced fatigue life for $\alpha = 0.01$ is also reflected in the average stress range which is 43.2 MPa compared to 36.1 MPa for $\alpha = 0.02$. The study is summarized for all cement levels in table 8.6.

Cement	$\alpha = 0.02$		$\alpha = 0.01$	
level [m]	Inf. model	Elastic model	Inf. model	Elastic model
0	103.67	103.35	91.19	91.19
2	81.99	81.59	70.84	70.84
5	113.67	113.14	100.08	100.08
10	84.71	84.59	75.13	75.13
15	96.94	96.59	85.31	85.31
20	112.52	112.17	99.55	99.55
25	146.34	145.60	128.71	128.71

Table 8.6: Fatigue life [days] - Parameter study #2 - Global damping factor

8.4.3 Parameter study #3 - Lower flex joint stiffness

This parameter study was conducted in order to assess the estimated fatigue damage when lower flex joint stiffness characteristics change. The flex joint stiffness is changed from non-linear to linear. The linearisation was carried out with basis in the stiffness corresponding to a deflection of 10 degrees. The values were sampled from the non-linear stiffness, see table C.8. This yielded a linear stiffness of 93 $^{\mathrm{kN\,m}}/_{\mathrm{deg}}$. The estimated fatigue life for all cement levels and for both BOP stack models are summarized in table 8.7.

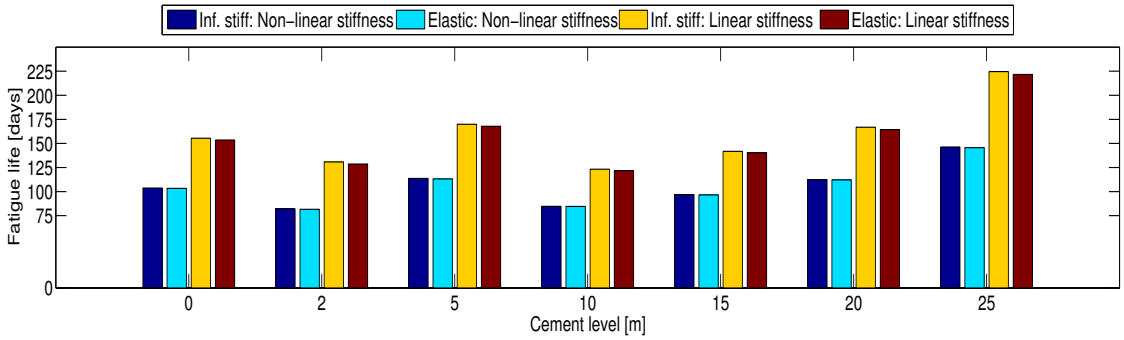

Figure 8.20: Fatigue life [days] - Parameter study #3 - Lower flex joint stiffness

Cement	Non-linear stiffness		Linear stiffness	
level [m]	Inf. model	Elastic model	Inf. model	Elastic model
0	103.67	103.35	155.41	153.55
2	81.99	81.59	130.79	128.67
5	113.67	113.14	169.87	167.83
10	84.71	84.59	123.23	121.69
15	96.94	96.59	141.81	140.26
20	112.52	112.17	166.85	164.41
25	146.34	145.60	224.59	221.58

Table 8.7: Fatigue life [days] - Parameter study #3 - Lower flex joint stiffness

For the case with linear flex joint stiffness, the difference in fatigue life between the infinitely stiff BOP stack model and the elastic BOP stack model lies between 0.9 to 1.2 percent. The infinitely BOP stack model imposes a slightly longer fatigue life. This is seen in figure 8.20. For the case with non-linear flex joint stiffness, the difference in estimated fatigue life lies between 0.1 to 0.5 percent.

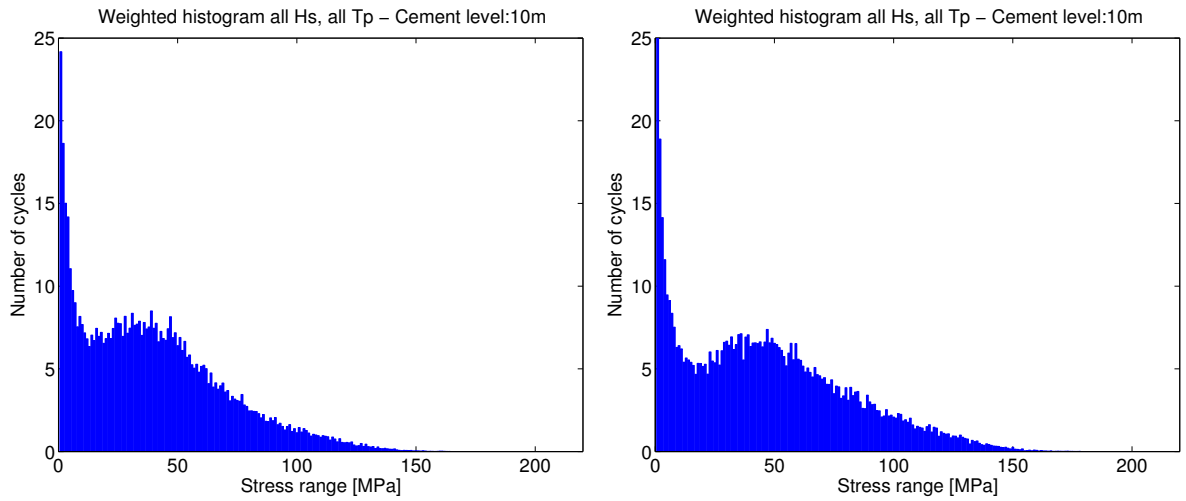

(a) Elastic BOP - Linear flexjoint stiffness (b) Elastic BOP - Non-linear flexjoint stiffness

Figure 8.21: Weighted stress histograms for elastic BOP model with linear and non-linear flex joint stiffness

Figure 8.21 shows weighted stress range histograms with linear and non-linear lower flex joint stiffness for the elastic BOP stack model. It can be seen that the linear flex joint stiffness gives a higher concentration of stress cycles around stress ranges below 50 MPa than what is the case with non-linear stiffness. For this cement level, the average stress range is 41.5 MPa for linear flex joint stiffness and 48.3 MPa for non-linear flex joint stiffness.

Application of linear flex joint stiffness instead of non-linear stiffness gives an overall increase in estimated fatigue life by 32 to 39 percent depending on the cement level. This coincides well with the finding that Williams and Greene [10] made. They concluded that application of non-linear stiffness gave a reduction in fatigue life of approximately 30 percent.

In the discussion of the main study, it was concluded that the estimated fatigue damage imposed by infinitely stiff BOP model was larger compared to the elastic BOP model for some cement levels at $H_s = 7$m and for all cement levels at $H_s = 8$m. It is of interest to see if this is still the case when the lower flex joint stiffness is linear. The damage from each H_s is a result from global response analyses carried out with all sea states in the H_s block. A H_s block contains all the corresponding spectral peak periods from the applied scatter diagram. The same mean displacement analysis that was conducted for the main study was also carried out for this study. The results are shown in figure 8.22.

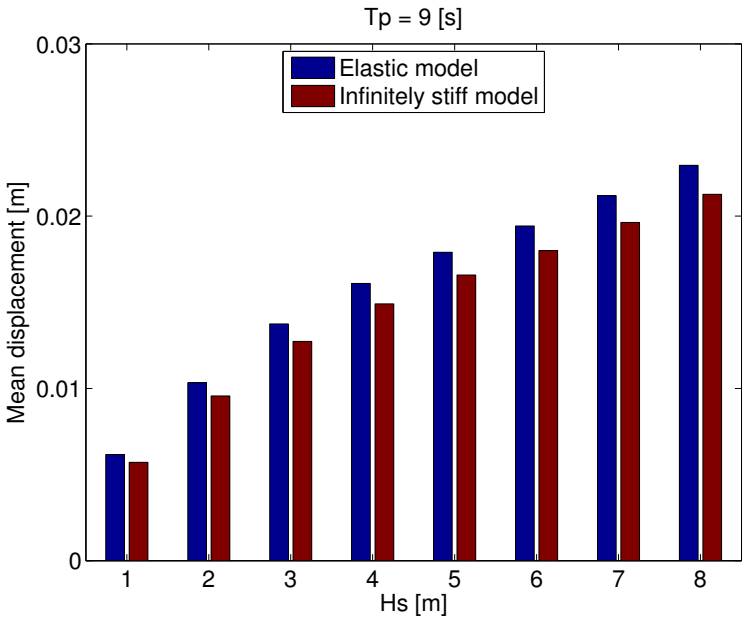

Figure 8.22: Mean displacement at lower flex joint for all H_s and $T_p = 9$. Linear flex joint stiffness

The mean displacement is roughly 7.3% greater for the elastic BOP stack model compared to the infinitely stiff BOP stack model, see table D.2 for complete listing. This is approximately the same as what was found when the stiffness of the lower flex joint was non-linear. From these two observations, it is reasonable to believe that the difference, in terms of estimated fatigue damage, between the two BOP stack models should be the same as for the main study. By this it is meant that the estimated fatigue damage imposed by the infinitely stiff BOP stack model should be larger for some cement levels at $H_s = 7$m and for all cement levels at $H_s = 8$m, as in the main study. However, this is not the case. The estimated fatigue damage imposed by the elastic BOP stack model is consistently greater for all cement levels as well as for all H_s blocks. See table 8.8 where only $H_s = 6$m to $H_s = 8$m is included. There may be coincidences that cause this result, but it might be of interest to investigate the matter further. However, this is not a part of this thesis.

8.4.4 Sensitivity study - Bending stiffness

In this sensitivity study, the bending stiffness in two sections of the elastic BOP stack model was altered. These are the sections describing the LMRP connector and the

H_s [m]	BOP Model	Cement level [m] 0	2	5	10	15	20	25	
6	Elastic	0.2624	0.3628	0.2455	0.3110	0.2775	0.2421	0.1905	$[10^{-4}]$
	Inf. stiff	0.2597	0.3585	0.2438	0.3075	0.2746	0.2393	0.1892	
7	Elastic	0.1504	0.2121	0.1346	0.1725	0.1544	0.1332	0.1040	$[10^{-4}]$
	Inf. stiff	0.1491	0.2101	0.1338	0.1718	0.1534	0.1322	0.1037	
8	Elastic	0.0800	0.1121	0.0679	0.0885	0.0793	0.0679	0.0524	$[10^{-4}]$
	Inf. stiff	0.0795	0.1115	0.0675	0.0881	0.0788	0.0676	0.0522	

Table 8.8: One hour fatigue damage for all T_p within $H_s = 6$m to $H_s = 8$m at different cement levels. Linear flex joint stiffness

wellhead connector. See table C.5 for the original setup of the elastic BOP stack model. The LMRP connector is section 5 and the wellhead connector is section 2 in the aforementioned table. The following variations in bending stiffness were applied: $1 \times 10^8\,\mathrm{N\,m^2}$ and $5 \times 10^8\,\mathrm{N\,m^2}$, $1 \times 10^9\,\mathrm{N\,m^2}$ and $5 \times 10^9\,\mathrm{N\,m^2}$ and finally $1 \times 10^{10}\,\mathrm{N\,m^2}$ and $5 \times 10^{10}\,\mathrm{N\,m^2}$. The study is summarized in terms of estimated fatigue life in table 8.9. The first variation in bending stiffness that imposes a larger estimated fatigue life, compared to the original setup, is marked with bold entry in this table.

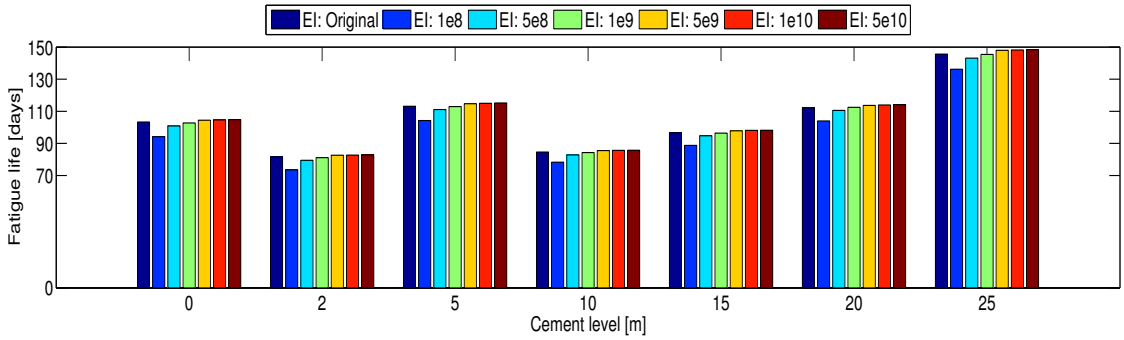

Figure 8.23: Fatigue life [days] - Sensitivity study - Bending stiffness

It was initially assumed that the stiffness of the LMRP connector and wellhead connector in the 3D element BOP stack model was too high. This is due to the fact that the connectors are modelled in solid steel. It is seen from figure 8.23 that the estimated fatigue life decreases if the bending stiffness is $5 \times 10^8\ \mathrm{N\,m^2}$ or less. It is also seen that bending stiffness above $5 \times 10^9\ \mathrm{N\,m^2}$ does not have a significant effect on the estimated fatigue life.

If the bending stiffness in the connectors is increased to $5 \times 10^9\,\mathrm{N\,m^2}$, the estimated fatigue life is longer compared to the original connector stiffness setup. This stiffness,

Cement level [m]	Bending stiffness [N m^2]						
	Original	1×10^8	5×10^8	1×10^9	5×10^9	1×10^{10}	5×10^{10}
0	103.35	94.15	100.87	102.73	**104.47**	104.63	104.84
2	81.59	73.46	79.47	81.12	**82.64**	82.73	82.86
5	113.14	104.24	111.12	112.95	**114.75**	115.01	115.21
10	84.58	78.29	82.84	84.31	**85.52**	85.65	85.76
15	96.59	88.77	94.75	96.41	**97.88**	98.12	98.20
20	112.17	104.01	110.56	**112.49**	113.66	113.94	114.10
25	145.60	136.17	143.12	145.41	**147.97**	148.16	148.44

Table 8.9: Fatigue life [days] - Sensitivity study - Bending stiffness

5×10^9 N m^2, is greater than the original stiffness setup. As mentioned, the stiffness in the connectors in the 3D element BOP stack model may be too stiff due to low detail modelling. Hence, it can be speculated that the estimated fatigue life which is calculated for the elastic BOP model in the main study should be lower, to some degree. If this is the case, the difference, in terms of estimated fatigue life, between the two BOP stack models would be larger.

8.5 Uncertainties and Assumptions

This section contains identification and evaluation of assumptions and uncertainties relevant for this thesis. A distinction is made between the factors that may influence *the magnitude* of the estimated fatigue damage and the factors that may influence *the relative differences* in terms of estimated fatigue damage between the two BOP stack models.

8.5.1 Factors affecting the magnitude of estimated fatigue damage

The large extent of wellhead fatigue methodologies involves numerous uncertainties and assumptions. To evaluate the estimated fatigue damage, it is important to assess the factors which can impose inaccurate estimates. Errors can accumulate if uncertainties are present in multiple parts of the analyses. Consequently, the final estimated fatigue damage can comprise significant deviation from realistic values.

Probabilistic environmental loading

The environment which is introduced in the global response analyses is based on statistics. This serves as an uncertainty in relation to which environmental conditions the drilling system will be exposed to in the future. The scatter diagram which is applied contains statistics from the northern north sea. To reduce the uncertainty, scatter diagrams which is developed in the area where the drilling system is expected to operate, could be applied.

RAO characteristics

The RAOs describe the relation between the load on the MODU and the response of the MODU. It was established that the RAOs are of first order, i.e. no hydrodynamical higher order effects are captured. This simplification affects the response of the system.

Calculation of response using finite element method

The finite element method gives, if applied correctly, a good representation of a structure's response to loading. Nevertheless it is important to keep in mind that the method is approximate and that factors like element type, number of elements, representation of non-linearities etc. are important in regards to accuracy.

The global model consists of the drilling system modelled with beam elements. A more accurate model could be represented by modelling the drilling system with cubic 3D elements. This would though impose severe CPU time and is thus not a relevant technique for this kind of analyses.

Modelling of the wellhead system

The wellhead system comprises different pipes and component that interact with each other and with the surrounding soil. These phenomena are represented in a beam model of the wellhead system as described in 6.1.3. Uncertainties are related to this simplification.

Soil damping in the studies carried out in this thesis was omitted. Damping in the soil may be implemented in the spring attached to the wellhead beam model if applicable data is available.

Fatigue damage estimation by Palmgren-Miner summation

The fatigue damage estimations were carried out using Palmgren-Miner summation and SN curves. The SN curves were gathered from DNV-RP-C203 and is developed by specimen testing. The curves are based on subtracting two standard deviations from the curve which is developed by specimen testing [31]. This results in conservative fatigue damage estimates. The SN curves are developed on the basis of constant amplitude loading. Hence, a Haibach extrapolation is applied to take variable amplitude loading into account. The accuracy of this representation is considered an uncertainty.

The Palmgren-Miner summation does not take into account the order of when the different stresses occur [66]. Hence, the possible effects of the order of the loading in the time series is not accounted for.

Effective cement level

Uncertainties are related to effective cement level between the 30″ conductor and the 20″ surface casing. With effective cement level it is meant the goodness of the connection between the casings and cement. To account for this uncertainty, different load-to-stress tables were provided for different cement levels. If conservatism is desirable, the cement levels which represents the highest fatigue life should be used.

Safety factor

Common procedure to account for assumptions and uncertainties is to multiply the final fatigue damage or fatigue life with a risk factor or a design fatigue factor. In the statement ”Wellhead Fatigue Analysis Method” [3] DNV applies a design fatigue factor of 10 to account for both uncertainties and consequences of failure. The possibility for inspection of the hot spots is also incorporated in the factor. A design factor of 10 would impose conservative fatigue estimates but it is justified by the significance of the potential consequences of failure.

8.5.2 Factors affecting the goodness of the elastic BOP stack model

This section addresses the uncertainties and assumptions that may affect the percentual difference between the elastic BOP stack model and the infinitely stiff BOP stack model with respect to estimated fatigue damage. The uncertainties and assumptions are highly relevant in relation to how these differences are interpreted and evaluated.

Identification of displacement curves in the calibration procedure

The calibration procedure on the elastic BOP stack model involved a comparison between the displacement of the 3D element BOP stack model and the elastic BOP stack model. The calibration was based on a visual evaluation of displacement plots. This may impose inaccuracies in the resulting stiffness.

Low-detail connector modelling

The 3D element model of the BOP stack that was provided consisted of connectors modelled in solid steel. For better accuracy, the connector should be modelled in full detail including bolts, interactions etc.

Mass properties of the BOP stack

An actual BOP stack is fitted with modules to the body. These modules are not modelled in the provided 3D element BOP stack model. Hence, it is reasonable to assume that the BOP stack applied in the global analyses is too light.

Assumption of linear displacement in each node

The assumption of linear displacement in each node is the basis for the calibration procedure. The assumption was partially validated by comparing the displacement fields of the two Abaqus models when exposed to load patterns from two additional sea states. Nevertheless should, ideally, even more applicable load patterns be analysed to ensure that the stiffness is linear with respect to loading.

However, if the stiffness of the BOP stack is non-linear with respect to loading, a problem in relation to representation of the BOP stack as beam elements would rise. This non-linear behaviour can not be reproduced in Riflex using the method presented in this thesis.

The low-detail connector modelling is considered as the largest uncertainty of the above. The bending stiffness study was conducted to evaluate the sensitivity of the uncertainty and thus giving basis to evaluation of the results.

Chapter 9

Summary and Conclusion

9.1 Summary of Results

A summary of the main results is given in this section. Estimated fatigue damage estimates presented in table 9.2 and 9.1 are calculated using a load-stress curve that corresponds to a 25 m cement level.

	Cement level: 25 m		
Case	Inf. model	Elastic model	% difference
Main study	146.34	145.60	0.51
Param. study #1 - Current	162.28	161.96	0.20
Param. study #2 - Damping factor	128.71	128.12	0.46
Param. study #3 - Lower flex joint stiffness	224.59	221.58	1.34

Table 9.1: Summary of results - Fatigue life [days]

Table 9.1 contains the main results from the fatigue damage assessments conducted in this thesis. Fatigue life estimates are based on a drilling operation with only one phase. The fatigue estimates are still given as fatigue life to give a more legibly presentation compared to presentation in the fatigue damage format.

The sensitivity of the LMRP- and wellhead connector stiffness is an important factor. This is due to the uncertainty of how well the properties of the connectors is represented in the 3D element BOP stack model.

Bending stiffness [N m^2] - Cement level: 25 m						
Original	1×10^8	5×10^8	1×10^9	5×10^9	1×10^{10}	5×10^{10}
146.34	136.17	143.12	145.41	147.97	148.16	148.44

Table 9.2: Summary of results - Fatigue life [days] - Sensitivity study

9.2 Conclusion

Current methods for estimating fatigue damage in subsea wellhead systems are proven to be overly conservative in comparison with full scale measurement [12]. A proper representation of the structural properties of the BOP stack in global response analyses has been identified as one of the shortcomings of today's methods. The main objective of this thesis was thus to investigate the effects of improved BOP stack modelling on fatigue damage estimates.

Difference, in terms of estimated fatigue damage, imposed by the two BOP stack models

The results from the wellhead fatigue assessments that were carried out in this thesis conclude that the elastic BOP stack model imposes the greatest estimated fatigue damage in the wellhead. This conclusion is valid independent of effective cement level. The difference, in terms of estimated fatigue damage, imposed by the two BOP models is, at maximum, 0.51 % for the main study. The largest difference observed in the parameter studies was 1.34 %. Hence, it is concluded that the effects of improved BOP stack modelling in a global response analysis, is not significant.

Evaluation of estimated fatigue damage

The fatigue assessment carried out in this thesis resulted in relatively large fatigue damage estimates. This corresponds to a short fatigue life. In a study by Reinås *et al.* [9], fatigue life in a wellhead in the range of 550 to 800 days was estimated. Williams and Greene [10], estimate the fatigue life of a wellhead to be in the vicinity of 1000 days. These values for estimated fatigue life are significantly greater than what were estimated in this thesis. Hence, the values for fatigue life estimated in this thesis are considered to

be too short. The error is connected to the number of uncertainties that are present in the analyses. In addition is only one phase of a drilling operation analysed. Although the magnitude of estimated fatigue life is considered to be too short, the values of percentual difference imposed by the two BOP stack models are considered to be adequate.

Chapter 10

Recommendations for Further Work

There are uncertainties related to the modelling of LMRP and wellhead connectors in the 3D element BOP stack model. To validate the influence of improved BOP stack modelling, a 3D element model with detailed representation of the connectors should be investigated.

In the conclusion it was emphasized that the effects of improved BOP stack modelling on estimated wellhead fatigue damage were insignificant. If it is still desirable to account for improved BOP stack modelling, we propose two methods:

- ◇ Incorporating the effects of improved BOP stack modelling in a risk factor or design factor. This method would not impose any extra modelling or CPU time. Nevertheless, it will be necessary to conduct a thorough investigation of the effects of the stiffness correction. If the effects of improved BOP stack modelling should be incorporated in a risk factor, it is important that there is a consistency in these effects. If this is validated, the effects of improved BOP stack modelling may be described as a given fraction of the estimated fatigue life.
- ◇ Quantification of stiffness properties of a 3D element BOP stack model as done in this thesis. Subsequently the stiffness properties should be implemented in the global response analysis. An alternative method to the calibration procedure may be to develop formulas for the BOP stack stiffness. These formulas can be functions of obtainable load-displacement relationships. This method would result in a more accurate modelling of the BOP stack in global response analysis, but involve an extension of already extensive analyses.

Russo *et al.* [12] address fatigue assessments based on measured riser loads. The paper indicates that measured loads may be applied to validate analytical methods. A suggestion for further work comprises hence of conducting measurements, e.g. by application of strain gauges, near the wellhead datum. Measured loads may be calculated

from the strain histories and compared with loads obtained from global analytical response analyses. The difference may be accounted for by a correction factor inherent to global response analyses. This would decrease the overall uncertainty in analytical fatigue assessments. Since the measurements are gathered below the main body of the BOP, effects from BOP stack elasticity would be accounted for in such a factor. The measured data may also be applied as a frame of reference when improving analytical methods for estimation of wellhead fatigue.

In this thesis the upper boundary of the drilling operation window was set to $H_s = 8$m. It is reasonable to assume that larger sea states could occur and impose larger loads to the drilling system and thus to the BOP stack. This can happen if the drilling system is not disconnected from the BOP in time. Hence, local plastic deformations in the BOP stack may occur. This will alter the BOP stack's stiffness properties. This change in stiffness properties should be re-assessed in a wellhead fatigue context. Global response analyses are unable to predict local yielding in the BOP stack. This implies that an investigation of this/these plastic deformation(s) must be conducted in a local FEM model.

Bibliography

[1] F. Robelius, *Giant oil fields-the highway to oil: GIant oil fields and their importance for future oil production*. PhD thesis, Uppsala University, 2007. 1

[2] DNV, "Offshore Update - News From DNV To The Offshore Industry," pp. 34–37, February 2012. 1

[3] T. Hørte, M. Istad Lem, and G. Grytøyr, "Wellhead fatigue analysis method," DNV, 2011. 1, 2, 22, 32, 45, 63, 65, 67, 69, 70, 71, 72, 87, 89, 95, 123, I, XXIV, XXXIX

[4] M. Sæther, L. Reinås, and J. Svensson, "Wellhead fatigue analysis method: A new boundary condition modelling of lateral cement support in local wellhead models," *ASME Conference Proceedings*, no. OMAE2012-83049, 2012. 2, 5, 91

[5] S. Singeetham, "An optimised design of a typical subsea drilling system for fatigue applications," *OMAE 1989*, 1989. 2

[6] L. Reinås, T. Hørte, M. Sæther, and G. Grytøyr, "Wellhead fatigue analysis method," *ASME Conference Proceedings*, no. OMAE2011-50026, 2011. 2, 13

[7] D. Buchmiller, T. Hørte, G. Grytøyr, L. Haug, and DNV, "Establishing an industry best practice on subsea wellhead fatigue assessment," *IADC/SPE Drilling Conference and Exhibition*, no. SPE-151198, 2012. 3, 30

[8] L. Reinås, M. Sæther, and B. S. Aadnœy, "The effect of a fatigue failure on the wellhead ultimate load capacity," *ASME Conference Proceedings*, no. OMAE2012-83325, 2012. 3

[9] L. Reinås, M. Russo, and G. Grytøyr, "Wellhead fatigue analysis method: The effect of variation of lower boundary conditions in global riser load analysis," *ASME Conference Proceedings*, no. OMAE2012-83314, 2012. 4, 11, 53, 96, 115, 128

[10] D. Williams and J. Greene, "The effects of modelling techniques and data uncertainty in wellhead fatigue life calculation," *ASME Conference Proceedings*, no. OMAE2012-83755, 2012. 4, 12, 13, 35, 69, 70, 96, 118, 128

[11] T. Hørte, L. Reinås, and J. Mathisen, "Wellhead fatigue analysis method: Benefits of a structural reliability analysis approach," *ASME Conference Proceedings*, no. OMAE2012-83141, 2012. 6, 17

[12] M. Russo, L. Reinås, M. Sæther, and H. Holden, "Fatigue assessment of subsea wells for future and historical operations based on measured riser loads," *ASME Conference Proceedings*, no. OMAE2012-83162, 2012. 6, 115, 128, 131

[13] T. K. Lim, E. Tellier, and H. Howells, "Wellhead, Conductor and Casing fatigue - Causes and Mitigation," *2H Offshore*, 2012. 6

[14] S. Sangesland, "Drilling and completion of subsea well - An overview," *Addendum to TPG4200 - NTNU*, January 2011. 9

[15] S. Sangesland, "Drilling and completion of subsea wells," 2008. 13

[16] D. Brooker, "Optimisation of drilling riser analysis for wellhead fatigue life calculations," June 2012. 13

[17] International Association of Drilling Contractors, "Typical subsea bop stack," 2011. 14

[18] Y. Bai and Q. Bai, *Subsea pipelines and risers*, vol. 3. Elsevier Science, 2005. 15

[19] M. A. Richbourg and K. A. Winter, "Subsea tree and wellheads: The basics," *COURSE TPG4200 Subsea Production Systems NTNU.*, 1998. 16

[20] J. T. Evans and J. McGrail, "An evaluation of the fatigue performance of subsea wellhead systems and recommendations for fatigue enhancements," *Offshore Technology Conference*, May 2011. 17

[21] O. de Brito Collaço Veras, P. J. Simpson, and F. E. Roveri, "A System For Measuring Wellhead Bending Moments During Completion Operations," *2H Offshore*, 2010. 18, 41

[22] ISO, "ISO - 19901:4 - petroleum and natural gas industries - Specific requirements for offshore structures – part 4: Geotechnical and foundation design considerations," tech. rep., ISO, 2003. 18

[23] ISO, "ISO - 19902: Petroleum and natural gas industries - Fixed steel offshore structures," tech. rep., ISO, 2007. 18

[24] API, "API RP2A - American Petroleum Institute Recommended Practice for Planning, Designing and Constructing Fixed Offshore Platformsworking Stress Design," tech. rep., API, July 1993. 18

[25] A. Standard, "E1049," *Standard Practices for Cycle Counting in Fatigue Analysis, Phila-delphia, PA*, 1985. 19

[26] FAMU/FSU College of Engineering, "Fatigue testing theory," 2007. 20

[27] S. Berge, *Fatigue and Fracture Design of Marine Structures 2, Fatigue Design of Welded Structures.* Faculty of Engineering Science and Technology - NTNU Trondheim, 2006. 20, 22, 23, 25, 26

[28] "Basic fatigue design, Concepts in Eurocode 3," *University of Ljubljana*, 2012. 21

[29] T. Irvine, "Rainflow cycle counting in fatigue analysis," August 2011. 25

[30] L. Damkilde, "Lecture notes in advanced structural engineering," 2013. 26

[31] DNV, "DNV-RP-C203 Fatigue design of offshore steel structures," 2010. 26, 27, 66, 71, 92, 93, 123

[32] DNV, "DNV-OS-C101 Design of offshore steel structures, general (LRFD METHOD)," April 2011. 27

[33] J. Buitrago, V. R. Krishnan, and P. M. Sommerfield, "Fatigue assessment of subsea tree connectors and wellheads," *ASME Conference Proceedings*, no. 49853, 2011. 29

[34] P. An, E. Elletson, and P. Ward, "Mitigation of wellhead and conductor fatigue using structural monitoring," 2012. 30

[35] O. Faltinsen, *Sea loads on ships and offshore structures*, vol. 1. Cambridge university press, 1993. 30, 32, 33, 36, 37, 38, 39, 40, 79, 88, V

[36] DNV, "DNV-RP-C205 Environmental conditions and environmental loads," 2010. 33, 37

[37] J. Journée and W. Massie, *Offshore Hydromechanics*. Delft University of Technology, January 2001. 34, 35, 37, 39, 40

[38] J. A. Pinkster, *Low Frequency Second Order Wave Exciting Forces On Floating Structures*, vol. 650. Netherlands Ship Model basin, Wageningen, 1980. 35

[39] J. R. Morison, J. Johnson, and S. Schaaf, "The force exerted by surface waves on piles," *Journal of Petroleum Technology*, vol. 2, no. 5, 1950. 37

[40] H. C. Karlsen, *Statistics of wave induced nonlinear loads and responses*. PhD thesis, Norwegian University of Science and Technology, September 2006. 38

[41] H. Maruo, "The drift of a body floating on waves," *Journal of Ship Research*, vol. 4, pp. 1–5, 1960. 39

[42] C. Chryssostomidis and Y. Liu, *Design of Ocean Systems*. MIT, 2011. 40

[43] C. M. Larsen, "VIV - a short and incomplete introduction to fundamental concepts," February 2010, Trondheim. 41

[44] H. Blackburn, R. Govardhan, and C. Williamson, "A complementary numerical and physical investigation of vortex-induced vibration," *Journal of Fluids and Structures*, vol. 15, pp. 481 – 488, 2001. 41

[45] J. Thorogood, A. Train, and A. Adams, "Deep water riser system design and management," in *IADC/SPE drilling conference*, 1998. 41

[46] M. Campbell and M. Tognarelli, "Drilling riser VIV: Fact or fiction?," in *IADC/SPE Drilling Conference and Exhibition*, 2010. 41

[47] C. Hopper, "Vortex induced oscillations of long marine drilling risers," *Proc. of DOT*, pp. 97–109, 1983. 41

[48] T. Sarpkaya, "A critical review of the intrinsic nature of vortex-induced vibrations," *Journal of Fluids and Structures*, vol. 19, no. 4, pp. 389 – 447, 2004. 42

[49] C. K. Morooka, R. I. Tsukada, and D. M. Brandt, "Numerical simulations of ocean drilling system behavior with a surface or a subsea BOP in waves and current," *ASME Conference Proceedings*, no. OMAE2008-5737, 2008. 42

[50] C. Felippa, "Introduction to finite element methods," *University of Colorado, Boulder - http://www.colorado.edu/engineering/CAS/courses.d/IFEM.d*, 2004. 43, 45

[51] T. Moan, "Nonlinear analysis," *Addendum to TMR4305 - NTNU*, 2007. 43, 48, 49, 50

[52] Simulia, "Abaqus documentation - version 6.12," *Simulia Corporation*, 2012. 44, 47

[53] T. Moan, *Finite Element Modelling and Analysis of marine Structures.* NTNU, September 2003. 45, 47

[54] S. S. Rao, *The Finite Element Method in Engineering.* Elsevier, 2011. 46

[55] J. W. Stærdahl, "Finite element method II - Powerpoint presentation," 2011. 46

[56] S. Sævik, "Lecture notes in offshore pipeline technology," *NTNU*, January 2012. 51, 52

[57] C. P. Sparks, *Fundamentals of marine riser mechanics: basic principles and simplified analyses.* PennWell Books, 2007. 52

[58] ISO, "ISO/TR - 13624-2 - petroleum and natural gas industries - Drilling and production equipment Part 2: Deepwater drilling riser methodomethod, operations and integrity technical report," tech. rep., ISO, 2009. 53

[59] I. Langen and R. Sigbjörnsson, *Dynamic analysis of structures.* Tapir, 1979. 53, 56, 58, 59, 60

[60] I. Fylling, C. Larsen, N. Sødahl, E. Passano, A. Bech, A. Engseth, H. Lie, and H. Ormberg, "Riflex user manual 3.6," *MARINTEK, Trondheim, Norway*, 2008. 53, 55, 56

[61] I. Fylling, C. Larsen, N. Sødahl, H. Ormberg, A. Engseth, E. Passano, and K. Holthe, "RIFLEX - Theory manual," *SINTEF report no. STF70 F*, vol. 95219, 1995. 53, 54, 59

[62] G. Forristall and C. Cooper, "Design current profiles using empirical orthogonal function (eof) and inverse form methods," in *Offshore Technology Conference*, 1997. 70

[63] MATLAB, *MATLAB - Version 8.0.0.783 (R2012b)*. Natick, Massachusetts: The MathWorks Inc., 2012. 82

[64] P. Brodtkorb, P. Johannesson, G. Lindgren, I. Rychlik, J. Rydén, and E. Sjö, "WAFO - a Matlab toolbox for the analysis of random waves and loads," in *Proc. 10'th Int. Offshore and Polar Eng. Conf., ISOPE, Seattle, USA*, vol. 3, pp. 343–350, 2000. 92

[65] H. J. Sutherland, *On the fatigue analysis of wind turbines*. Sandia National Laboratories Albuquerque, 1999. 92

[66] P. Johannesson, T. Svensson, and J. de Maré, "Fatigue life prediction based on variable amplitude tests-methodology," *International Journal of Fatigue*, vol. 27, no. 8, pp. 954 – 965, 2005. 123

Appendices

Appendix A

Local Models of the Blowout Preventer

This appendix contains all relevant data on the 3D element model of the BOP stack as well as the elastic beam model of the BOP stack. It is emphasized that the data on the 3D element model was condensed and sanitized to make the 3D element model suitable for public dissemination.

A.1 3D Element Model

The 3D element model of the blowout preventer stack was provided by Statoil. It was received as an *.*inp*-file, a data file containing all the coordinates(x,y,z) for all global nodes. Further, the data file also contains all the element nodes, meaning the local nodes of each element have a corresponding global node number thus assigning a specific location to each element in space. Abaqus reads this *.*inp*-file and constructs the complete 3D element model based on the coordinates of global nodes in combination with the local node numbers of each element. By editing the coordinates of all global nodes in the *.*inp*-file, the constructed model was condensed and sanitised. It was also through this process that thickness reduction at assumed LMRP connector location could take place. Modification of the coordinates in the data file must be done with caution, as irregularities in geometry can occur and render the model invalid.

The model was constructed using 20-node solid elements for the main structure and 3D beam elements for the framework. This is in accordance with the JIP [3]. The model consists of 19 420 elements based on the coordinates of 105 325 nodes. The regions 1, 2 and 3 marked on figure A.1 are the position of the lower flex joint, the assumed position of the LMRP connector and the position of the wellhead connector, respectively.

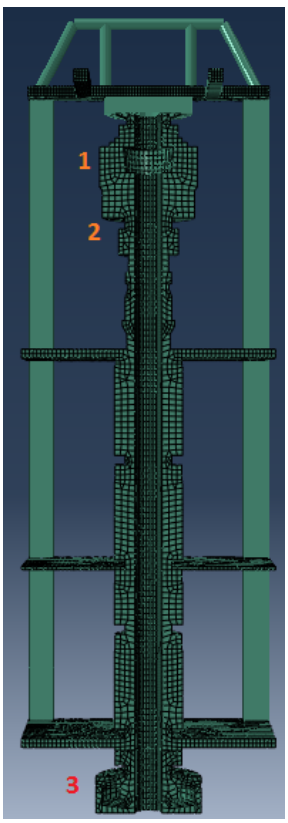

(a) Front view

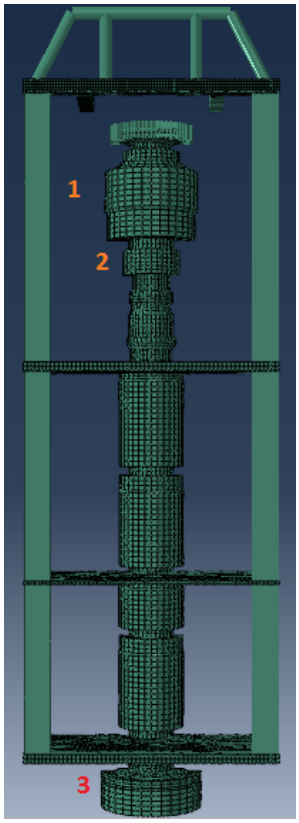

(b) Back view

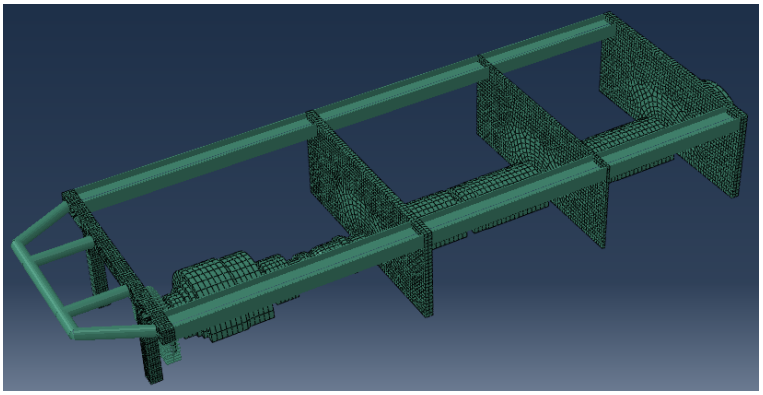

(c) Isometric view

Figure A.1: Front, back and isometric view 3D FEM model

Mass (dry weight)	190 000	[kg]
Mass (in water)	162 000	[kg]
Center of gravity (x,y,z)	(0 , 0 , 7.57)	[m]
Height	12.4	[m]
Material density	7850	[kg/m^3]
Young's Modulus	2.1×10^{11}	[N/m^2]

Table A.1: BOP Model Specifics

A.2 Elastic Beam Model

The elastic beam model has height equal to the distance from the bottom to the lower flex joint on the 3D element model(marked as index 1 in figure A.1a. The reason for this is that forces and moments from global analyses conducted in Riflex are imported at the lower flex joint in the global model. Furthermore, the beam was divided into five sections, see figure A.2. By doing this, it was possible to represent the 3D element model in an adequate way by calibrating the beam wall thickness in the different sections. This process is thoroughly explained in appendix B, section B.3.

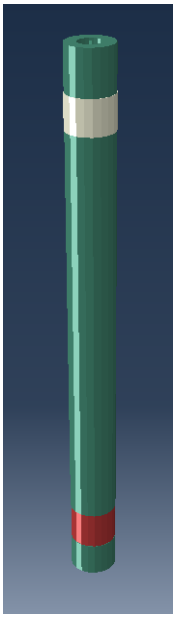

Figure A.2: Simplified beam model

In contrast to the 3D element model, the elastic beam model was built using 3D beam elements exclusively. The 3D element model is modelled mostly solid elements, which cannot reproduce nodal bending/rotation. This means that the bending moments that

were imported from Riflex required some modifications they could be applied to the 3D element model. This was not necessary for the elastic beam model. In addition, only the half of the BOP is present in the 3D element model, meaning the magnitude of the forces and bending moments that were imported from Riflex had to be divided by two to account for this. For the elastic beam model, the full magnitude can be used. This process is thoroughly explained in appendix B, section B.2.

Appendix B

Calibration of the Elastic BOP Stack Model

This appendix contains the relevant information on the procedures that were conducted in the calibration of the elastic BOP stack model. In order to investigate the stiffness characteristics of the 3D element model, loads were applied. The magnitude of these loads was obtained from global analyses of the drilling system.

B.1 Displacement and Loads at the Lower Flex Joint

In order to obtain the magnitude of the loads at the lower flex joint, a global analysis was conducted where the BOP stack was modelled as a beam with infinitely high stiffness. For this purpose, three different significant wave heights, H_s, from the scatter diagram in Faltinsen [35] were chosen. The corresponding spectral peak periods, T_p, were selected on the basis of the highest number of wave observations, see bold entries in table 7.8. Global response analyses were subsequently executed for each sea states. The simulation length of the analyses was 3700 seconds. Axial force, shear force and displacement in the x-direction and moment about y-axis at the lower flex joint were extracted from the analysis results and plotted functions of time. The first 100 seconds of the analyses results were omitted to avoid the influence of transient effects. For each sea state, the maximum displacement was observed, and the corresponding axial force, shear force and moment was noted. This is summarized in table B.1. These were the forces that were applied in the 3D element model in Abaqus.

The moments that were extracted from Riflex have a negative sign. These moments act clockwise. In the local model, moments were applied to coincide with the coordinate system in Abaqus and the sign may therefore change.

	Sea state #1	Sea state #2	Sea state #3	
T_p	13	12	9	[s]
H_s	8	6	3	[m]
Axial force	8.06×10^5	8.14×10^5	7.78×10^5	[N]
Moment	-2.82×10^5	-2.52×10^5	-1.71×10^5	[N m]
Shear force	6.32×10^4	5.63×10^4	4.02×10^4	[N]
Displacement	0.0818	0.0734	0.0523	[m]

Table B.1: Forces, moments and displacements in lower flex joint at corresponding sea states

B.1.1 Displacement

A comparison between the displacements at the lower flex joint for the three sea states shows that the displacement magnitude increases with more harsh sea, which was expected.

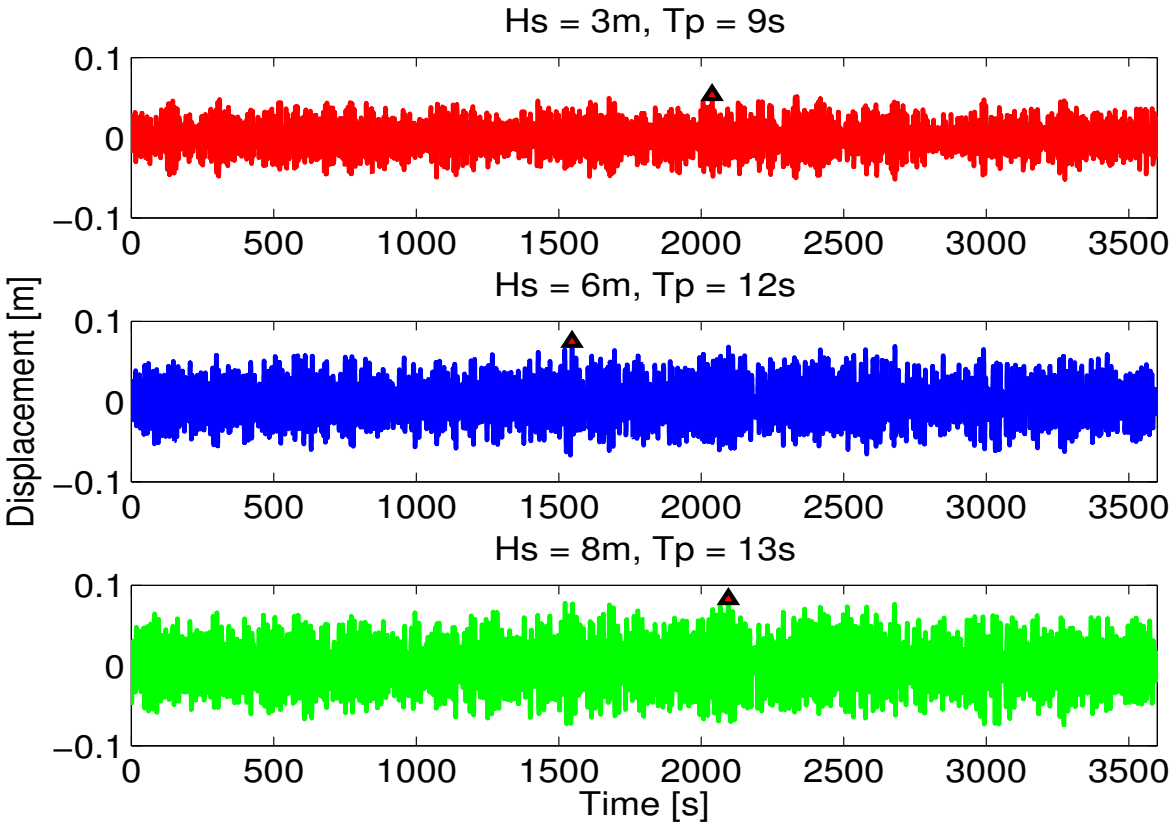

Figure B.1: Displacement comparison

B.1.2 Axial force, Shear force and Moment

A comparison between the axial forces at the lower flex joint for the three sea states shows at the time step where the displacement magnitude is at its largest (marked with red arrow on figure B.2) the axial force is near its minimum. It is noted that the axial force is largest in the second most harsh sea state, and this may be coincidental.

A comparison between the shear forces at the lower flex joint for the three sea states shows at the time step where the displacement magnitude is at its largest (marked with red arrow on figure B.3) the shear force is near its maximum.

A comparison between the moments at the lower flex joint for the three sea states shows at the time step where the displacement magnitude is at its largest (marked with red arrow on figure B.4) the bending moment is near its maximum.

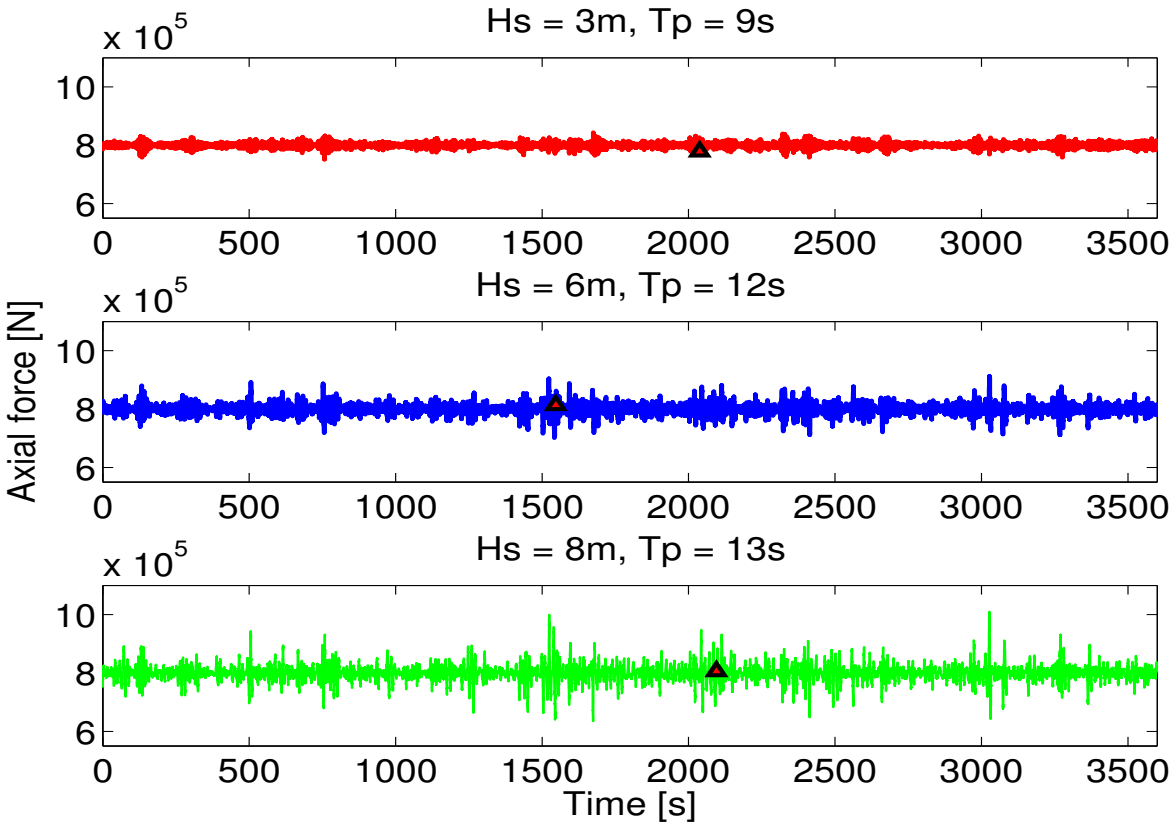

Figure B.2: Axial force comparison

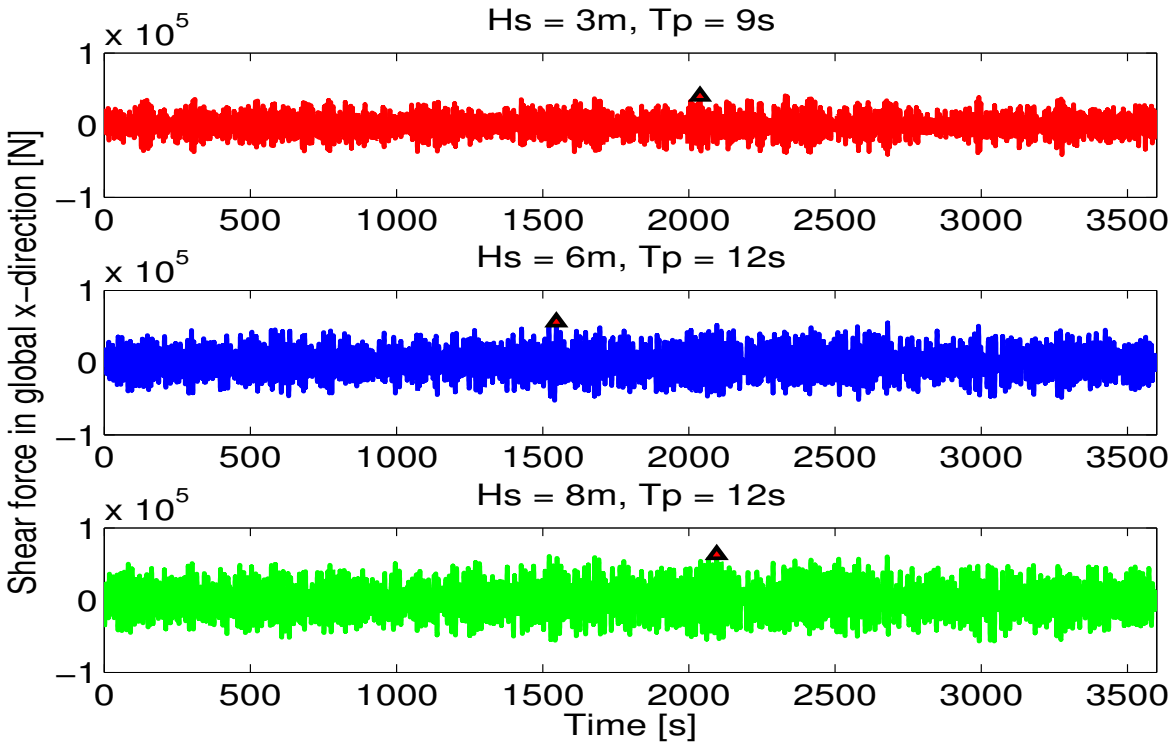

Figure B.3: Shear force comparison

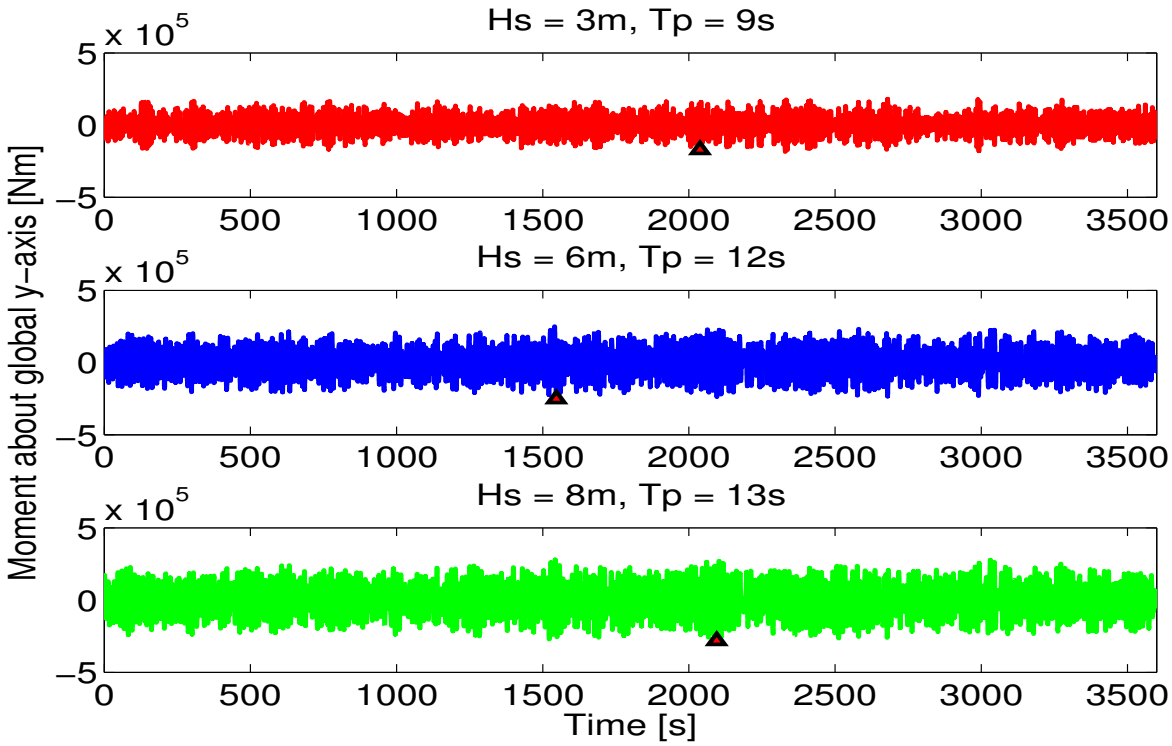

Figure B.4: Moment comparison

B.2 Nodal Forces in the 3D Element Model

The loads that were extracted from Riflex at the lower flex joint had to be processed before they could be implemented in the 3D element model. This is because these loads were extracted from a single node in the global model. In the 3D element model they were distributed to several nodes to avoid local yielding of the material. The axial and shear forces were thus divided on the number of element nodes they were assigned to. For this study, twelve nodes in the 3D element model were used, six nodes on each side of the flex joint. The bending moment that was imported from Riflex required additional processing before it could be implemented in the 3D element model. Since only the half of the BOP was modelled in the FEM model, the magnitude of the forces and moments was divided by two. This is to account for the fact that only half the cross sectional area is present and thus only half the stiffness is present.

B.2.1 Axial Force and Shear Force

The processed shear force was applied in the positive x-direction in the 3D element model in Abaqus as can been seen on figure B.5. This is the same direction as the shear force acts in Riflex.

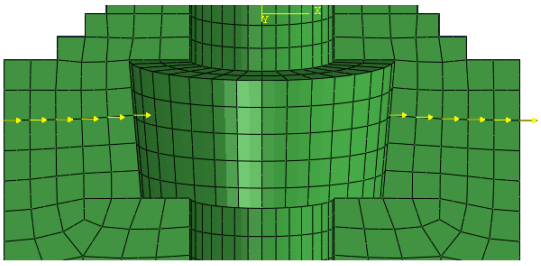

Figure B.5: Nodal shear forces

Shear force from Riflex [N]	
Sea state #1	6.32×10^4
Sea state #2	5.63×10^4
Sea state #3	4.02×10^4

Nodal shear forces Abaqus [N]	
Sea state #1	2633
Sea state #2	2346
Sea state #3	1675

Table B.2: Shear force processing

The processed axial force is applied in the positive z-direction in the 3D element model in Abaqus as can been seen on figure B.6. This is the same direction as the axial force acts in Riflex.

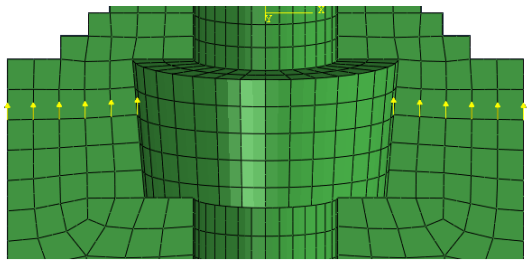

Figure B.6: Nodal axial forces

Axial force from Riflex [N]	
Sea state #1	8.06×10^5
Sea state #2	8.14×10^5
Sea state #3	7.78×10^5

Nodal axial forces Abaqus [N]	
Sea state #1	33 580
Sea state #2	33 917
Sea state #3	32 417

Table B.3: Axial force processing

B.2.2 Bending Moment

The bending moment that was imported from Riflex required additional processing before it could be implemented in the 3D element model. Firstly, the 3D element model consists mostly of solid elements which cannot rotate and thus are unable to reproduce moment behavior. A way to go about this was to simulate a moment about the middle of the flex joint section by assigning vertical nodal forces with opposite sign. Secondly, the nodal forces on each node must, in total, constitute a moment equal to that which was imported from Riflex, though divided by two for reason mentioned earlier. The nodal forces were set equal in all nodes. The correct magnitude of the force to constitute the required moment was found by goal seeking in Excel. Thirdly, the moments from Riflex have a negative sign and it is established that these moment act clockwise. When the moments were implemented in Abaqus, they were applied so that they worked correctly in Abaqus and the sign could therefore change.

Bending moment from Riflex [N m]		Conversion to Abaqus [N m]	
Sea state #1	-2.82×10^5	Sea state #1	-1.41×10^5

Node #	Distance from center [m]	Nodal force [N]	Moment [N m]
1	0.4225	−18 433	−7788
2	0.50893	−18 433	−9381
3	0.59527	−18 433	−10 973
4	0.6805	−18 433	−12 544
5	0.7665	−18 433	−14 129
6	0.8509	−18 433	−15 685
		Sum	-7.05×10^4

Table B.4: Moment processing sea state #1

In table B.4, the node number is self explaining, and the distance is the x-coordinate of the node. The center of the flex joint has x-coordinate equal to 0. Further, the table only shows the processing for the nodes that have positive x-coordinates, i.e. the nodes at the right hand side of the flex joint center. The processing is identical for the left hand side with the exception of the entries in the distance column and nodal force column, where the sign will change. The total moment about y-axis in the local model is then $2 \cdot (-7.05 \times 10^4 \text{N m}) = -1.41 \times 10^5 \text{N m}$, and is illustrated in figure B.7.

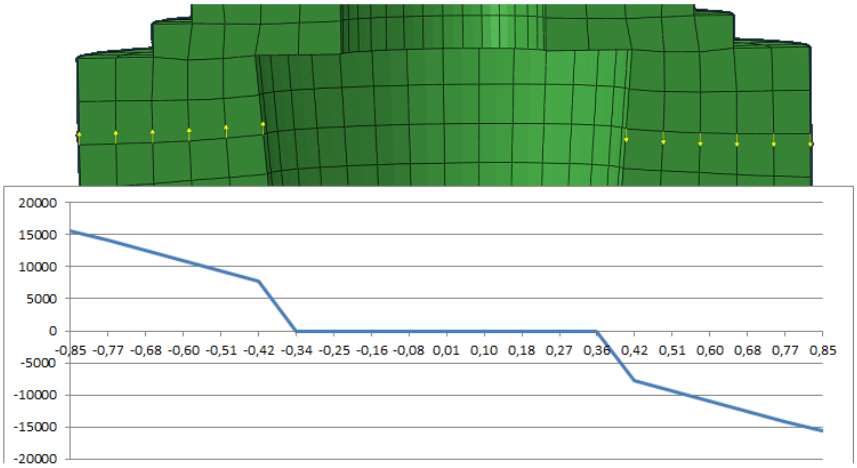

Figure B.7: Moment distribution [N m]

The same procedure was also applied for sea state #2 and sea state #3. Also here only the right hand side of the flex joint is considered.

Bending moment from Riflex [N m]		Conversion to Abaqus [N m]	
Sea state #2	-2.52×10^5	Sea state #2	-1.26×10^5
Sea state #3	-1.71×10^5	Sea state #3	-8.55×10^4

		Sea state #2		Sea State #3	
Node #	Dist. [m]	Nodal force [N]	Moment [N m]	Nodal force [N]	Moment [N m]
1	0.4225	−16 472	−6960	−11 178	−4723
2	0.50893	−16 472	−8383	−11 178	−5689
3	0.59527	−16 472	−9805	−11 178	−6654
4	0.6805	−16 472	−11 209	−11 178	−7606
5	0.7665	−16 472	−12 626	−11 178	−8568
6	0.8509	−16 472	−14 016	−11 178	−9511
		Sum	-6.3×10^4	Sum	-4.275×10^4

Table B.5: Moment processing sea state #2 and sea state #3

B.3 Calibration procedure

The input stiffness parameters of the elastic BOP stack in the global model should be obtained by calibrating an elastic beam model in Abaqus. The calibration was done by using the 3D element model of the BOP stack as the frame of reference. The idea was to calibrate the beam so that its stiffness properties are the same as the 3D element model. In order to do this, the 3D element model and the elastic BOP model were loaded with the equivalent loads. The resulting displacement of the 3D element model was compared to the resulting displacement of the elastic BOP model. The loads that were applied are listed in table B.1. When the 3D element model was exposed to the loading configurations from sea state #1, #2 and #3, the resulting displacement was plotted. This is shown in figure B.8

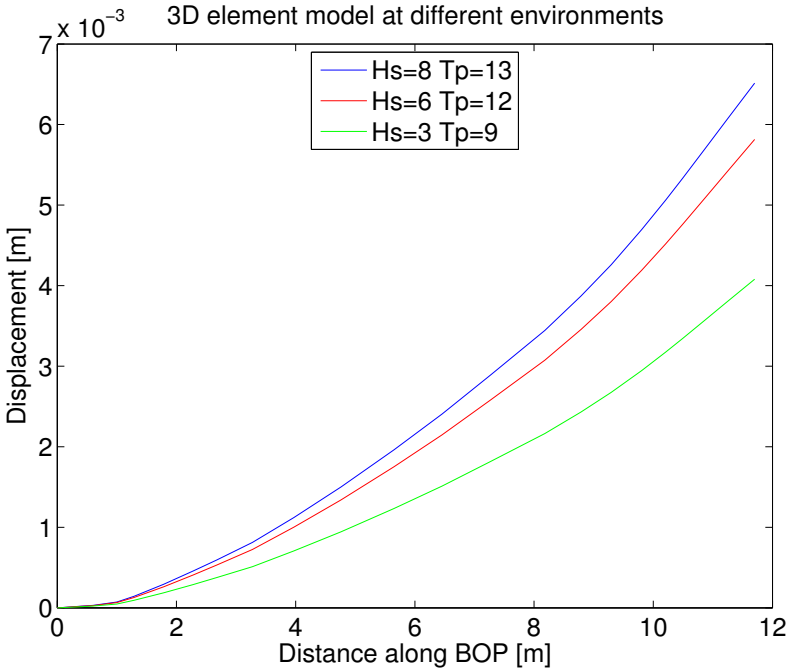

Figure B.8: 3D element model displacement

In the calibration procedure, the loads that were used are the processed forces and moments from Riflex for sea state #1. The final calibration result was verified by the forces and moments from sea state #2 and sea state #3. The 3D element model was loaded as described in section B.2.1. The elastic BOP model was loaded in the node at the top end (end of section 5). Since this is a beam, the nodes have all the degrees of freedom required to reproduce translation and rotation. This means that in addition

to the axial force and shear moment, the bending moment could be applied directly without any processing required. Also, the elastic BOP model was loaded with the full magnitude of the loads from Riflex since it is a complete model, while the 3D element model was loaded with the processed load.

The main parameter affecting the displacement magnitude is the bending stiffness, EI. The Young's modulus, E, is a material parameter and may not be changed. This implies that the second moment of area, I, must be changed. The formula for the second moment of area for a pipe may be written as:

$$I = \frac{\pi}{64}\left(d_o^4 - d_i^4\right) \tag{B.1}$$

The inner diameter of the pipe, d_i, is set to $18\,3/4''$ as a default parameter. It is thus only possible to alter the outer diameter, d_o. The thickness of the elastic beam model was altered to obtain new displacements. If the displacements relative to the 3D element model were to small, the beam model was too stiff. Consequently the pipe diameter in the elastic beam model was reduced. The 3D element model and the elastic BOP model side by side illustrated below.

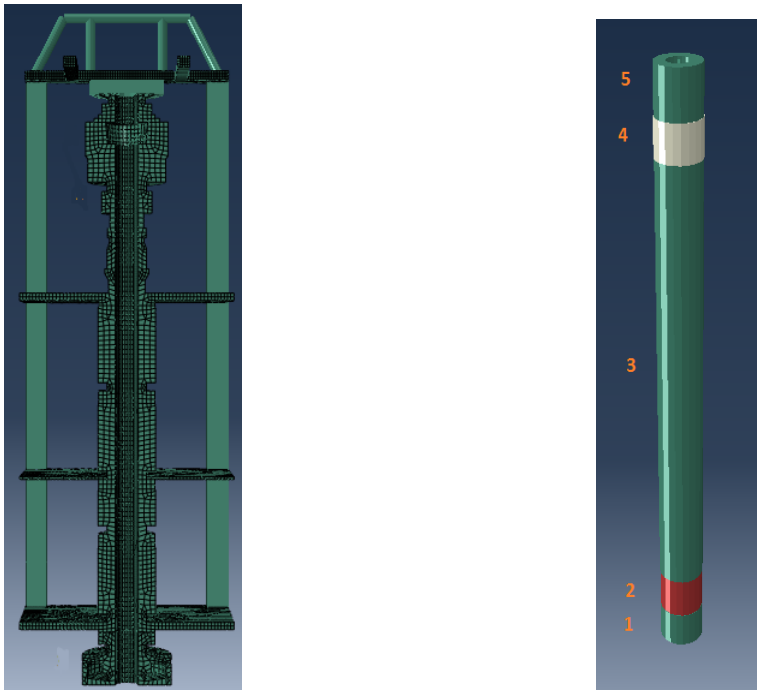

(a) 3D element model (b) Elastic BOP model

Figure B.9: 3D element model and elastic BOP model

The method may be described as a trial and error process, the input parameters (different pipe thickness) for each run were decided on the basis of engineering judgement. The first try at creating a beam was done by estimating an average thickness of the wall of the 3D element model. The inner pipe diameter was given as $18\,3/4''$ as a default parameter for every section of the beam. The thickness was assumed to be less in the sections where LMRP (4) and wellhead connector (2) are located. The first run is summarized below, where the thickness applied in each section is found in table B.6 and the corresponding displacement result is seen in figure B.10.

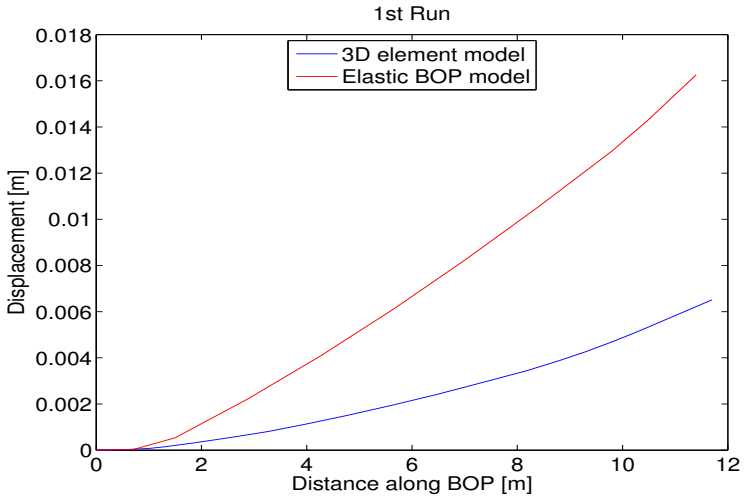

Figure B.10: Displacement - 1st run

	Thickness [m]
Section 1	0.25
Section 2	0.05
Section 3	0.25
Section 4	0.05
Section 5	0.25

Table B.6: Section thickness - 1st run

From the figure above it is seen that the displacement of the simplified beam was much too high and this points to insufficient bending stiffness. The thickness in each section was altered to atone for the lack of bending stiffness. Additional 4 runs were required to obtain a satisfying similarity between the elastic BOP model and the 3D element model. These runs are summarized in table B.7 and the corresponding displacement result in

	Thickness [m]			
	2nd run	3rd run	4th run	5th and final run
Section 1	0.50	0.38	0.25	0.24
Section 2	0.20	0.20	0.25	0.23
Section 3	0.50	0.38	0.25	0.24
Section 4	0.30	0.20	0.25	0.25
Section 5	0.50	0.38	0.25	0.24

Table B.7: Thickness - 2nd to 5th calibration run

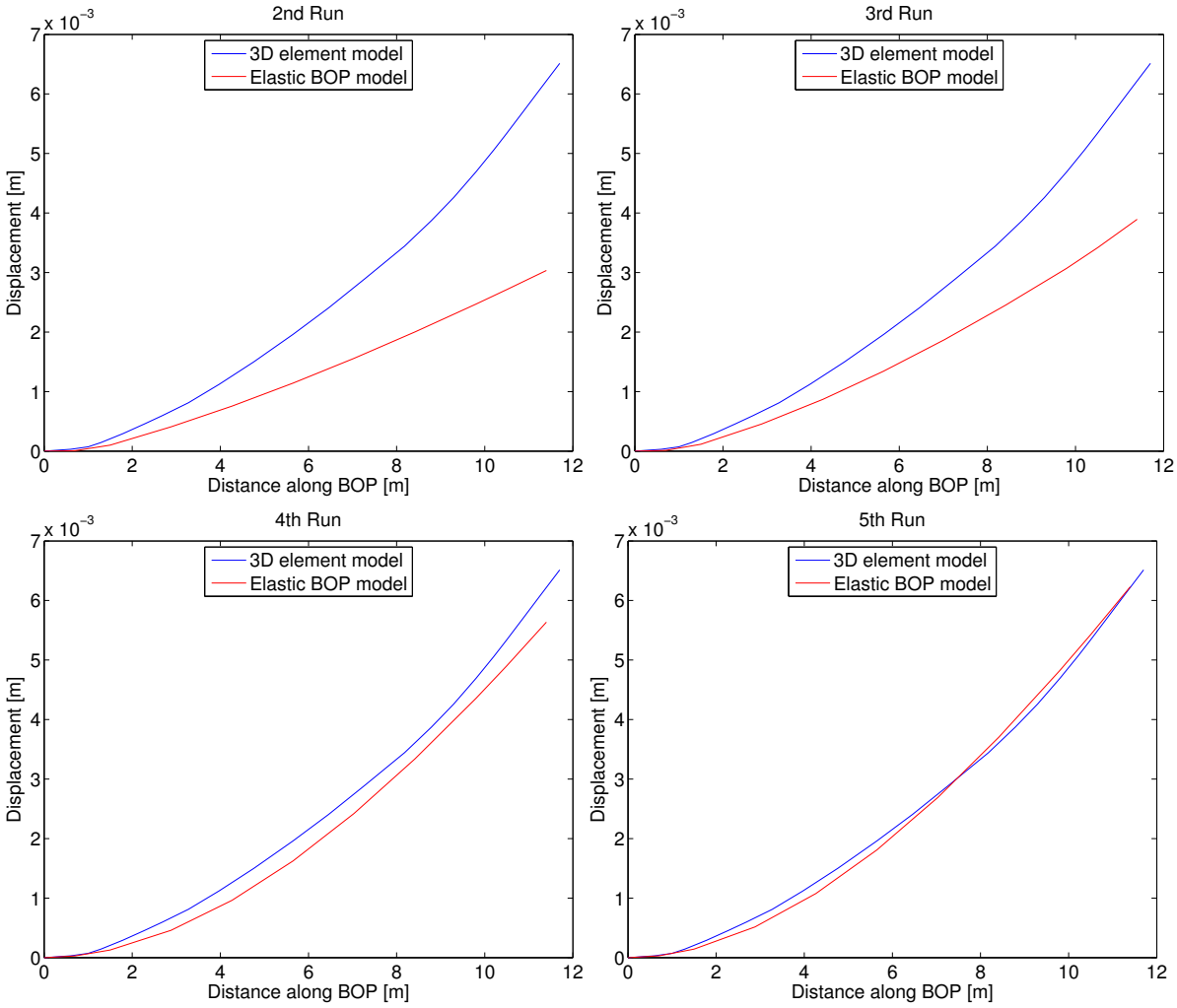

Figure B.11: Displacement - 2nd to 5th calibration run

figure B.11. At the 5th run it is seen that the displacement of the simplified beam corresponds well with the displacement of the 3D FEM model. The inner diameter, d_i, and outer diameter, d_o give rise to the second moment of area, I (equation B.1), which in turn gives rise to the bending stiffness, EI.

	d_i [m]	Thickness [m]	d_o [m]	I [m^4]	EI [N m^2]
Section 1	0.47625	0.24	0.956	0.0385	8.09×10^9
Section 2	"	0.23	0.936	0.0352	7.39×10^9
Section 3	"	0.24	0.956	0.0385	8.09×10^9
Section 4	"	0.25	0.976	0.0421	8.83×10^9
Section 5	"	0.24	0.956	0.0385	8.09×10^9

Table B.8: Final elastic BOP build - local model

Subsequently, the elastic BOP was verified with the load configurations from sea state #2 and #3. The final build from table B.8 was employed together with the load configurations from sea state #2 and #3. The displacement of the elastic BOP model corresponds well with the displacement of the 3D element model as seen in figure B.12.

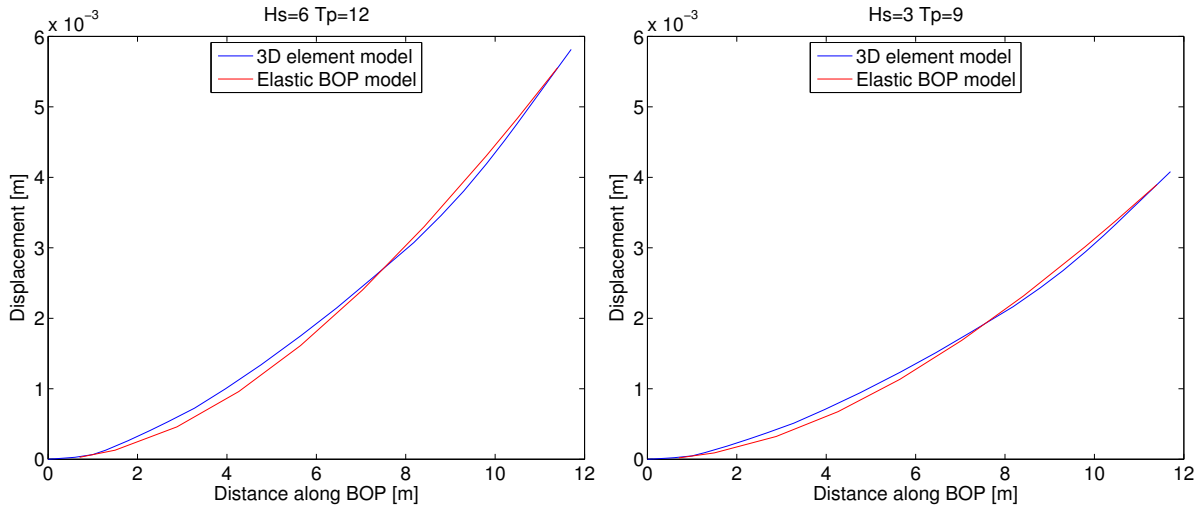

(a) Sea state #2

(b) Sea state #3

Figure B.12: Verification - 3D element model vs. elastic BOP model

Appendix C

Drilling System Configuration and Properties

The global analysis was conducted in the FEM software Riflex. For this study, the water level was set to 350 meter. The overall model configuration was setup to obtain an upper flex joint location of circa 30 meter above mean water level. The number of riser joints with and without buoyancy elements is based on a requirement of 50 tonnes of tension in the LMRP connector combined with 300 tonnes of top tension. The global model from top to bottom in table C.1 satisfies this tension requirement. The flex joints are modelled without lengths in Riflex and thus are not provided in the table, however, the lower flex joint is located between the BOP stack and the 10 foot joint and the upper flex joint is located near the top of the uppermost 10 foot joint. The global model also comprise of a set of RAOs to reproduce semi-submersible vessel motions.

	Start point [m]	Length/component [m]	No. of components
10′ Joint	30.18	3.05	1
30′ Joint	27.13	9.14	2
75′ Naked joint	8.85	22.86	6
75′ Buoy. joint	−128.31	22.86	9
10′ Riser joint	−334.05	3.05	1
BOP stack	−337.1	11.40	1
Wellhead	−348.50	4.6	1

Table C.1: Overall model configuration

C.1 Riser

The riser was modelled by use of several different riser joints. Each riser joint has its own set of properties. These are listed in table C.2.

	75′ Buoy. Joint	75′ Joint	30′ Joint	10′ Joint	
Mass per unit length	1000	600	730	1100	[kg/m]
Buoyancy area, AE	1.05	0.3	0.32	0.38	[m^2]
Moment of inertia	0.081	0.001	0.002	0.005	[m^4]
Axial stiffness, EA	7.06×10^9	"	"	"	[N]
Bending stiffness, EI	2.3×10^8	"	"	"	[N m^2]
Torsion stiffness, GI	4.4×10^4	"	"	"	[N m^2]
Hydrodynamic diameter	1.25	0.50	"	"	[m]
Internal diamter	0.60	"	"	"	[m]
Internal Area	0.28	"	"	"	[m^2]
External diameter	1.16	0.62	0.64	0.70	[m]
External Area	0.77	0.02	0.04	0.10	[m^2]
Gyration radius	0.33	0.21	0.22	0.23	[m]

Table C.2: Complete riser joint properties

C.2 Support vessel

The support vessel is implemented as a set of RAOs. The RAOs that are applied in this thesis are of first order. Waves are exclusively propagating in the x-direction, so any other direction can be omitted. Consequently, sway, roll and yaw are also omitted. The RAOs are illustrated in the figures below and tabulated in table C.3.

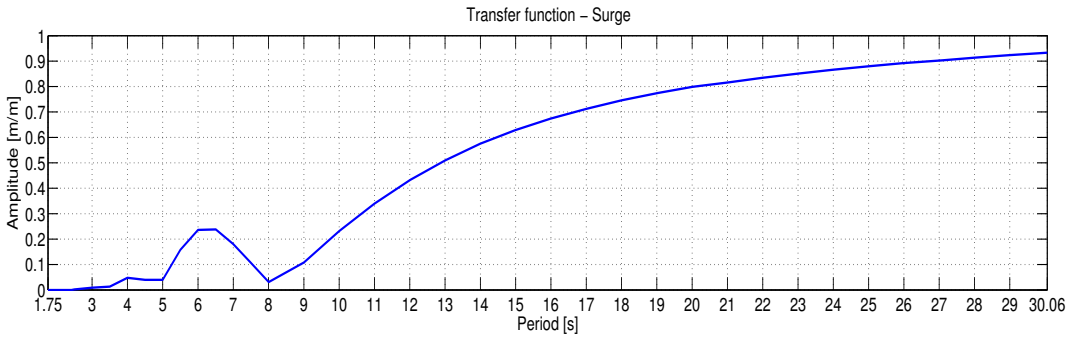

Figure C.1: RAO - Surge - Amplitude ratio

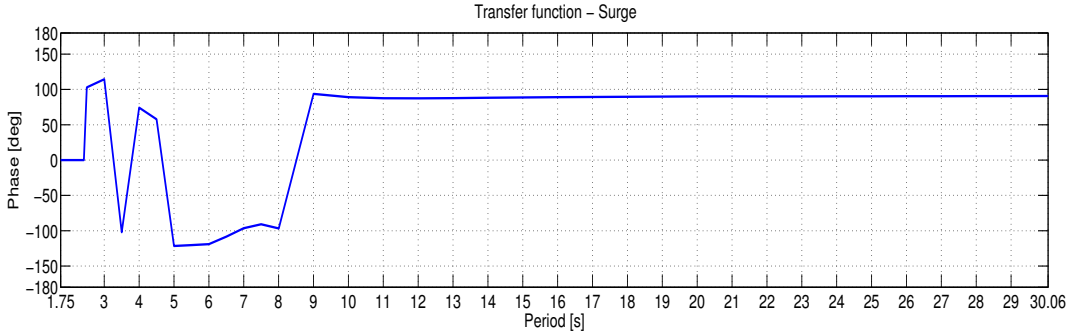

Figure C.2: RAO - Surge - Phase

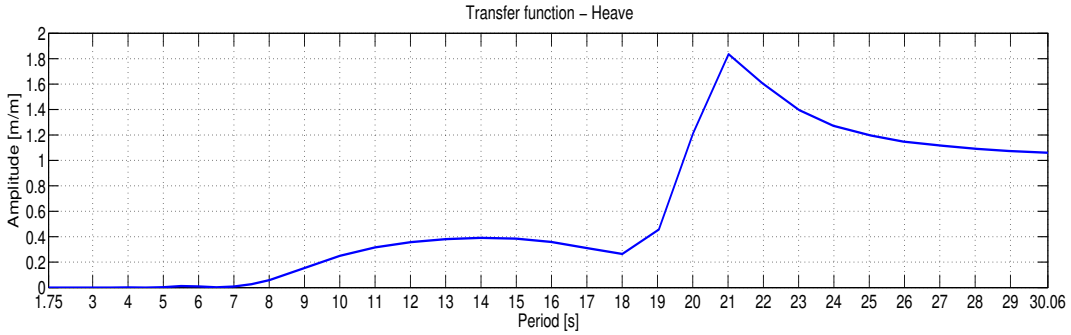

Figure C.3: RAO - Heave - Amplitude ratio

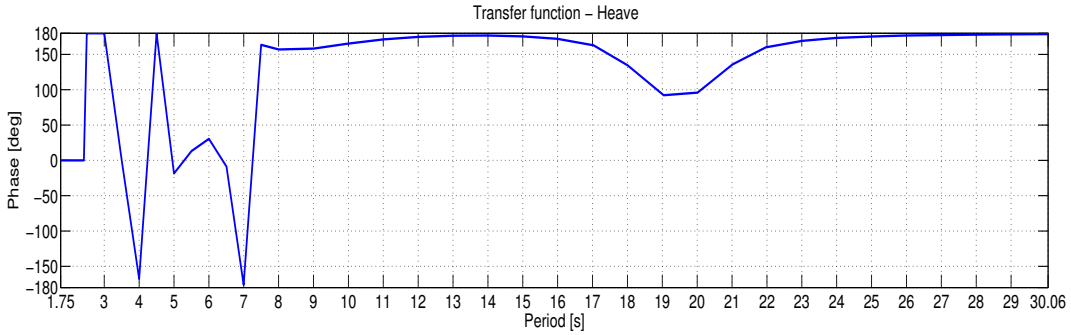

Figure C.4: RAO - Heave - Phase

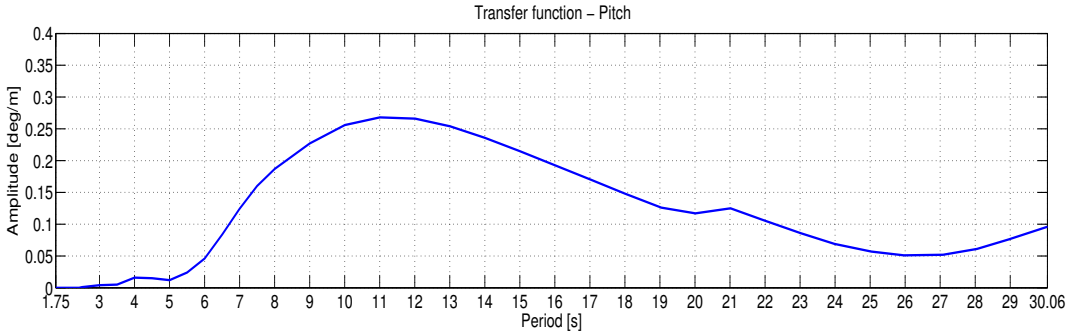

Figure C.5: RAO - Pitch - Amplitude ratio

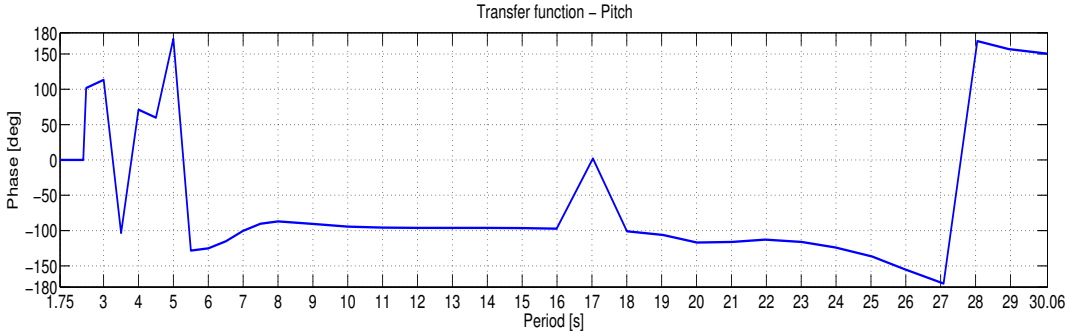

Figure C.6: RAO - Pitch - Phase

	Surge		Heave		Pitch	
Period	Amplitude	Phase	Amplitude	Phase	Amplitude	Phase
[s]	[m/m]	[deg]	[m/m]	[deg]	[$^{deg}/_{m}$]	[deg]
1.75	0.00	0.00	0.00	0.00	0.00	0.00
2.42	0.00	0.00	0.00	0.00	0.00	0.00
2.50	0.00	102.98	0.00	180.00	0.00	101.83
3.00	0.01	114.47	0.00	180.00	0.00	113.36
3.50	0.01	-102.06	0.00	0.00	0.01	-103.51
4.00	0.05	74.25	0.00	-167.65	0.02	71.28
4.50	0.04	57.85	0.00	180.00	0.02	59.84
5.00	0.04	-121.57	0.00	-18.54	0.01	171.55
5.50	0.16	-120.36	0.01	13.21	0.02	-128.29
6.00	0.24	-118.98	0.01	30.50	0.05	-125.17
6.50	0.24	-108.24	0.00	-8.74	0.08	-115.11
7.00	0.18	-96.44	0.01	-176.25	0.12	-100.42

Table C.3 – Continued on next page

Table C.3 – Continued from previous page

	Surge		Heave		Pitch	
Period [s]	Amplitude [m/m]	Phase [deg]	Amplitude [m/m]	Phase [deg]	Amplitude [deg/m]	Phase [deg]
7.50	0.11	-90.85	0.03	163.64	0.16	-90.37
8.00	0.03	-96.72	0.06	157.02	0.19	-87.02
9.00	0.11	93.69	0.15	158.26	0.23	-90.63
10.01	0.23	89.08	0.25	165.35	0.26	-94.37
11.00	0.34	87.58	0.32	171.33	0.27	-95.84
12.01	0.43	87.40	0.36	174.86	0.27	-96.17
13.01	0.51	87.74	0.38	176.48	0.25	-96.17
13.99	0.58	88.21	0.39	176.71	0.24	-96.23
15.00	0.63	88.66	0.39	175.56	0.22	-96.54
15.99	0.67	89.03	0.36	172.14	0.19	-97.25
17.03	0.71	89.34	0.31	162.92	0.17	2.00
18.00	0.75	89.60	0.26	134.70	0.15	-100.98
19.04	0.78	89.85	0.46	92.23	0.13	-106.24
20.01	0.80	90.19	1.21	95.91	0.12	-116.95
21.01	0.82	90.32	1.84	135.82	0.13	-116.17
21.97	0.83	90.22	1.61	160.02	0.11	-112.77
23.02	0.85	90.22	1.40	169.22	0.09	-116.04
23.98	0.87	90.26	1.27	173.31	0.07	-123.87
25.03	0.88	90.32	1.20	175.46	0.06	-136.65
25.96	0.89	90.38	1.15	176.72	0.05	-154.71
27.08	0.90	90.45	1.12	177.52	0.05	-174.93
28.05	0.91	90.54	1.09	178.06	0.06	168.20
28.95	0.92	90.65	1.07	178.44	0.08	156.93
30.06	0.93	90.78	1.06	178.72	0.10	150.36

Table C.3: RAOs for surge, heave and pitch

C.3 BOP stack

Global response analyses were conducted for two separate global models. The global models are identical with the exception of the BOP stacks structural properties. One global model comprises of the infinitely stiff BOP stack. The other global model comprises of the elastic BOP stack. Both BOP stacks are modelled as a beam in Riflex.

Both BOP stacks weigh the same as the provided 3D element model of the BOP stack and have the same center of gravity, see table A.1 for this info. It is noted that the length of the BOP stack in the global model is set to 11.4 meter contrary to the original length of 12.4 meter of the 3D element model. This is because the BOP stack models in Riflex are modelled from the wellhead to the lower flex joint. The remaining length is omitted.

The infinitely stiff BOP stack model is divided into two sections, see table C.4.

	Sections		
	1	2	
Length	5.70	"	[m]
Mass per length	5731	27 602	[kg/m]
Moment of inertia	0.0227	"	[m^4]
Axial stiffness	1×10^{12}	"	[N]
Bending stiffness	1×10^{11}	"	[$N\,m^2$]
Torsion stiffness	1×10^{11}	"	[$\frac{N\,m^2}{rad}$]
Internal diameter	0.476	"	[m]
Internal Area	0.178	"	[m^2]
External diameter	0.85	"	[m]
External Area	0.56	"	[m^2]
Gyration radius	0.15	"	[m]

Table C.4: Complete infinitely stiff BOP stack properties

The elastic BOP stack model is divided into six sections, see table C.5.

	Sections						
	1	2	3	4	5	6	
Length	0.705	0.794	4.202	4.097	0.706	0.899	[m]
Mass per length	5731	5731	S1	27 602	27 602	27 602	[kg/m]
Moment of inertia	0.0385	0.0352	S1	S1	0.0421	S1	[m^4]
Axial stiffness	1.13×10^{11}	1.07×10^{11}	S1	S1	1.20×10^{11}	S1	[N]
Bending stiffness	8.09×10^9	7.39×10^9	S1	S1	8.83×10^9	S1	[N m^2]
Torsion stiffness	1×10^{11}	"	"	"	"	"	[$\frac{N\,m^2}{rad}$]
Internal diameter	0.476	"	"	"	"	"	[m]
Internal area	0.178	"	"	"	"	"	[m^2]
External diameter	0.956	0.936	S1	S1	0.976	S1	[m]
External area	0.718	0.688	S1	S1	0.749	S1	[m^2]
Gyration radius	0.267	0.263	S1	S1	0.272	S1	[m]

Table C.5: Complete elastic BOP stack properties

Section 1, 3, 4 and 6 are identical with the exception of mass distribution and length. It is emphasized that this number of sections is not to be confused with the number of sections the local model of the elastic BOP is divided into, which is five. To aid the reader, section 1,3,4 and 6 in the global model corresponds to section 1, 3 and 5 in the local model. Section 2 in the global model corresponds to section 2 in the local model and section 5 in the global model corresponds to section 4 in the local model.

C.4 Wellhead

The wellhead and corresponding soil is modelled as a beam with an attached lateral spring in Riflex. The wellhead stick up is set to 1.5 meter above sea bottom. Although it may appear so on figure C.7, the lateral spring is not positioned at the bottom of the wellhead stick up. It is positioned 1 meter below wellhead datum, meaning in the global coordinate system it has a vertical coordinate of -349.5 meter.

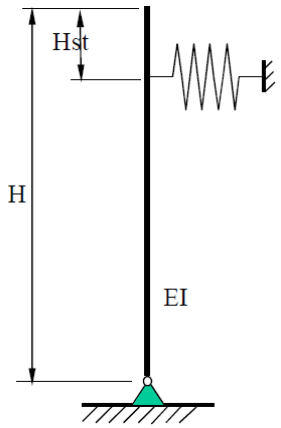

Figure C.7: Wellhead beam model [3]

Length, H	4.6	[m]
Stick up, Hst	1.5	[m]
Axial stiffness, EA	9.6×10^7	[kN]
Bending stiffness, EI	1.4×10^6	[kN m^2]
Torsion stiffness, GI	6.7×10^5	[kN m^2]
Stiffness lateral spring	35×10^3	[kN/m]
Position lateral spring below wellhead datum	1	[m]

Table C.6: Soil Beam Model

C.5 Flex Joint Data

Stiffness for typical flex joints were used in the global model in RIFLEX. The stiffness

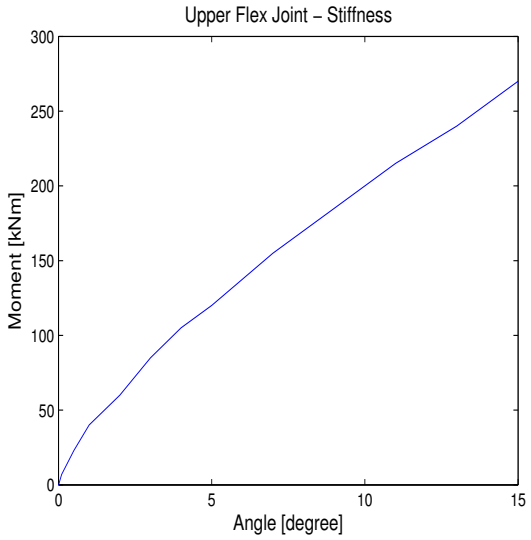

Figure C.8: Upper flex joint data plot

Moment [kN m]	Angle [deg]
0	0
7	0.1
23	0.5
40	1.0
60	2.0
85	3.0
105	4.0
120	5.0
155	7.0
185	9.0
215	11.0
240	13.0
270	15.0

Table C.7: Upper flex joint data

for the lower flex joint is as seen much higher than the upper flex joint.

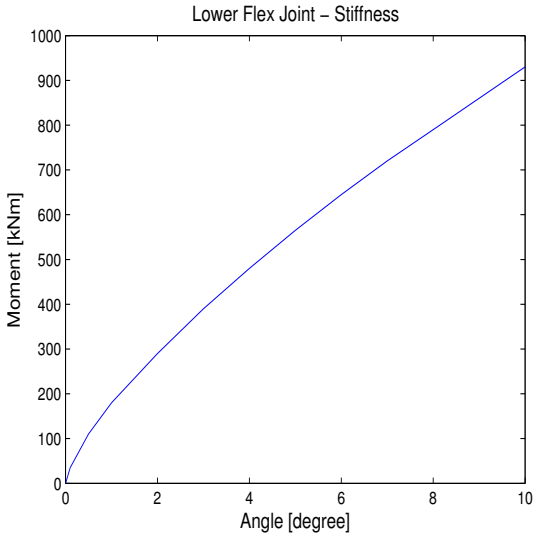

Figure C.9: Lower flex joint data plot

Moment [kN m]	Angle [deg]
0	0.0
35	0.1
110	0.5
180	1.0
290	2.0
390	3.0
480	4.0
565	5.0
645	6.0
720	7.0
790	8.0
860	9.0
930	10.0

Table C.8: Lower flex joint data

Appendix D

Fatigue damage assessment

D.1 Mean displacement at lower flex joint for $T_p = 9$s and all H_s

This analysis was conducted in order to ascertain the horizontal displacement of the two models of the BOP stack at the lower flex joint. It is seen that the elastic BOP stack model has greater displacement than the infinitely stiff BOP stack model for all H_s at $T_p = 9$m. The observation is seen for the case where the lower flex joint stiffness is non-linear as well as for the case where the lower flex joint stiffness is linear. It is also seen that the displacement is smaller when the flex joint has linear stiffness characteristics. The difference in displacement between the two BOP stack models is consistent for all H_s, with a marginally less difference between the two models when the flex joint has linear stiffness characteristics.

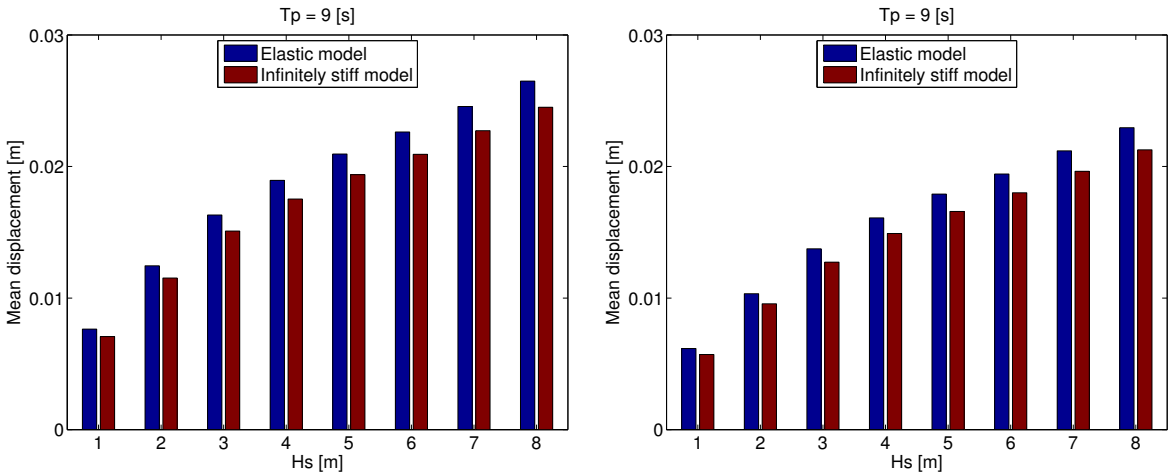

(a) Non-linear flex joint stiffness

(b) Linear flex joint stiffness

Figure D.1: Mean horizontal displacement at lower flex joint

H_s [m]	Mean displacement [mm] Inf. model	Elastic model	Δ %
1	7.07	7.64	7.45
2	11.52	12.45	7.47
3	15.09	16.32	7.48
4	17.53	18.95	7.48
5	19.38	20.95	7.49
6	20.93	22.62	7.50
7	22.72	24.56	7.50
8	24.51	26.49	7.49

Table D.1: Mean displacement at lower flex joint. Non-linear flex joint stiffness

Mean displacement [mm] Inf. model	Elastic model	Δ %
5.71	6.16	7.37
9.57	10.33	7.37
12.73	13.74	7.37
14.91	16.09	7.36
16.59	17.90	7.35
18.00	19.43	7.34
19.60	21.19	7.34
21.27	22.95	7.33

Table D.2: Mean displacement at lower flex joint. Linear flex joint stiffness

D.2 Fatigue damage assessment - MATLAB script

```
%% Clear workspace, command window and figure windows
clc
clear
close all

% Apply default plot properties
set(0,'DefaultAxesFontSize', 16)
set(0,'DefaultTextFontSize', 16)

% Weighted histogram values
b2 = 0; a2 = 0; c2 = 0; d2 = 0;

%% Data load
% Runs one time for each Hs, each Hs contains X number of Tp
for j = 1 : 8;
    load(['Hs',num2str(j),'.mat'])

    % Runs one time for each Tp
    for p = 1 : numel(Hsmomentswellheaddatum(1,:))
        % Extracting moments in KNm
        mom = Hsmomentswellheaddatum(:,p)/1000;
        % Removing average moment from all entries
        mom = mom - mean(mom);
        % removing first 100 seconds. Time increment = 0.25second,
        % first 400 terms are removed.
        mom(1:400) = [];
```

```
% Mapping from moment-time series to stress-time series
% using a load-to-stress curve for desired cement level.
stresstime(:,p) = cement_15m_load_to_stress(mom);

%% Rainflow counting
% Finding turning points
[tp_sea ind] = dat2tp(round(stresstime(:,p)));
% Rainflow counting
[RFCR,RFCUR,R] = tp2rfc(tp_sea);

%% Example plot of turning points for one sea state:
if p==5 && j==8
    momplot=figure;
    set(momplot, 'PaperPosition', [2.5 2.5 50 10]);
    plot([0.25:0.25:3600],mom);
    title('Hs = 8, Tp = 13')
    xlabel('Time [s]')
    ylabel('Moment [kNm]')
    xlim([ 0 3600])
    print(momplot,'-depsc','momploths8tp13')

    ind1=ind/4;
    stresstime8_4 = stresstime(:,p);
    turnplot=figure;
    set(turnplot, 'PaperPosition', [2.5 2.5 50 10]);
    plot([0.25:0.25:3600] , stresstime8_4)
    hold on
    plot(ind1,stresstime8_4(ind),'k^','markerfacecolor',[1,0,0])
    title('Hs = 8, Tp = 13 - Cement level: 15m')
    xlabel('Time [s]')
    ylabel('Stress [MPa]')
    xlim([ 0 3600])
    print(turnplot,'-depsc','turnploths8tp13')
end

%% SN - Data
% SN curve class:F1    DNV-RP-C203
m1=3;        % slope of the first curve
m2=5;             % slope of the second curve
Nk=1e7;      % kneepoint log N axis [Cycles]
st = 73.10;       % kneepoint stress range axis [MPa]
loga1= 10^11.699; % Intercept at log N axis for first curve
```

```
loga2= 10^14.832; % Intercept at log N axis for second curve

%%   Fatigue damage calculation
% The fatigue damage calculation is done for one sea state at the time.
% The Rainflow counts acts as input. RFCUR represents whole cycles
% (without residuals) and R represents half cycles(residuals).

% Stress range for whole cycles
RFCUR(:,3) = abs(RFCUR(:,2)-RFCUR(:,1));
% Stress range for half cycles
for n= 2:2:(numel(R(:,1)))
    R(n,3) = abs(R(n,1)-R(n-1,1));
end
% Dividing each cycle count into two vectors,
% depending on the corrosponding slope of SN curve.
% For whole-cycles:
RFCUR(1,4) = 0; RFCUR(1,5) = 0;
for n=1:numel(RFCUR(:,3));
    if RFCUR(n,3) >= st;
        RFCUR(n,4)= RFCUR(n,3);
    else
        RFCUR(n,5)=RFCUR(n,3);
    end
end
% For half-cycles:
R(1,4) = 0; R(1,5) = 0;
for n=1:numel(R(:,3));
    if R(n,3) >= st;
        R(n,4)= R(n,3);
    else
        R(n,5)=R(n,3);
    end
end

% Determine unique stress-ranges, and also counts the
% number of instances of those stress-ranges.
% For whole cycles:
[URuniques1,URnumUnique1] = count_unique(RFCUR(:,4));
[URuniques2,URnumUnique2] = count_unique(RFCUR(:,5));
URuniques1(1) = []; URnumUnique1(1) = [];
URuniques2(1) = []; URnumUnique2(1) = [];
```

```
% For half cycles:
[Runiques1,RnumUnique1] = count_unique(R(:,4));
[Runiques2,RnumUnique2] = count_unique(R(:,5));
Runiques1(1) = []; RnumUnique1(1) = [];
Runiques2(1) = []; RnumUnique2(1) = [];

% Dividing the unique count by two for the half cycles
% so the unique count will represent the number of cycles:
RnumUnique1 = RnumUnique1./2; RnumUnique2 = RnumUnique2./2;

% Applying Miner summation for the cycles, ref DNV-RP-C203:
% Damage for whole cycles, for each SN slope:
URdamagem1 = (1/loga1).*sum(URnumUnique1.*(URuniques1).^m1);
URdamagem2 = (1/loga2).*sum(URnumUnique2.*(URuniques2).^m2);
% Damage for half cycles, for each SN slope:
Rdamagem1 = (1/loga1).*sum(RnumUnique1.*(Runiques1).^m1);
Rdamagem2 = (1/loga2).*sum(RnumUnique2.*(Runiques2).^m2);
% Summation of damage:
damage(:,p) = URdamagem1 + URdamagem2+ Rdamagem1 + Rdamagem2;

% Arranging damage matrix so that its shape has
% the same structure as applied scatter diagram
if numel(damage) ~ 19;
    damage(numel(damage)+1:19) = 0;
end

%% Histogram plot for all Hs and selected Tp
% Here exemplified by Tp = 13 (j+p == 13)
if (j+p) == 13
    Runiques = [Runiques1;Runiques2];
    Rnumunique = [RnumUnique1; RnumUnique2];
    URuniques = [URuniques2; URuniques1];
    URnumunique = [URnumUnique2; URnumUnique1];
    h2 = figure;
    bar(URuniques,URnumunique,'b','edgecolor','b');
    xlim([0,220])
    ylim([0,25])
    title(['Non-weighted histogram for Hs = ',num2str(j),...
        ', Tp = ',num2str(p+j),' - Cement level:15m'])
    ylabel('Number of cycles')
    xlabel('Stress range [MPa]')
    print(h2,'-depsc',['hist_hs_',num2str(j)])
```

```
            fprintf('For Hs =%2.0f, Tp = %2.0f\n',j,(j+p))
            fprintf('Total number of whole cycles is: %5.2f\n',...
                sum(URnumunique))
            fprintf('Total number of half cycles is: %5.2f\n',...
                sum(Rnumunique))
            fprintf('Total number of cycle bins is: %5.2f\n\n',...
                length(URnumunique))
        end


        %% Weighted calculations
        % loading weighted occurrence for hs/tp combination
        load scatterweight
        % Collecting all unique whole cycles into same vector
        b1 = [URuniques1;URuniques2];
        % Collecting all unique number count for whole cycles
        % into same vector and weighing by the probability
        % of occurence for current sea state
        a1 = [URnumUnique1;URnumUnique2]*scatterweight(j,p);
        % Adding to previous collected whole cycles
        % and whole cycle counts
        b2 = [b2; b1]; a2 = [a2; a1];
        clear b1 a1

        % Collecting all unique half cycles into same vector
        c1 = [Runiques1;Runiques2];
        % Collecting all unique number count for half cycles
        % into same vector and weighing by the probablity
        % of occurence for current sea state
        d1 = [RnumUnique1;RnumUnique2]*scatterweight(j,p);
        % Adding to previous collected half cycles
        % and half cycle counts
        c2 = [c2; c1]; d2 = [d2; d1];
        clear c1 d1
    end
    % Inserting damage for all Hs into one matrix:
    tpdamage(j,:) = damage;
end

%% Processing weighted whole cycles and half cycles
% Collecting all whole cycles and adding all weighted cycle count
% contribution from each sea state.
```

```
a2(1) = []; b2(1) = [];
unique_stressUR = unique(b2);
for i = 1:length(unique_stressUR)
    weightUR(i,1) = unique_stressUR(i);
    weightUR(i,2) = sum(a2(b2 == unique_stressUR(i)));
end
% Categorizing whole cycles depending if they are above
% or below SN curve knee point
for i = 1 : length(weightUR(:,1))
    if weightUR(i,1) >= st
        above_stUR(i) = weightUR(i,1);
        above_st_numUR(i) = weightUR(i,2);
    else
        below_stUR(i) = weightUR(i,1);
        below_st_numUR(i) = weightUR(i,2);
    end
end
% Collecting all half cycles and adding all weighted cycle count
% contribution from each sea state.
c2(1) = []; d2(1) = [];
unique_stressR = unique(c2);
for i = 1:length(unique_stressR)
    weightR(i,1) = unique_stressR(i);
    weightR(i,2) = sum(d2(c2 == unique_stressR(i)));
end
% Categorizing half cycles depending if they are above
% or below SN curve knee point
for i = 1 : length(weightR(:,1))
    if weightR(i,1) >= st
        above_stR(i) = weightR(i,1);
        above_st_numR(i) = weightR(i,2);
    else
        below_stR(i) = weightR(i,1);
        below_st_numR(i) = weightR(i,2);
    end
end

% Weighted Damage for whole cycles, for each SN slope:
WeightdamUR1 = (1/loga1).*sum(above_st_numUR.*(above_stUR).^m1);
WeightdamUR2 = (1/loga2).*sum(below_st_numUR.*(below_stUR).^m2);

% Weighted Damage for half cycles, for each SN slope:
```

```
WeightdamR1 = (1/loga1).*sum((above_st_numR).*(above_stR).^m1);
WeightdamR2 = (1/loga2).*sum((below_st_numR).*(below_stR).^m2);
% Weighted damage total
Weightdamtot = WeightdamUR1 + WeightdamUR2 + WeightdamR1 + WeightdamR2;

%% Re-arranging damage data to fit scatter diagram
tpdamage(3,2:19) = tpdamage(3, 1:18);
tpdamage(3,1) = 0;
tpdamage(4,3:19) = tpdamage(4,1:17);
tpdamage(4,1:2) = 0;
tpdamage(5,4:19) = tpdamage(5, 1:16);
tpdamage(5,1:3) = 0;
tpdamage(6, 5:19) = tpdamage(6, 1:15);
tpdamage(6, 1:4) = 0;
tpdamage(7, 6:18) = tpdamage(7, 1:13);
tpdamage(7, 1:5) = 0;
tpdamage(7, 19) = 0;
tpdamage(8,7:17) = tpdamage(8,1:11);
tpdamage(8,1:6) = 0;
tpdamage(8,18:19) = 0;

%% Weighted histogram for all Hs all Tp
h9= figure;
bar(weightUR(:,1),weightUR(:,2),'b','edgecolor','b');
xlim([0,220])
ylim([0,25])
ylabel('Number of cycles')
xlabel('Stress range [MPa]')
title(['Weighted histogram all Hs, all Tp - Cement level:15m'])
print(h9,'-depsc','weightedhist')
fprintf('Total number of weighted whole cycles for all Hs and all Tp is: %5.2f\n',...
    sum(weightUR(:,2)))
fprintf('Total number of weighted half cycles for all Hs and all Tp is: %5.2f\n',...
    sum(weightR(:,2)))
fprintf('Total number of weighted cycle bins is: %5.2f\n\n',...
    length(weightUR(:,1)))

%% Fatigue damage resulsts
load scatterdiag  % Importing scatter diagram

% Calculating probability for each sea state
scatter2= scatterdiag./(sum(sum(scatterdiag)));
```

```
% Multiplying damage for each sea state with probability
% of occurence for corresponding sea state
weighteddam = scatter2.*tpdamage;

disp('Weighted fatigue damage, D, for one hour operaion:')
% Sum of weighted damage, one hour
sumweight= sum(sum(weighteddam))

% The fatigue life in operation days IF the configuration
% of the drilling system remains unchanged
days=(1)/(sumweight*24);
disp('Fatigue life in days:')
disp(1/(sumweight*24))
```

Appendix E

Contents in attached data folder

Overview of folders and files in attached zip-file. Files concerning the 3D FEM model are not enclosed due to the sensitive nature of the information. Bold, italic text means it is a folder. Italic text means it is a file.

Excel

In the Excel folder the following files can be found.

Abaqus_tuning_calculations.xlsx
The iterative runs for calibrating the beam model in Abaqus.

Riflex_to_Abaqus_conversions.xlsx
Forces and moments from Riflex processed for application in Abaqus.

Fatigue_results.xslx
Fatigue damage and fatigue life from all studies.

Riserdata.xlsx
Calculation of required riser parameters and BOP parameters for input in Riflex.

Matlab

In the Matlab folder the following folders are included. The scripted file that should be run is named "*Fatigue_Assessment0m.m*". The other files can be disregarded. The data files *Hs1*.mat to *Hs8*.mat in each folder contains the imported moment-time series imported from Riflex for the study in question. By *Hs1* it is meant the sea state with significant wave height 1 m and all the corresponding spectral time periods. See the scatter diagram, Table 7.8.

MAINCASE_elastic

The fatigue assessment on the main study with the elastic BOP model and by application of the DNV example load-to-stress curve.

MAINCASE_infinite

The fatigue assessment on the main study with the infinitely stiff BOP model and by application of the DNV example load-to-stress curve.

PARAMETER_elastic_current

The fatigue assessment on the parameter study with the elastic BOP model where current is included in the analyses. Application of the DNV example load-to-stress curve.

PARAMETER_elastic_globaldamping

The fatigue assessment on the parameter study with the elastic BOP model where the global damping factor is altered from $\alpha = 0.02$ to $\alpha = 0.01$ in the analyses. Application of the DNV example load-to-stress curve.

PARAMETER_elastic_linearflexjointstiffness

The fatigue assessment on the parameter study with the elastic BOP model where the stiffness characteristics of the lower flex joint is changed from non-linear to linear in the analyses. Application of the DNV example load-to-stress curve.

PARAMETER_infinite_current

The fatigue assessment on the parameter study with the infinitely stiff BOP model where current is included in the analyses. Application of the DNV example load-to-stress curve.

PARAMETER_infinite_globaldamping

The fatigue assessment on the parameter study with the infinitely stiff BOP model where the global damping factor is altered from $\alpha = 0.02$ to $\alpha = 0.01$ in the analyses. Application of the DNV example load-to-stress curve.

PARAMETER_infinite_linearflexjointstiffness

The fatigue assessment on the parameter study with the infinitely stiff BOP model where the stiffness characteristics of the lower flex joint is changed from non-linear to linear in the analyses. Application of the DNV example load-to-stress curve.

SENSITIVITY_elastic_bendstiff1e8

Fatigue damage and fatigue life from all studies. The fatigue assessment on one of the sensitivity studies where the bending stiffness of LMRP connector and wellhead

connector is changed to 1×10^8 N m^2. DNV example load-to-stress curve is applied.

SENSITIVITY_elastic_bendstiff5e8
Fatigue damage and fatigue life from all studies. The fatigue assessment on one of the sensitivity studies where the bending stiffness of LMRP connector and wellhead connector is changed to 5×10^8 N m^2. DNV example load-to-stress curve is applied.

SENSITIVITY_elastic_bendstiff1e9
Fatigue damage and fatigue life from all studies. The fatigue assessment on one of the sensitivity studies where the bending stiffness of LMRP connector and wellhead connector is changed to 1×10^9 N m^2. DNV example load-to-stress curve is applied.

SENSITIVITY_elastic_bendstiff5e9
Fatigue damage and fatigue life from all studies. The fatigue assessment on one of the sensitivity studies where the bending stiffness of LMRP connector and wellhead connector is changed to 5×10^9 N m^2. DNV example load-to-stress curve is applied.

SENSITIVITY_elastic_bendstiff1e10
Fatigue damage and fatigue life from all studies. The fatigue assessment on one of the sensitivity studies where the bending stiffness of LMRP connector and wellhead connector is changed to 1×10^{10} N m^2. DNV example load-to-stress curve is applied.

SENSITIVITY_elastic_bendstiff5e10
Fatigue damage and fatigue life from all studies. The fatigue assessment on one of the sensitivity studies where the bending stiffness of LMRP connector and wellhead connector is changed to 5×10^{10} N m^2. DNV example load-to-stress curve is applied.

Comments
Upon request, the load-to-stress curves that were employed in this thesis have been removed. Instead, they have been replaced by the example load-to-stress curve found in the JIP [3]. This means that when running the fatigue assessment scripts, the results will not be the same as presented in this thesis, and thus not representative for the analyses that have been conducted. The fatigue assessment script is otherwise the same.

Riflex

In the Riflex folder the following folders are included.

Workspace and model files

bop_elastic_dynmod.inp
bop_elastic_elastic_inpmod.inp
bop_elastic_stamod.inp
Files regarding the global model with the elastic BOP model. Can be imported into Riflex through the interface in Riflex(File -> Import -> ... etc).

bop_infinite_dynmod.inp
bop_infinite_elastic_inpmod.inp
bop_infinite_stamod.inp
Files regarding the global model with the infinitely stiff BOP model. Can be imported into Riflex through the interface in Riflex(File -> Import -> ... etc).

RAO.TRA
Text document with the RAO inputs used in the global models in Riflex.

RIFLEX.sima
The workspace file used when working on this thesis in Riflex.

BOP_detailed
Contains the produced results from global analysis for the elastic BOP model. Results are found for the main study and two sensitivity studies. In each respective folder the moment-time series at wellhead datum is found. These files must be processed before they can be implemented in the Matlab fatigue assessment scripts. The files are equivalent of the *Hs1*.mat to *Hs8*.mat files in the Matlab folders. However, they can be opened by other software than Matlab.

Comments
Due to limitations in the allowed file size of the attachment, most of the result files from Riflex had to be omitted. In the event of interest in the data files for the studies that are not included in the attachment, contact the authors of the thesis.

Andreas Haukanes: andreashaukanes@gmail.com, or
Erling Harildstad: harildstad@gmail.com.